

Aus der Klinik für Strahlentherapie und Radioonkologie
Geschäftsführender Direktor: Herr Prof. Dr. Sebastian Adeberg
des Fachbereichs Medizin der Philipps-Universität Marburg

Titel der Dissertation:

**Investigating radiation effects of proton irradiation using Monte
Carlo simulations on micro- and nanometer scales**

Inaugural-Dissertation zur Erlangung des Doktorgrades der Medizinwissenschaften
(Dr. rer. med.)
dem Fachbereich Medizin der Philipps-Universität Marburg
vorgelegt von

Larissa Derksen

05.09.1995

aus Hagen

Marburg, 2024

Angenommen vom Fachbereich Medizin der Philipps-Universität Marburg am:
24.04.2024

Gedruckt mit Genehmigung des Fachbereichs Medizin

Dekanin: Frau Prof. Dr. D. Hilfiker-Kleiner

Referenten: Frau Prof. Dr. R. Engenhardt-Cabillic/ Herr Prof. Dr. K. Zink

1. Korreferentin: Frau Prof. Dr. K. Volz

In Peer-Review Journalen veröffentlichte Arbeiten

Diese kumulative Dissertation stellt eine Zusammenfassung von Forschungsergebnissen dar, die in Peer-Review-Fachzeitschriften veröffentlicht wurden. Die folgenden Manuskripte wurden veröffentlicht oder zur Veröffentlichung angenommen:

[1] **L. Derksen**, T. Pfuhl, R. Engenhardt-Cabillic, K. Zink and K.-S. Baumann. Investigating the feasibility of TOPAS-nBio for Monte Carlo track structure simulations by adapting GEANT4-DNA examples application. *Physics in Medicine & Biology*, 66(17), 175023, 2021.

[2] **L. Derksen**, V. Flatten, R. Engenhardt-Cabillic, K. Zink and K.-S. Baumann. A method to implement inter-track interactions in Monte Carlo simulations with TOPAS-nBio and their influence on simulated radical yields following water radiolysis. *Physics in Medicine & Biology*, 68(3), 135017, 2023.

[3] **L. Derksen**, S. Adeberg, K. Zink and K.-S. Baumann. Comparison of two methods simulating inter-track interactions using the radiobiological Monte Carlo toolkit TOPAS-nBio. Accepted by *Physics in Medicine & Biology*, 2024.

Die Publikationen werden im Text entsprechend der oben definierten Reihenfolge mit den Nummern 1-3 referenziert. Für die abgedruckten Publikationen gibt es, so erforderlich, eine Abdruckgenehmigung von IOP Publishing im Auftrag des „Instituts for Physics and Engineering in Medicine“ (IPEM).

Konferenzbeiträge

Im Rahmen der Dissertation wurden die Ergebnisse auf verschiedenen Konferenzen vorgestellt, die im Folgenden aufgeführt sind:

- PTCOG59, 4.–7. Juni 2021, online, Posterpräsentation mit dem Titel *Investigating the feasibility of TOPAS-nBio for Monte Carlo track structure simulations of GEANT4-DNA example applications*
- DGMP2021, 19.–21. September 2021, online, Posterpräsentation mit dem Titel *Investigating the feasibility of TOPAS-nBio for Monte Carlo track structure simulations of GEANT4-DNA example applications*
- DGMP2022, 21.–24. September 2022, Aachen, Deutschland, Vortrag mit dem Titel *Einfluss von inter-track Wechselwirkungen in radiobiologischen Monte-Carlo-Simulationen mit TOPAS-nBio zur Untersuchung des FLASH-Effekts*
- Fourth International Geant4 User Conference, 24.–26. Oktober 2022, Neapel, Italien, Vortrag mit dem Titel *A Monte Carlo based investigation of the FLASH effect by examining inter-track interactions in radiobiological simulations performed with TOPAS-nBio*
- FRPT2022, 30. November – 2. Dezember 2022, Barcelona, Spanien, e-Poster mit dem Titel *A Monte Carlo based investigation of the FLASH effect by examining inter-track interactions in radiobiological simulations performed with TOPAS-nBio*
- ESTRO2023, 12.–16. Mai 2023, Wien, Österreich, e-Poster mit dem Titel *A Monte Carlo based investigation of the FLASH effect by examining inter-track interactions in radiobiological Monte Carlo simulations*
- DGMP2023, 27.–30. September 2023, Magdeburg, Deutschland, Posterpräsentation mit dem Titel *Vergleich von zwei verschiedenen Methoden zur Simulation von inter-track Wechselwirkungen in dem radiobiologischen Monte-Carlo Toolkit TOPAS-nBio*
- FRPT2023, 5.–7. Dezember 2023, Toronto, Kanada, Posterpräsentation mit dem Titel *Dosimetric analysis of a synchrotron-based proton and carbon ion beamline for FLASH experiments*

Abstract

Proton therapy offers a distinct advantage in the scope of radiotherapy, allowing highly precise and conformal irradiation of tumor tissue while minimizing the impact on surrounding healthy tissue, compared to conventional radiotherapy with photons. This precision and protection is achieved by depositing the proton's energy within a narrow region known as the Bragg peak, leading to a more precise dose delivery and sharp dose falloffs. However, a challenge arising from the sharp dose gradients in the Bragg peak is the accurate determination of the range of the protons, including the localization of the Bragg peak. Thus, precise positioning of the Bragg peak is substantial; any over- or underestimation may lead to suboptimal tumor coverage, potentially resulting in underdosing, while the surrounding normal tissue and organ at risk (OAR) might receive an excessive radiation dose. In particular, the range of biological effects of protons appears to be underestimated with associated uncertainties of about 1 - 2 mm. While current radiation planning in proton therapy is conducted with a fixed relative biological effectiveness (RBE) value of 1.1 in comparison to photons, increasing research suggests that an adjustment and modulation of the RBE could be beneficial. Especially at the distal end of the Bragg peak, the RBE may be underestimated. The underestimation of the range related to biological effects carries the risk of increased radiation-induced toxicity in the surrounding OAR. This underscores the importance of ongoing efforts to optimize and model the RBE of protons in the field of radiotherapy. For examining the RBE, Monte Carlo simulations are particularly valuable, as the RBE depends on various factors that may be challenging to achieve with sufficient precision in experimental settings. However, Monte Carlo simulations enable an independent analysis of individual parameters and offer a cost and time efficient alternative to experimental approaches. One toolkit for performing Monte Carlo simulations with regard to the examination of the RBE is TOPAS-nBio. This powerful tool enables the simulation of each individual particle process, ranging from inelastic to elastic scattering, and extending to residual kinetic energies of secondary electrons as low as a few eV. This capability facilitates simulations on nano- and micrometer scales. Simulating on those scales is essential for RBE studies since the main biological effects are induced within the deoxyribonucleic acid (DNA), which consists of a double helix with a diameter of approximately 2 nm. In addition to physical interactions, TOPAS-nBio offers the capability to simulate chemical reactions of molecules created through radiolysis. So far, Monte Carlo simulations have primarily been conducted at macroscopic levels, wherefore the experience in utilizing programs that enable simulations at smaller scales is limited. To ensure the robustness and reli-

ability of the Monte Carlo code and to enable reliable interpretation of the results, it is essential to properly set up and validate the simulations.

Within the scope of this dissertation, a comprehensive exploration of proton radiation interactions was conducted by performing Monte Carlo simulations on nano- and micrometer scales using TOPAS-nBio, spanning from the physical to the chemical stage of the radiation. These studies are an indispensable prerequisite for subsequent research validating the code against experimental data and hence, for further investigating the biological effectiveness of proton radiation including both experiments and Monte Carlo simulations.

At first, the modelling of the physical stage following the irradiation was examined by investigating different default physics modules that are available in TOPAS-nBio. The findings indicate that the choice of the applied physics list can significantly affect simulation results, a consideration that should be taken into account when dealing with induced yields of chemical species and DNA damages resulting from inelastic processes. After the investigation of the physical stage, the dynamics and reactions of the molecules generated by radiolysis through the inelastic interactions, were analyzed. In the chemical stage, the focus was primarily on investigating the effects of so-called inter-track interactions, chemical reactions that may contribute to the FLASH effect. The study of the FLASH effect is particularly clinically relevant, as FLASH radiotherapy could expand the therapeutic window by reducing the radiation effect to healthy tissue. Since simulating inter-track interactions was not a default feature in TOPAS-nBio, a method was developed to enable and investigate these chemical reactions. It was demonstrated that inter-track interactions have a substantial impact on the chemical stage, observed for various radiation sources. As the number of inter-track interactions increased, potentially associated with FLASH radiotherapy, the overall yield of molecules, quantified by the G-value, decreased. In the meantime, a new version of TOPAS-nBio has been published, including a tool to simulate inter-track interactions employing a method different to the one developed in this study. In order to compare both methods, G-values of various molecules were simulated. For certain molecule types, the deviations reached up to 3.9% which is in an acceptable range regarding general deviations of experimental and simulated data of radiolytic species. These results demonstrate that both methods are suitable for examining the effects of inter-track interactions on the chemical stage.

In this dissertation, nanodosimetric simulations were performed that provide fundamental insights into the physical and chemical effects of radiation on small scales. In this context, a novel concept for the simulation of inter-track interactions was presented, providing a valuable contribution to the investigation and declaration of the FLASH effect in radiation therapy.

Zusammenfassung

Die Protonentherapie bietet im Rahmen der Strahlentherapie den Vorteil einer präzisen, konformalen Bestrahlung von Tumorgewebe, während das umliegende Normalgewebe im Vergleich zur Verwendung von Photonen weniger stark belastet wird. Die Präzision und Schonung wird dadurch erreicht, dass nahezu die gesamte Energie eines Protons im Bragg Peak punktuell abgegeben wird, was zu scharfen Dosisgrenzen führt. Eine Herausforderung, die sich aus den scharfen Dosisgradienten im Bragg Peak ergibt, ist die genaue Bestimmung der Reichweite der Protonen und Lokalisation des Bragg Peaks, d.h. die Position des Bragg Peaks muss präzise ermittelt und festgelegt werden. Eine Über- oder Unterschätzung kann dazu führen, dass der Tumor unterdosiert wird, wohingegen das Normalgewebe und umliegende Risikoorgane zu viel Dosis erhalten. Insbesondere die Reichweite von biologischen Effekten von Protonen scheint in Hinblick auf die Reichweite unterschätzt, wobei Unsicherheiten von 1-2 mm angenommen werden. Während die klinische Bestrahlungsplanung in der Protonentherapie derzeit mit einer relativen biologischen Wirksamkeit (RBE) im Vergleich zu Photonen von 1.1 erfolgt, wurde in einige Studien gezeigt, dass eine Anpassung und Modulation der RBE sinnvoll sein kann. Besonders am distalen Ende des Bragg Peaks scheint die RBE unterschätzt. Letzteres birgt das Risiko einer erhöhten strahleninduzierten Toxizität in den umliegenden Risikoorganen. Dies betont die Bedeutung der Optimierung und Modellierung der RBE von Protonen in der Strahlentherapie.

Um die RBE zu erforschen, erweisen sich Monte-Carlo-Simulationen als besonders wertvoll, da die RBE von verschiedenen Faktoren abhängt, die experimentell nicht immer mit ausreichender Genauigkeit eingestellt werden können. Monte-Carlo-Simulationen ermöglichen eine unabhängige Regulierung und Analyse einzelner Parameter und bieten darüber hinaus eine kostengünstige und zeiteffiziente Alternative zu experimentellen Ansätzen. Ein Toolkit für die Durchführung von Monte-Carlo-Simulationen im Zusammenhang mit der Untersuchung der RBE ist TOPAS-nBio. Mit diesem Simulationsprogramm kann jeder einzelne Prozess, von inelastischen über elastische Streuungen bis zu restlichen kinetischen Energien von Sekundärelektronen von einigen eV, simuliert werden, welches Simulationen auf Nanometerskalen ermöglicht. Die Simulation auf diesen Skalen ist für die Erforschung der RBE unerlässlich, da der Großteil an biologische Wirkungen innerhalb der DNA induziert wird, die aus einer Doppelhelix mit einem Durchmesser von etwa 2 nm besteht. Neben physikalischen Wechselwirkungen ist es zu dem in TOPAS-nBio möglich, die chemischen Reaktionen der durch die Radiolyse entstandenen Moleküle zu simulieren. Bisher wurden Monte-Carlo-Simulationen typischerweise auf makroskopischer Ebene durchge-

führt, weshalb die Erfahrung im Umgang mit Programmen, die Simulationen auf kleineren Skalen ermöglichen, eher gering ist. Um die Robustheit und Zuverlässigkeit des Monte-Carlo-Codes sicherzustellen und eine verlässliche Interpretation der Ergebnisse zu ermöglichen, ist es entscheidend, Simulationsparameter bewusst einzustellen und diese zu validieren.

Im Rahmen dieser Dissertation wurden die Wechselwirkungen von Protonenstrahlung von der physikalischen bis zur chemischen Phase auf Nano- und Mikrometerskalen mittels Monte-Carlo-Simulationen untersucht. Diese Untersuchungen legen den Grundstein für die Validierung des Codes und damit für weiterführende Erforschungen zur relativen biologischen Wirksamkeit der Protonenstrahlung mit Hilfe von Experimenten und Simulationen.

Zunächst wurde die Modellierung der physikalischen Phase der Strahlungswirkung untersucht, indem verschiedene Standard-Physikmodule, die im Monte-Carlo-Code verfügbar sind, analysiert wurden. Die Ergebnisse zeigen, dass die Wahl der Physikliste die Simulationsergebnisse erheblich beeinflussen kann. Die physikalischen, inelastischen Prozesse wirken sich wiederum auf die Entstehung chemischer Moleküle und die Verteilung von DNA-Schäden aus, was bei weiteren Simulationen entsprechend berücksichtigt werden sollte.

Nach der Untersuchung der physikalischen Phase erfolgte im Anschluss eine Analyse der Dynamik und Reaktionen von den Molekülen, die basierend auf den inelastischen Prozessen durch die Radiolyse erzeugt werden. In der chemischen Phase lag der Fokus darauf, die Effekte von sogenannten inter-track Wechselwirkungen, chemische Reaktionen, die zum FLASH-Effekt beitragen können, zu untersuchen. Die Erforschung des FLASH-Effektes ist klinisch besonders relevant, da durch die FLASH-Strahlentherapie das therapeutische Fenster erweitert werden könnte, indem die Strahlungswirkung auf das Normalgewebe verringert wird.

Da die Simulation von inter-track Wechselwirkungen in TOPAS-nBio standardmäßig nicht möglich war, wurde eine Methode entwickelt, um diese chemischen Reaktionen zu untersuchen. Es wurde für verschiedene Strahlenquellen gezeigt, dass durch inter-track Wechselwirkungen die chemische Phase signifikant beeinflusst wird. Mit der Zunahme von inter-track Wechselwirkungen, welches möglicherweise mit der FLASH-Strahlentherapie zusammenhängt, wurde die gesamte Ausbeute von Molekülen, ausgedrückt durch den sogenannten G-Wert, verringert.

In der Zwischenzeit wurde eine neue Version von TOPAS-nBio veröffentlicht, die ein Tool zur Simulation von inter-track Wechselwirkungen enthält, das eine andere Methode als die in dieser Studie entwickelte verwendet. Um beide Methoden zu vergleichen, wurde der G-Wert für verschiedene Moleküle simuliert. Für einzelne Molekülarten können die Abweichungen bis zu 3,9% betragen, welches im Rahmen der Abweichungen von Ergebnissen von Simulationen und

Experimenten liegt. Diese Ergebnisse zeigen, dass beide Methoden geeignet sind, um Einflüsse von inter-track Wechselwirkungen zu erforschen.

In dieser Dissertation wurden nanodosimetrische Simulationen durchgeführt, die grundlegende Einblicke in die physikalischen und chemischen Effekte von Strahlung auf kleinen Skalen liefern. In diesem Zusammenhang wurde ein neues Konzept zur Simulation von inter-track Wechselwirkungen vorgestellt, das einen wertvollen Beitrag zur Untersuchung und Erklärung des FLASH-Effekts in der Strahlentherapie leisten kann.

Contents

Abstract	vi
Zusammenfassung	viii
List of Figures	xiii
List of Tables	xiv
List of Abbreviations	xv
1 Introduction	1
1.1 Cancer and therapeutic approaches	1
1.2 Proton therapy: principles, benefits and challenges using heavy charged particles in radiooncology	2
1.3 Radiation effects on physical, chemical and biological scales	7
1.4 FLASH radiotherapy	10
1.5 Monte Carlo simulations and the toolkit TOPAS	12
2 Aim of this dissertation	14
3 Summary of the results and contributions	15
3.1 Article 1: Investigating the feasibility of TOPAS nBio for Monte Carlo track structure simulations by adapting GEANT4-DNA examples application	15
3.1.1 Summary of article 1	15
3.1.2 Contributions	21
3.2 Article 2: A method to implement inter-track interactions in Monte Carlo simula- tions with TOPAS-nBio and their influence on simulated radical yields following water radiolysis	21
3.2.1 Summary of article 2	21
3.2.2 Contributions	29

3.3	Article 3: Comparison of two methods simulating inter-track interactions using the radiobiological Monte Carlo toolkit TOPAS-nBio	29
3.3.1	Summary of article 3	29
3.3.2	Contributions	35
4	Discussion	36
4.1	Simulation of the physical stage	36
4.2	Simulation of the chemical stage	37
4.3	The potential role of radiochemistry in the FLASH effect	40
4.4	Applicability and limitations of the Monte Carlo toolkit TOPAS-nBio for nanodosimetric simulations	42
5	Conclusions and outlook	43
	Bibliography	46
	Published articles	61
	Appendix	121
	Verzeichnis der akademischen Lehrenden	121
	Danksagung	122
	Ehrenwörtliche Erklärung	123

List of Figures

1.1	Relative depth dose curves of photon and proton beams in water	3
1.2	Effects of radiation on the physical, pre-chemical, chemical and biological stage .	8
3.1	Comparison of the process counts of electron, proton and hydrogen processes summarized from 100 primary protons of 100 keV energy using three different physics list options	17
3.2	Frequency and energy depositions of all electron processes with initial energies in the range of 10 - 60 eV using G4EmDNAPhysics_option2	19
3.3	Illustration of the number of steps per process and range for 100 individual events of an energy of 24.2 eV	20
3.4	G-value in dependence of the number of tracks with inter-track interactions for 60 eV electrons	23
3.5	Investigation of chemical reactions during the overall chemical stage in depen- dence of the number of tracks with inter-track interactions	25
3.6	Time-dependent G-values of $\bullet\text{OH}$ and H_2O_2	26
3.7	G-value in dependence of the number of tracks with inter-track interactions for 10 MeV and 100 MeV protons	28
3.8	Comparison of the G-value G_{all} and the G-values of $\bullet\text{OH}$, $\text{H}_2\text{O}^\bullet$ and H_3O using the phsp and TsIRTInterTrack method enabling inter-track interactions	31
3.9	Comparison of the G-values of OH^- , H_2 , H_2O_2 and e_{aq} using the phsp and TsIRTInterTrack method enabling inter-track interactions	32
3.10	Comparison of time-dependent G-values of $\bullet\text{OH}$ for $N=2$ using the phsp and TsIRTInterTrack method	33
3.11	Number of inelastic processes and chemical species processing	34
5.1	Total number of indirect DNA strand breaks using a 10 MeV proton beam	45

List of Tables

3.1	Electron processes included in GEANT4-DNA	18
3.2	Chemical reactions and reaction rates considered in the chemical stage	24
4.1	Deposited energies in eV by vibrational excitation, electronic excitation and ion- ization using the physics list G4EmDNAPhysics_option2	38

List of Abbreviations

CH	Condensed history
CSD	Continuous slowing down
CT	Computer tomography
DSB	Double-strand break
DNA	Deoxyribonucleic acid
HU	Hounsfield unit
ICRU	International Commission on Radiation Units and measurements
IMPT	Intensity Modulated Proton Therapy
IMRT	Intensity Modulated Radiotherapy
IRT	Independent reaction time
LET	Linear energy transfer
OAR	Organ at risk
QUANTEC	Quantitative Analyses of Normal Tissue Effects in the Clinic
RBE	Relative biological effectiveness
SBRT	Stereotactical Body Radiotherapy
SBS	Step-by-step
SSB	Single-strand break
TOPAS	TOol for PArticle Simulations
TS	Track structure
VMAT	Volumetric Modulated Arc Therapy

CHAPTER 1

Introduction

1.1 Cancer and therapeutic approaches

In conjunction with cardiovascular diseases, cancer diseases, particularly trachea, bronchus, and lung cancers, are one of the world's leading causes of death, presenting a major burden on society (WHO, 2020). In 2020, more than 19 million new cancer cases including 400,000 children were recorded, whereas about 10 million deaths were attributed to cancer (Sung et al., 2021). Actually, the incidence is assumed to increase to approximately 28.4 million cases in 2040 caused by factors such as the demographic change and increasing risk factors, e.g. smoking, excess body weight and physical inactivity (Sung et al., 2021).

The statistics provided underline the importance of an efficient cancer treatment. Currently, the spectrum of cancer treatment modalities is very wide, so that the decision for a particular therapy depends on the type of cancer, the individual diagnosis and the defined treatment goal. The treatment goal can be classified into two groups: the curative and the palliative treatment. The aim of the curative treatment is to completely remove a tumor or reduce its size and prevent further growing. In cases in which the disease is too advanced, and a curative treatment cannot achieve successful results, a palliative treatment is applied, reducing symptoms and improving the patient's quality of life. Cancer treatment includes therapeutic methods like chemotherapy, hormone therapy, immunotherapy, stem cell transplant, surgery and radiotherapy. Patients commonly receive a combination of two or more different treatment modalities, albeit nearly one in two cancer patients receives radiotherapy as part of their treatment progress (Borras et al., 2015). Radiotherapy provides the advantage that many different tumor types, sizes and shapes can be addressed. In this case, high radiation doses are applied to kill cancer cells and thus shrink the tumor. This is achieved as the radiation causes cell damage through interactions of the ionizing radiation with the surrounding molecules. Damages include double-strand breaks in the DNA leading to a dysfunction of the cells and eventual cell death. In this case, the yield of DNA

damages and cell death is related to the deposited energy in the cells: An increased dose leads to a larger number of unrepaired DNA damages and hence to a decreased cell survival. However, the interactions of the radiation are not only limited to the tumor tissue alone, but they also affect the surrounding normal tissue. Nevertheless, healthy tissue has the advantage that it can regenerate and repair certain damages up to defined dose levels, whereas the mechanism is less elaborated in cancerous cells (Withers, 1975). In this context, the concept of the therapeutic window was established, which describes a range of doses that compromise between achieving the greatest tumor control and minimizing the likelihood of side effects of healthy tissue. Thus, for the success of a radiotherapy treatment, a precise application of a well-planned dose distribution is essential. This includes accurate imaging, careful planning and an exact dose application of the radiation therapy device. Constant research and development is ongoing with the aim of making radiotherapy as precious as possible (Chandra et al., 2021). For this reason, techniques such as Intensity Modulated Radiotherapy (IMRT) (Group et al., 2001), Volumetric Modulated Arc Therapy (VMAT) (Otto, 2008), Cyberknife (Adler Jr et al., 1997), Stereotactical Body Radiotherapy (SBRT) (Potters et al., 2004), have been developed and are now implemented in clinical practice. While most people receive radiation therapy involving photons, there is also the possibility of irradiating the tumor with heavy charged particles such as protons and carbon ions. This has advantages regarding normal tissue protection compared to irradiation with photons. In the next section, the use and benefits of protons in radiotherapy are further described.

1.2 Proton therapy: principles, benefits and challenges using heavy charged particles in radiooncology

In proton therapy, the special physical characteristics of these ions regarding their energy loss per unit distance are utilized to precisely irradiate tumors while minimizing radiation exposure to surrounding healthy tissues and OAR. In contrast to photons, which deposit energy in the medium through the generation of secondary electrons, protons are directly ionizing. Small contributions of energy are continuously transferred through numerous small collisions in form of coulomb scattering with the shell electrons, known as the continuous slowing down (CSD) concept of charged particles. However, with increasing depth of the protons in the medium, the rate of energy loss, also defined as the linear energy transfer (LET), increases. Just before reaching the end of their range, protons exhibit such a high LET that nearly all their energy is deposited locally. This characteristic behavior is reflected in the depth dose profile by the so-called Bragg

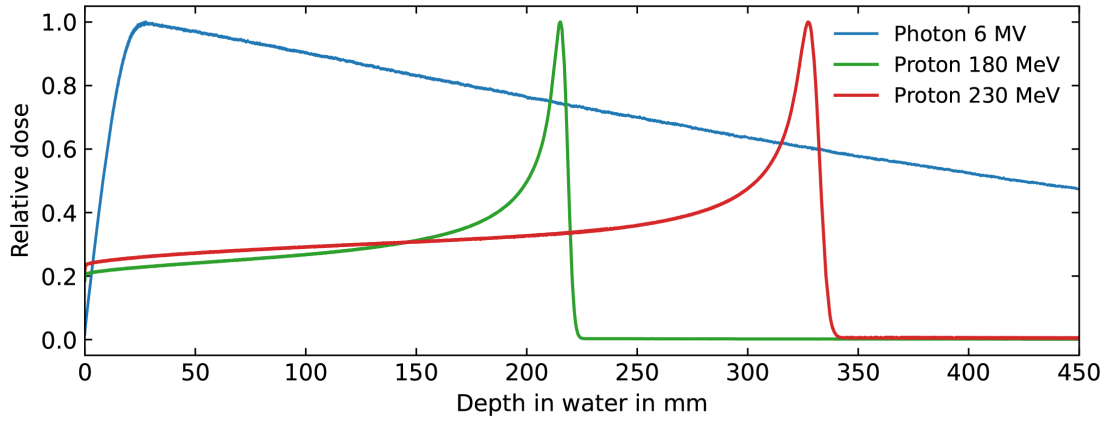


Figure 1.1: Relative depth-dose curves of photon (blue) and proton beams (green, red) in water.

peak as shown in figure 1.1. After reaching the dose maximum, the curve drops abruptly, effectively limiting the range of the protons. The energy loss of high energy charged particles through matter is described by the stopping power, which includes electronic and nuclear components. The nuclear stopping power involves interactions with the nucleus, while the electronic stopping power covers coulomb interactions, preliminary with the shell electrons. Regarding clinical proton energies, the electronic stopping power predominates. Thus, mathematically, the energy loss can be expressed by the Bethe-Bloch formula of the electronic stopping power, dE/dx , initially proposed by Bethe (1930) and further adjusted by Bloch (1933), as follows:

$$-\frac{dE}{dx} = \frac{4\pi n z^2}{m_e c^2 \beta^2} \left(\frac{e^2}{4\pi \epsilon_0} \right)^2 \left[\ln \left(\frac{2m_e c^2 \beta^2}{I(1-\beta^2)} \right) - \beta^2 \right] \quad (1.1)$$

The electronic stopping power depends, on the one hand, on general constants including the velocity of light in vacuum c , the electron charge e , rest mass m_e and the vacuum permittivity ϵ_0 and, on the other hand, on parameters of the radiation particle, namely its charge z and its velocity v expressed as $\beta = v/c$. Furthermore, the mean excitation potential I and the electron number density n of the material influence the energy loss per unit length. The latter can be expressed as:

$$n = \frac{N_A Z \rho}{A M_u} \quad (1.2)$$

with N_A as the Avogadro number, M_u the molar mass constant and material specifications including the atomic number Z , the relative atomic mass A and the density ρ .

The benefits of the characteristic depth dose profile regarding the use of protons in the treatment of tumors was already proposed by Wilson (1946) in 1946. He emphasized that the range of

protons, and thereby the depth of the Bragg peak, can be precisely adjusted by the proton energy. By adjusting the proton energy aligning their range to the tumor's position, the maximum dose is deposited in the cancerous tissue while sparing surrounding normal tissue, both at the surface and tissue immediately distal to the tumor. Reduced scattering radiation associated with protons in contrast to photons further contributes to minimizing dose exposure of healthy tissue.

Sparing of normal tissue through the beneficial use of protons has been observed in numerous studies comparing radiotherapy with photons and protons (McDonald et al., 2016; Romesser et al., 2016; Mock et al., 2004; Lin et al., 2015). For example, Holliday et al. (2015) showed in a comparative study applying Intensity Modulated Proton Therapy (IMPT) and IMRT treating nasopharyngeal cancer that the dose exposure of OAR e.g. oral cavity, brainstem, and the whole brain was significantly lower for patients receiving IMPT compared to IMRT. Furthermore, Schneider et al. (2000) identified a reduction of nearly 50% of cancer incidence after treating Hodgkin's disease with proton therapy in contrast to photon radiotherapy. Moreover, these advantages of proton therapy were shown to be particularly significant for pediatric radiotherapy (Fuss et al., 2000; Miralbell et al., 1997; Tatsuzaki et al., 1992; Kirsch and Tarbell, 2004; Munck af Rosenschold et al., 2016). For pediatric patients, the distance between the tumor and OAR is, in general, much smaller due to the smaller body size. Additionally, their radiosensitivity is higher since children are still in the stage of growth, as well as their integral tumor risk due to a longer life expectancy. All in all, the most important benefit of proton therapy is a reduced exposure of normal tissue, minimizing the patient's risk of side effects.

Even though the potential of proton therapy is substantial and promising, there are certain challenges that require effective improvement and solutions. In comparison to photon irradiation, the application is quite expensive and the availability of proton facilities with 114 operating institutions is currently significantly smaller than for photons, even though the construction of further facilities is planned (PTCOG, 2023). Moreover, the historical experience using protons clinically is not as extensive and long-lasting than with photons: While the irradiation with photons had its origin in the late 19th and early 20th centuries, first patients were irradiated with protons in 1954 (Leszczynski and Boyko, 1997; Tobias et al., 1958). Furthermore, while the depth dose profile of protons including the Bragg Peak offers distinctive advantages, it also raises challenges since the range of protons needs to be adjusted as precisely as possible to the volume of interest. Under- or overestimating the range, just by a few millimeters, results in less dose to the tumor, whereas the dose exposure is higher for the healthy tissue (Wedenberg and Toma-Dasu, 2014).

However, there are some uncertainties related to the range. As highlighted in equation 1.1, the

material of the medium is one of the factors influencing the loss of energy. Therefore, the resolution of the computer tomography (CT) scan, which serves as the basis for treatment planning, can contribute to inaccurate results of the calculation of proton ranges during the treatment planning process (España and Paganetti, 2011). Additionally, the conversion of CT based Hounsfield unit (HU) to relative stopping powers can lead to uncertainties up to 1 - 3 mm (Schaffner and Pedroni, 1998; Chvetsov and Paige, 2010). Furthermore, movement of any anatomical structures in the surrounding of the tumor, or a shift or motion of the tumor itself, impacts the proton range as well as the tumor coverage. Additional sources of uncertainty may arise from inaccuracies in the setup or approximations in dose calculations (Paganetti, Harald, 2012). The most crucial factor, however, is the uncertainty of the range of biological effects with uncertainties in the order of 1 - 2 mm (Paganetti, Harald, 2012; Grün et al., 2013). While this range uncertainty is within the same order of magnitude as the previously mentioned uncertainties, it demands a unique and careful consideration. The clinical consequences of the uncertainties in the range of biological effects are directly observable, as further discussed in the subsequent part of this section. Since range uncertainties are crucial factors in proton therapy, most proton facilities use a safety margin to cover those uncertainties. For example, several facilities report a safety margin of 3.5% of the range with additional 3 mm (Paganetti, Harald, 2012). However, enlarging the target volume with the safety margin, covering more healthy tissue, limits the efficiency of proton therapy. This highlights the need of further research regarding the current uncertainties in proton therapy. In particular, the relative biological effectiveness (RBE) of protons is the focus of research. The RBE is defined as the ratio of two doses of different radiation qualities resulting in the same biological effect within the same conditions:

$$\text{RBE} = \frac{D_{\text{ref}}}{D_x} \Big|_{\text{Isoeffect}} \quad (1.3)$$

with D_{ref} representing the dose of the reference radiation, which is commonly high-energy photon radiation or Cobalt-60, and D_x , the dose of the radiation quality of interest (ICRU, 2007). Currently, in the clinical practice a generic RBE of 1.1 is used for protons in relation to high-energy photons (ICRU, 2007). The value is derived from a combination of in vitro and in vivo experiments, a conclusion that was elaborated as reasonable by Paganetti et al. (2002) in their comprehensive analysis, reflecting the current state of research in 2002. However, nowadays, it is assumed that a fixed RBE value of 1.1 is not sufficient taking into account in the treatment planning (Wouters et al., 1996, 2015; Paganetti and Goitein, 2000; Paganetti, 2003; Ödén et al.,

2017). It has been revealed that the RBE is influenced by various factors including the type of radiation, fractionation, dose per fraction, LET, tissue or cell type and the biological endpoint considered in experimental studies (Paganetti, Harald, 2014; Wouters et al., 2015; Green et al., 2001; Belli et al., 2000). Especially, an increasing LET, promotes an increasing biological effect. Even though the dose at the distal edge of the Bragg Peak is low, but the LET is still high, the RBE is underestimated particularly in this region (Paganetti, Harald, 2014; Liu et al., 2022). As a result of certain clinical studies, it has been highlighted that this might be the reason for proton radiotherapy related toxicities in surrounding healthy tissues. As an example, Indelicato et al. (2014) investigated the tolerance to proton therapy of pediatric brainstem toxicities of 313 patients with tumors of the brain and skull base. In all cases, the brainstem dose was within QUANTEC (*Quantitative Analyses of Normal Tissue Effects in the Clinic*) (Emami et al., 1991; Bentzen et al., 2010) constraints. Nevertheless, for 11 out of 313 patients, a brainstem toxicity was observed as part of their radiotherapy treatment. The two-year cumulative incidence of toxicity was 3.8% and grade 3+ toxicity was 2.1% recommending a more conservative dosimetric guideline. Comparable findings have been reported in other research studies investigating proton therapy's side effects, indicating that the prior incorporation of a RBE of 1.1 is not adequate enough for treatment planning (Bahn et al., 2020; Nanda et al., 2017; Peeler et al., 2016; Giantsoudi et al., 2016). Therefore, models must be developed to encompass all relevant RBE dependencies of protons, which can then be integrated into the treatment planning process.

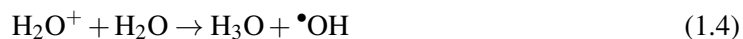
In the past, some phenomenological models, mostly based on the linear quadratic model (Fowler, 1989), but also mechanistic ones, have already been established to include variabilities of RBE (Belli et al., 1997; Wilkens and Oelfke, 2004; Tilly et al., 2005; Chen and Ahmad, 2011; Wedenberg et al., 2013; Jones, 2015; Mairani et al., 2017; Rørvik et al., 2018). These models address factors such as LET-dependency, dose per fraction and tissue parameters. Although numerous models have been developed to account for the impact of various factors on the RBE, they do not yet show the desired results. In fact, Rørvik et al. (2018) has compared eleven of these models, revealing considerable discrepancies up to 50% in the calculated RBE and RBE-weighted dose depending on the region of the planning target volume (PTV) and considered OAR across the various approaches. He claimed that this is due to different accounting for biological data and mathematical models. Nevertheless, McMahon (2021) was able to show that the consideration of the LET between those models leads to highly consistent results. In conclusion, to fully harness the benefits of proton therapy and minimize side effects associated with biological uncertainties, the biological effectiveness of protons at the cellular level requires further detailed investigations.

1.3 Radiation effects on physical, chemical and biological scales

As presented in the previous sections, the biological effectiveness of irradiation is the key factor responsible for the success of each radiotherapy. The effectiveness, in turn, is conditioned by a multitude of factors and primarily shaped by the prior physical and chemical interactions of radiation with the surrounding biomolecules. Thus, this section will give an overview of the interaction of radiation on the physical, pre-chemical, chemical and biological stages as it is illustrated in figure 1.2.

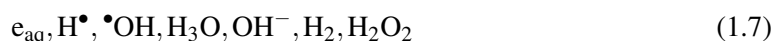
Beginning with the physical stage, which directly starts after the irradiation and lasts around 1 fs, the radiation interacts with the biological matter, primarily water, in form of elastic and inelastic processes. Inelastic processes include particularly ionization and electronic excitations, which deposit energy in the system. This results in excited (H_2O^*) and ionized (H_2O^+) water molecules leading to the next stage of interaction, the pre-chemical stage.

In the pre-chemical stage, also referred to as the physicochemical stage, those ionized and excited molecules produce highly reactive radicals (Allen, 1961; Buxton, 1987; Draganic, 2012). The pathways of these reactions are shown in the following equations for ionization as well as electronic excitations:



Regarding ionization, it creates a cation and a free electron. The cation further reacts with another water molecule resulting in H_3O and $\bullet\text{OH}$ radicals, whereas the free electron surrounds itself with a few (n) water molecules forming namely a solvated electron e_{aq} (eq. 1.6¹). Excited water molecules can for example dissociate and follow the same pathway as ionized molecules (eq. 1.4) or the excited water molecule splits into $\bullet\text{OH}$ and $\text{H}\bullet$ (eq. 1.5). Further processes are auto-ionization, dissociative relaxation and thermalization. It is assumed that these processes are finished within 1 ps after irradiation.

In the next stage, the chemical stage, these created radicals can further diffuse and react with other produced radicals or bio-molecules. Thus, in sum, irradiation creates mainly the following chemical species:



¹On the right-hand side of the equation, water molecules are not listed explicitly as they are part of e_{aq} .

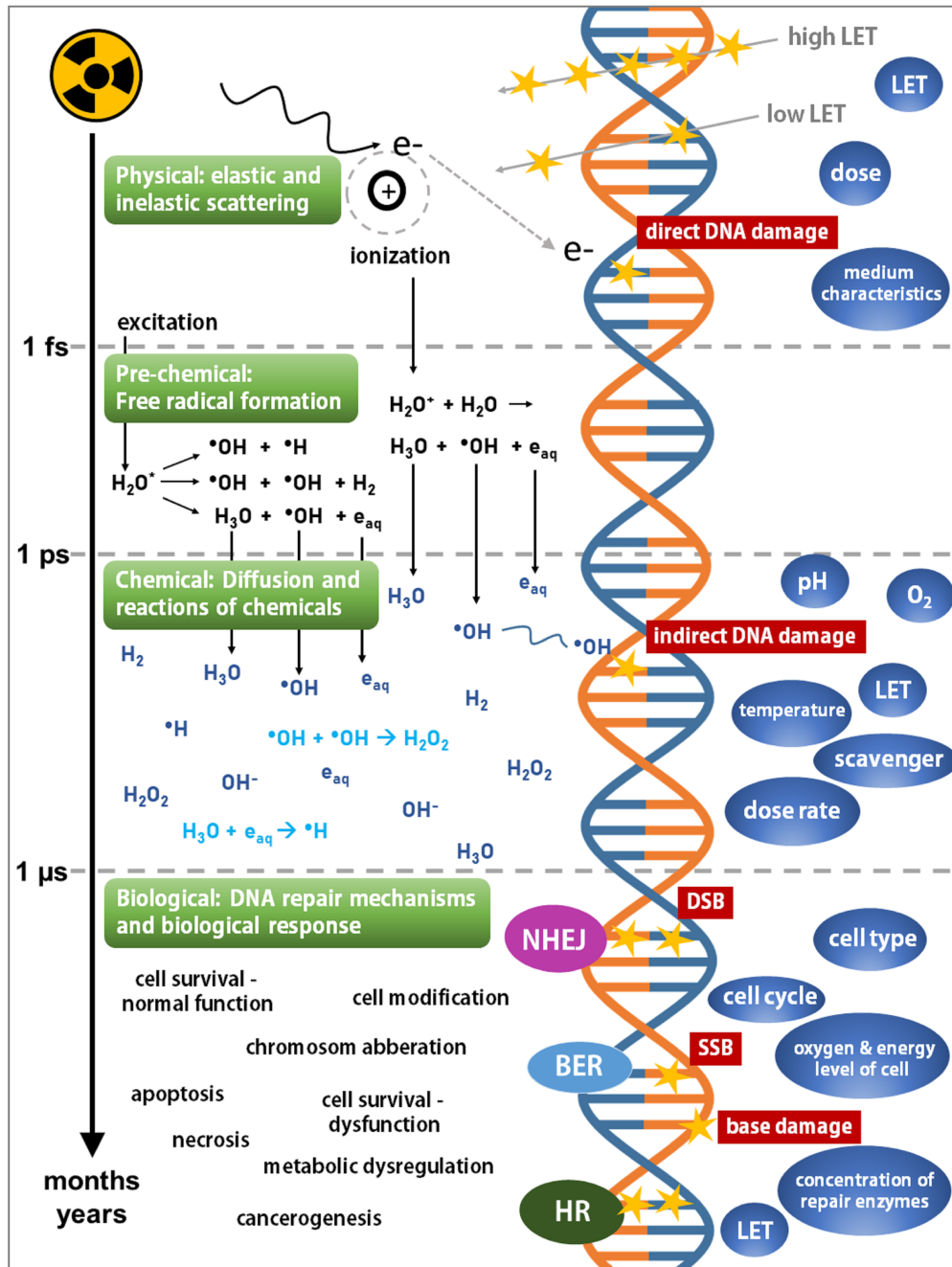


Figure 1.2: Schematic illustration of the effects of radiation on the physical, pre-chemical, chemical and biological stage (green boxes) in dependence of the time after irradiation including effects on the DNA (red boxes) and exemplary factors influencing the different stages (blue bubbles on the right).

Here, the number of molecules $M(t)$ created through radiolysis given at a time t normalized to 100 eV of deposited energy E defines the G-value $G(t)$:

$$G(t) = \frac{M(t) \cdot 100}{E(\text{eV})}. \quad (1.8)$$

Moreover, the G-value depends not just on the delivered dose, but also on the LET of the radiation (Burns and Sims, 1981). For radiation sources of higher LETs, the density of inelastic interactions is higher, resulting in a higher density of chemicals. Additionally, factors such as oxygen concentration in the biomolecular system, temperature, pH, presence of scavengers and components of the system can influence the chemical reactions and are crucial factors that must be taken into account when considering radiation effects on the chemical stage (Grimes and Partridge, 2015; Draganic and Draganic, 1971; Hiroki et al., 2002; Pastina and LaVerne, 1999; Štefanić and LaVerne, 2002; Plante, 2011; Autsavapromporn et al., 2007). Furthermore, it is important to consider that the dose rate of irradiation can have an impact on the kinetics and reactions of chemicals. Therefore, ultra-high dose rate irradiation, known as FLASH radiotherapy, holds particular significance in this context, which is further described in the next section. Assuming a homogeneous distribution of chemical species, the chemical stage is finished approximately at 1 μs .

Due to the physical and chemical interactions, the biological system has already sustained substantial modifications and structural alterations. This radiation-induced damage can be categorized into two primary classes: direct and indirect damages. Direct damage arises directly from the physical interactions between radiation particles and biological components, while indirect damages are obtained by the radiolysis products. The primary molecular target for such damage is the DNA molecule. DNA damages are mainly single-strand breaks (SSBs), double-strand breaks (DSBs), and base damage (Ward, 1988). For the development of SSBs and DSBs, there is an empirical rule suggesting that within an applied dose of 1 Gy approximately 1000 SSBs and 10 - 40 DSBs occur per cell (Ward, 1988; Lomax et al., 2013). However, the occurrence of SSBs and DSBs differs between sparsely (low LET) and densely (high LET) ionizing radiation. For higher LET, more clustered and complex damage is observed than for low LET irradiation (Zhu et al., 2020; Goodhead, 1994; Belli et al., 1994). All lesions are subsequently addressed and repaired during the following and final stage of irradiation, the biological stage.

At the beginning of this stage, the focus is particularly on repairing the DNA and affected components. These can take minutes to hours and depend on factors such as cell type, cell cycle,

oxygen and energy level of a cell, concentration of repair enzymes and the general condition of the tissue. There are several different repair mechanisms, differing regarding their repair target, the fastness of the repair as well as their rate of miss repair (Shrivastav et al., 2008; Sonoda et al., 2006; Lieber, 2008; Jackson, 2002). Just as the initial DNA damage depends on the LET, the rate of successful repair depends on the LET as observed in previous studies (Jenner et al., 1993) indicating reduced DSB rejoining with high-LET radiation. The consequences of irradiation at the biological level range from modifications of the genetic material and damage to cells and organelles, to metabolic disorders, cell division inhibition, increased cell division rate associated with the growth of tumors, and cell death. In the context of radiotherapy, the primary objective is the induction of apoptosis and senescence in cancerous cells through radiation.

1.4 FLASH radiotherapy

FLASH radiotherapy describes the application of very high doses in extremely short time periods, delivering ultra-high dose rates of over 40 Gy/s (Favaudon et al., 2014). In comparison, conventional dose rates are about 0.03 Gy/s. FLASH radiotherapy is considered to be a promising new technique in the field of radiotherapy, since in several experimental studies a reduced normal tissue toxicity could be observed applying ultra-high dose rates, whereas the tumor control remained constant (Favaudon et al., 2014; Montay-Gruel et al., 2019; Fouillade et al., 2020). For instance, in an experimental animal study by Montay-Gruel et al. (2019), mice brains were exposed to electron radiation at conventional dose rates (0.07 - 0.1 Gy/s) or FLASH dose rates (≥ 100 Gy/s). While conventional dose rates resulted in radiation-induced neurocognitive deficits, FLASH irradiation showed no significant loss in extinction memory, depression, or anxiety. This normal tissue sparing effect has the potential to spread the therapeutic window of radiotherapy, positively affecting the treatment efficiency. Thus, with this special therapy, even tumors that are considered as radioresistant could be treated efficiently by increasing the dose to the tumors. The potential effect of ultra-high dose rates in radiotherapy was first introduced by Hornsey and Alper (1966) in 1966. However, Favaudon et al. (2014)'s research and subsequent re-evaluation of the ultra-high dose rate effect, referred to as the FLASH effect, in 2014, evoked an expansion of investigations into this subject (Gao et al., 2022).

Although the results are very promising, the technique is not yet clinically implemented. This is partly due to the need for an appropriate adaption of techniques including devices delivering such ultra-high dose rates and dosimetric measurement equipment as well as quality assurance

protocols, but particularly, because the origin of the FLASH effect is not yet fully understood. Although there are now facilities capable of consistently delivering FLASH dose rates, and dosimetric measurement tools are available (Marinelli et al., 2022; Gómez et al., 2022; Baack et al., 2022) with ongoing research in this area, the lack of knowledge regarding the underlying mechanisms of the FLASH effect remains a challenge.

Components considered contributing to the FLASH effect are for example the reduction of oxygen and inter-track interactions on the chemical level of the radiation effect, but also the complexity and number of DNA damages and the subsequent immune response, suggested by several experimental and simulation studies (Jansen et al., 2021; Boscolo et al., 2021; Lai et al., 2021; Buonanno et al., 2019; Froidevaux et al., 2023; Labarbe et al., 2020; Abolfath et al., 2020). Meanwhile, some approaches including the complete depletion of oxygen (Jansen et al., 2021) could be classified as rather implausible to explain the FLASH effect as summarized by Limoli and Vozenin (2023). All in all, it is emphasized that one approach, either physical, chemical or biological, alone will not explain the FLASH effect, as it is rather “the result of a multi-parameter situation” (Rothwell et al., 2021).

Even though the basic mechanisms of the FLASH effect are not known yet, but since experimental results are highly promising, in 2019, a first skin cancer patient was already treated palliative with FLASH-RT at the University Hospital in Lausanne (Switzerland) showing promising results on normal tissue protection and tumor control (Bourhis et al. 2019). Furthermore, between 2020 and 2022, a first patient study, FAST-01 (NCT04592887), involving a cohort of 10 patients was conducted (Daugherty et al., 2023; Mascia et al., 2023). This clinical trial implemented the FLASH technique with protons in the form of a palliative radiotherapy treating extremity bone metastases. This trial showed that the application of FLASH radiotherapy is feasible and safe since the adverse effects were similar to conventional radiotherapy. Additionally, a follow-up study, FAST-02, is currently planned. Moreover, there is an ongoing patient study (NCT04986696) at the University Hospital in Lausanne examining dose escalation with electron FLASH radiation (ClinicalTrials.gov, 2023).

All experiments, simulations and clinical research reported so far show that even though the knowledge gap of radiotherapy using ultra-high dose rates is slowly closing, the FLASH effect itself needs to be further investigated.

1.5 Monte Carlo simulations and the toolkit TOPAS

Monte Carlo simulations have become an indispensable tool and a powerful technique in various fields of medical physics, including radiotherapy, medical imaging, and nuclear medicine (Rogers, 2006). Monte Carlo algorithms are a statistical approach developed to solve intractable or complex problems and integrals, firstly motivated and presented by Metropolis and Ulam (1949). Based on the probability theory and the law of large numbers, random experiments are frequently repeated with different random and independent samples. In this way, the mean value of the experiments converges towards the expected value. However, this method requires the input of appropriate physical quantities. For example, in order to simulate the interaction of radiation with matter, it requires data like scattering cross-sections, particle characteristics and material properties. These data are acquired through a combination of experimental data and theoretical models.

There are several tools available to simulate the radiation transport through matter, which includes the open-source Monte Carlo code GEANT4 (Agostinelli et al., 2003; Allison et al., 2006). This code provides features like tracking particles, includes many physical models, describes interactions of particles step-by-step and allows the generation of many complex structures offering a wide range of applications. Exemplary, applications are in the field of particle physics, radiation physics, medical imaging, space research, radiation protection and nuclear physics.

Based on GEANT4, the toolkit TOPAS (*TOol for Particle Simulations*) was developed to offer a wide range of users, especially medical physicists, the access to Monte Carlo simulations (Perl et al., 2012; Faddegon et al., 2020; Testa et al., 2013). Therefore, the focus is on applications in medical physics, accessible without the need for advanced programming skills. For example, the design of detectors, the performance of ionization chambers and patient dose distribution can be calculated with this tool. In TOPAS, all GEANT4 data and physics list are implemented.

In TOPAS and GEANT4, the simulations of physical interactions of radiation with matter can be performed in two ways: using the condensed history (CH) approach and the track structure (TS) approach. Due to its time efficiency, most applications are performed with the CH approach. Here, single scattering events are combined into multiple scattering events, whereby particle energy and angle at the end of the defined step width are statistically selected by algorithms. The CH approach is sufficient for simulations on macroscopic levels, since residual ranges of a few micrometers remain as residual kinetic energies are in the order of 1 - 10 keV (electrons with an energy of 10 keV have a residual range in water of ca. 2.5 μm).

This highlights the requirement of the second method, the TS approach: For experiments on biological levels, such as the investigation of the biological effectiveness, resolutions in the range of a few nanometers to micrometers are necessary corresponding to the scale of DNA and cell components. To achieve this resolution, each process is simulated step-by-step down to kinetic energies of a few eV, resulting in residual ranges of less than 1 nm. However, particularly for track-structure data on smaller scales, the experimental setup can be highly complex, leading to a limited availability of experimental cross-section data. For example, to cover the data of electrons below 100 eV, experiments are conducted with water vapor instead of liquid water since in this energy regime, experiments are too difficult to perform with liquid water. However, the conversion of electron cross-section data of water vapor to liquid water comes with further uncertainties (Michaud et al., 2003). Thus, a validation of the simulation data is necessary and needs further improvement.

Access to the relevant models and data required for the TS approach is provided by the corresponding extensions GEANT4-DNA and TOPAS-nBio (Incerti et al., 2010a; Schuemann et al., 2019). These extensions allow the simulation of radiation-induced intracellular damage to DNA. However, cross-section data are currently limited to water and are not available for other materials. In addition to physical models, chemical models are included, enabling the simulation of both direct and indirect DNA damages (Karamitros et al., 2011, 2014; Ramos-Méndez et al., 2018). With these features, the extension TOPAS-nBio is a suitable tool to gain insights into the mechanisms of the biological effectiveness of different radiation types as a supplement to experiments. Incorporating Monte Carlo simulations into biological experiments has several advantages. While the cost of experiments can be quite high due to laboratory equipment, expensive hardware, materials, and staff costs, Monte Carlo simulations are much less expensive. In addition, they are less complex to perform and can be carried out quickly. If needed, they can be easily repeated and a large amount of data can be collected. Furthermore, there is no need to obtain an approval by any ethical committee for the application. Monte Carlo simulations offer the advantage that individual variables can be well controlled by adjusting simple parameters in the code. In biological experiments, full control is not always given or can only be achieved in a very effortful way, like the exact adjustment of a certain oxygen concentration. Nevertheless, it is very important that the fundamental models underlying the code are thoroughly validated through benchmark experiments. Therefore, simulations and experiments should always complement each other in order to obtain a comprehensive understanding of complex research questions.

CHAPTER 2

Aim of this dissertation

The overall aim is to explore key factors influencing biological effects of protons applying Monte Carlo simulations. Therefore, the Monte Carlo code needs to be configured accurately and thoroughly validated against experimental results to gain a feasible and reliable tool for examining the biological effect of protons. The primary focus of this research was to investigate physical and chemical interactions of ionizing radiation at nanodosimetric scales using TOPAS-nBio, which further provides a foundation for validating the code.

It is crucial to understand physical and chemical interactions directly at dimensions in the order of the DNA, the primary target in radiotherapy, since here, at the DNA, the main biological effects are initiated, leading to significant damage to the cell. Within this framework, the nanodosimetric tool TOPAS-nBio was used to examine physical and chemical interactions on nano- and micrometer levels. Especially, since the number of Monte Carlo tools designed for studying interactions at nanodosimetric levels, along with the expertise in handling simulations with these tools is currently limited, this study aims to fill a critical gap.

In a first step, the effect of different physics models available in TOPAS-nBio was examined by simulating the physical stage of interactions. The focus was on the distribution, frequency and energy depositions of inelastic processes which may cause direct DNA damages as well as induce chemical radicals. In a next step, simulations were extended by simulations of chemical interactions. Especially, the impact of different dose rates, expressed through inter-track interactions, on the dynamics of radiochemistry was investigated with relation to the question of the origin of the FLASH effect applying ultra-high dose rates in radiotherapy. Therefore, a method had to be developed to enable inter-track interactions at the chemical stage in TOPAS-nBio. Lastly, the developed method facilitating inter-track interactions was compared by quantifying differences of G-values compared to simulation results performed with a second, independently developed method within TOPAS-nBio. In this way, it can be evaluated if the methods gain reliable and consistent results.

CHAPTER 3

Summary of the results and contributions

3.1 Article 1: Investigating the feasibility of TOPAS nBio for Monte Carlo track structure simulations by adapting GEANT4-DNA examples application

3.1.1 Summary of article 1

In the first article (Derksen et al., 2021), the Monte Carlo simulation tool TOPAS-nBio was used to investigate physical interactions on nanometer scales on a step-by-step approach. The frequency of electron, proton and hydrogen processes occurring along the interactions of an 100 keV proton beam was investigated applying three different pre-defined physics lists that are recommended by GEANT4: G4EmDNAPhysics_option2, G4EmDNAPhysics_option4 and G4EmDNAPhysics_option6 (Incerti et al., 2018). The lists vary in terms of the models applied for individual electron processes, while the processes for all other particles (protons, neutral hydrogen, alpha particles, ${}^7\text{Li}$, ${}^9\text{Be}$, ${}^{11}\text{B}$, ${}^{12}\text{C}$, ${}^{14}\text{N}$, ${}^{16}\text{O}$, ${}^{28}\text{Si}$, ${}^{56}\text{Fe}$, photons) remain consistent across all models. The G4EmDNAPhysics_option2 (option 2) physics list was the first developed list implemented in GEANT4-DNA that used discrete physical models for energies in the eV regime (Incerti et al., 2018, 010b). In comparison to the other two examined options, this list includes models for simulating the thermalization of sub-excited electrons via vibrational excitation (Melton, 1972) and dissociative attachment (Michaud et al., 2003). G4EmDNAPhysics_option4 (option 4), provides updated inelastic cross-section data due to refinements of the model of option 2 and applies a different elastic scattering model (Kyriakou et al., 2015). However, cross-section data are limited up to electron energies of 10 keV, whereas the cross-section data of option 2 are available up to 1 MeV. The physics list G4EmDNAPhysics_option6 (option 6) implements an independent set of physics models and cross-section data as applied in the CPA100 track structure code for energies up to 256 keV (Bordage et al., 2016).

In addition to the examined processes of the different physics list options using a proton beam,

the frequency and energy depositions of each process using electrons of an initial energy in the range of 10 - 60 eV were investigated applying the default physics list option 2. This range of initial electron energies was selected since, on the one hand, the mean energy of secondary electrons produced by ions of clinically relevant energies is about 50 - 60 eV and the most probable energy is around 10 eV (Pimblott and LaVerne, 2007). On the other hand, this tool is especially developed to consider the impact of those small particle energies. The step-by-step physical interactions were investigated in a water-filled cube with an edge length of 100 μm in order to ensure that the complete particle track of each particle is smaller than the dimension of the geometry. To investigate the physical interactions, TOPAS-nBio offers the possibility to monitor detailed information of a particle's track like position, energy and process of each step. The final quantities of interest (process counts, mean and maximum deposited energy) were calculated based on this information.

In figure 3.1 (corresponding to figure 2 in **article 1**), the influence of using three different physics lists on the frequency of electron, hydrogen and proton processes is shown separately for each particle type. For this purpose, the individual processes, that are outlined for each step of a particle in TOPAS-nBio, were quantified by summarizing the same types of interactions of 100 primary protons with an energy of 100 keV. For the comparison, the percentage differences of each combination of two physics list options shown as vertical bars in figure 3.1 were calculated individually for the different processes for electrons, protons and hydrogen. A short description of each process is given in table 3.1. Regarding the electron processes, percentage differences are on average 46% and can amount up to 255% (excitation, comparing option 2 and option 4). However, these great variations are not observed for the hydrogen and proton processes. For those processes, the percentage differences are at maximum 0.2%. The reason for this is that the models of the processes between the applied physics lists only vary for electrons, not for hydrogen and proton processes. Thus, the deviations between the physics lists of proton and hydrogen processes are of statistical nature.

In figure 3.2 (corresponding to figure 5 in **article 1**), the frequency and energy depositions per electron process using the default physics list option of TOPAS-nBio (option 2) are shown in dependence on the initial electron energy of 10 - 60 eV. In figure 3.2(a) the frequency of processes is shown. In comparison to figure 3.1, here two more processes (vibrational excitation and attachment) are depicted since these are only part of this physics list option and not considered in the other options. In general, the number of processes increases with increasing electron energy. The most common process is elastic scattering, followed by vibrational excitation which

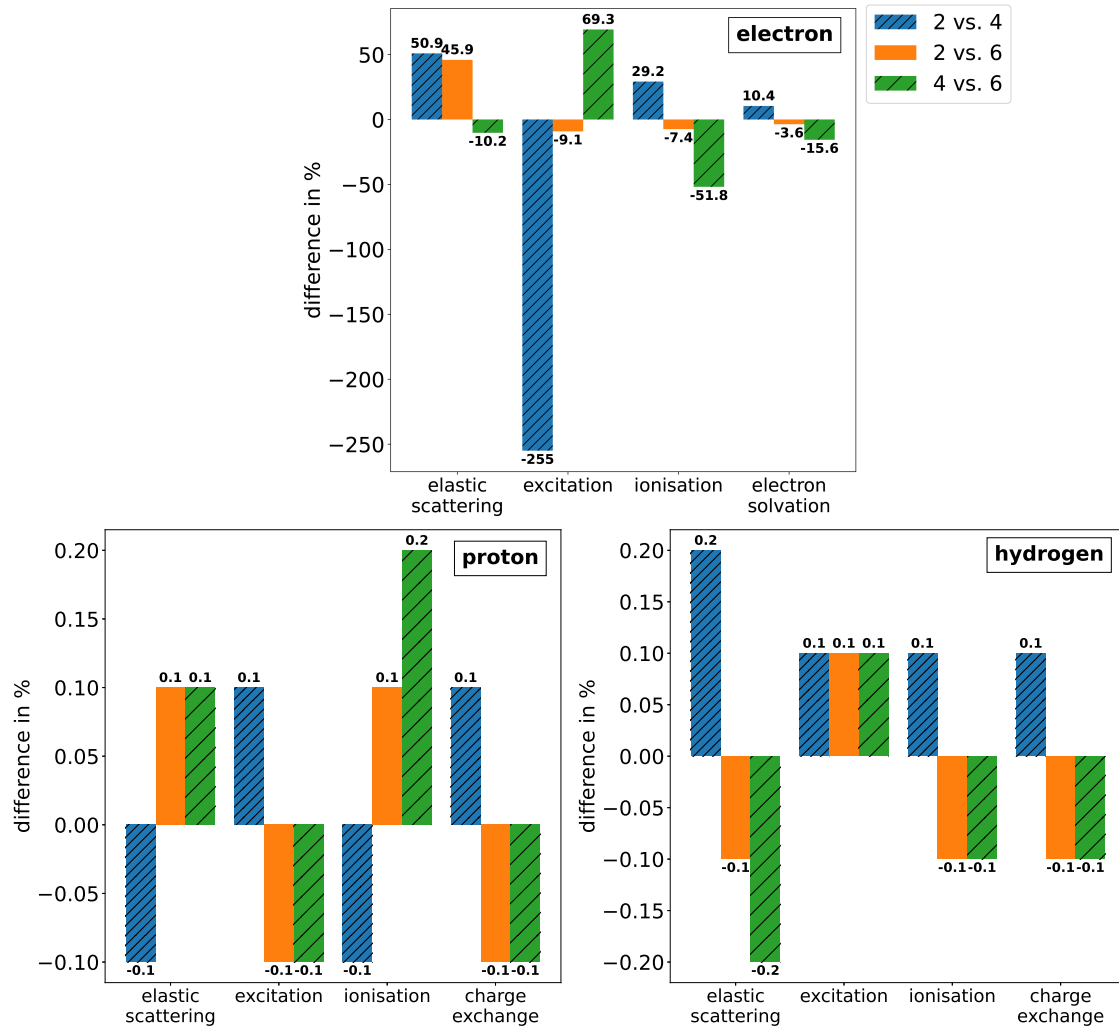


Figure 3.1: Comparison of the process counts of electron, proton and hydrogen processes summarized from 100 primary protons of 100 keV energy using three different physics list options (G4EmDNAPhysics_option2, G4EmDNAPhysics_option4 and G4EmDNAPhysics_option6). When calculating the percentage differences, the physics list option, which is listed in first position in the legend, was set as basis of comparison. Figure taken from (Derksen et al., 2021). © Institute of Physics and Engineering in Medicine. Reproduced with permission. All rights reserved.

Table 3.1: Brief overview of all possible electron processes included in GEANT4-DNA. Table taken and adapted from (Derksen et al., 2021). © Institute of Physics and Engineering in Medicine. Reproduced with permission. All rights reserved.

Process name	Definition
Attachment	Electron sub-excitation process; capture of an electron by an electrically neutral molecule, when the kinetic energy is less than the ionization potential and matches the quasibound state of the molecule. OH^- , H^- and O^- ions are produced by the electron interacting with liquid water (Denifl et al., 2012; Melton, 1972).
Charge exchange	Capture or loss of an electron, influencing the electrical charge of the particle.
Elastic scattering	Scattering of the particle interacting with free and bound atoms without an energy transfer.
Electron solvation	Accumulation of water molecules around a free electron. In GEANT4-DNA, the tracking cut is represented by this process when chemical processes are inactivated. Electrons that reach the tracking cut are then assumed to be solvated (Incerti et al., 2018).
Electronic excitation	Energy transfer to a bound electron of a molecule, with the result that it is excited to a higher energy level. Consideration of the five electron excitation states of liquid water.
Ionization	Detachment of an electron from the electron shell of a neutral atom or molecule, resulting in a positive ion. Taking into account the ionization energies for four valence electrons and the K-shell.
Vibrational excitation	Small energy depositions inducing excitation of the vibrational state of the interacting molecule (Michaud et al., 2003). Nine excitation phonon modes are taken into account.

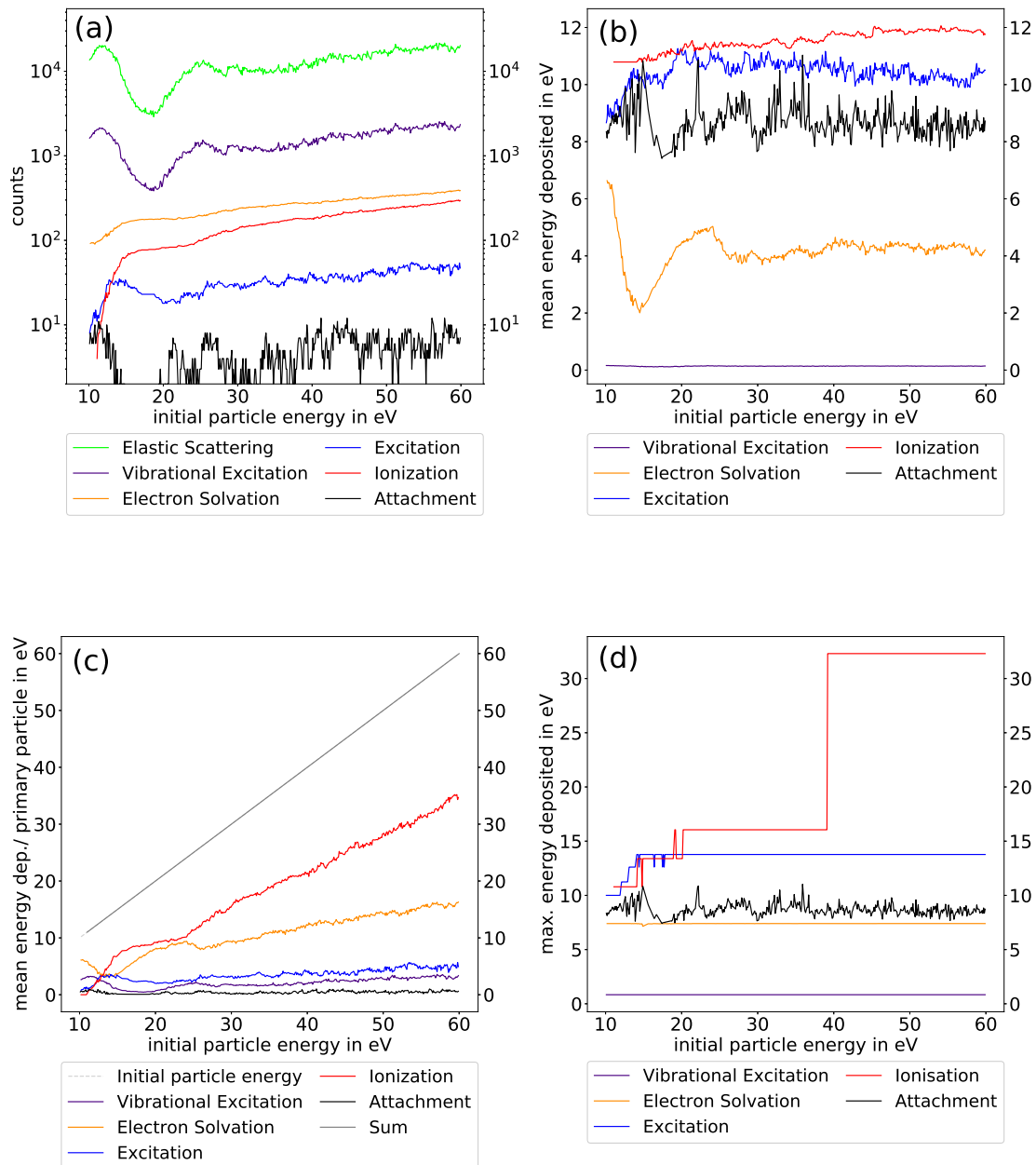


Figure 3.2: Frequency and energy depositions of all electron processes with initial energies in the range of 10-60 eV using G4EmDNAPhysics_option2. (a) Frequency of processes from a total of 100 primary electrons including electrons of later generations, (b) mean deposited energy of all primary events of each process, (c) sum of the deposited energy per process in average of all primary electrons, and (d) maximum deposited energy per process. Considering (b) and (c), uncertainties are not shown for a more concise presentation of results. Since ionizations only occur above an initial energy of 11 eV, the corresponding results were only plotted for initial energies above this minimum energy. Figure taken from (Derksen et al., 2021). © Institute of Physics and Engineering in Medicine. Reproduced with permission. All rights reserved.

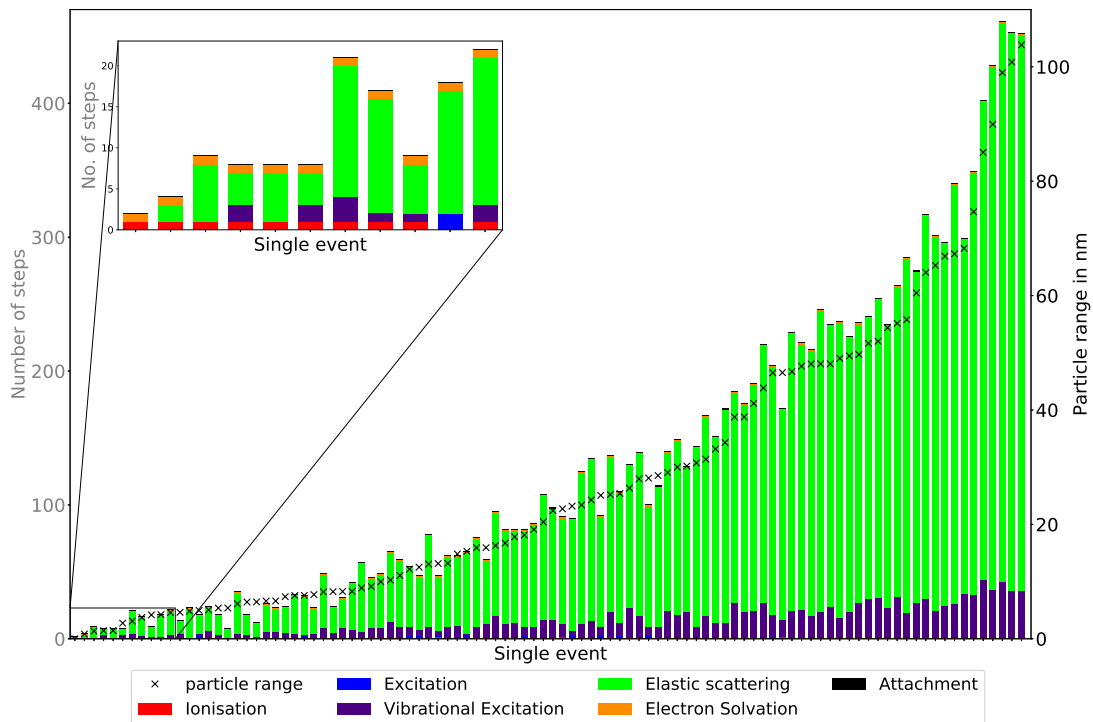


Figure 3.3: Illustration of the number of steps per process (bars) and range (x) for 100 individual events of an energy of 24.2 eV. Each process is illustrated in a different color. The more steps of a process, the larger its bar. Events are sorted according to their range. In a zoom-in view, the results with the smallest ranges are represented. Figure taken from (Derksen et al., 2021). © Institute of Physics and Engineering in Medicine. Reproduced with permission. All rights reserved.

is caused by the fact that these two processes deposit no energy at all (elastic scattering) or only well below 1 eV (vibrational excitation), which is shown in figure 3.2 (b) - (d). Fluctuations in the frequency, especially for vibrational excitation and elastic scattering, are caused due to the different energy thresholds that are required for a discrete ionization or excitation level depositing the corresponding energy. In figure 3.2(d), the maximum deposited energy is depicted for each process in dependence on the initial electron energy. For both, ionizations and excitation, the maximum deposited energy as a function of initial energy increases in certain energy steps, illustrating energies which reach specific energy thresholds.

As shown in figure 3.2 (b) - (d), the most energy is deposited by ionization and excitation processes. Thus, the more ionizations or excitation occur, the less kinetic energy remains and the number of steps and processes followed by those processes decreases.

The following figure 3.3 (corresponding to figure 6 in **article 1**) illustrates those correlations by showing each step, process and range of 100 individual electron tracks for an exemplary energy of 24.2 eV. For each individual track, one vertical bar is depicted on the x-axis. The correspond-

ing number of steps is shown on the left y-axis whereas the associated range is shown on the right y-axis. With an increasing number of steps, the amount of vibrational excitation and elastic scattering increases as well as the electron range. In contrast, the more ionizations or excitations occur in one track, the number of steps decreases as well as the electron range. Even though the initial energy of all electron tracks remains the same, the individual tracks diverse in their range, number of processes and amount of energy deposited in one step.

The study demonstrated significant variability in process frequencies of electrons arising from their different modelling in the three physics list options, manifesting differences of up to 255%. For proton and hydrogen processes, differences were negligible between different physics lists. Furthermore, single particle trajectories exhibited considerable diversity significantly influenced by the process and energy deposition of each step.

3.1.2 Contributions

L. Derksen wrote the manuscript and designed the study. She performed all Monte Carlo simulations with TOPAS-nBio and conducted the analysis of the data.

T. Pfuhl validated the implementation of GEANT4-DNA data in TOPAS-nBio by performing some of the simulations using GEANT4-DNA.

R. Engenhardt-Cabillic substantively revised this manuscript and was supervising the work.

K. Zink helped to discuss the results and interpreting the collected data.

K.-S. Baumann supervised the work and assisted in the design of the study. He supported performing the simulations in TOPAS.

3.2 Article 2: A method to implement inter-track interactions in Monte Carlo simulations with TOPAS-nBio and their influence on simulated radical yields following water radiolysis

3.2.1 Summary of article 2

In the second article (Derksen et al., 2023), the Monte Carlo tool TOPAS-nBio was employed to investigate the impact of radiation on the chemical stage. In particular, the implementation of inter-track interactions and their effect on the chemical stage were the focus of this study. Therefore, a method was developed to simulate those chemical inter-track reactions which were not included per default in TOPAS-nBio.

In TOPAS-nBio, the simulation of a particle track, including physical and chemical interactions, is performed independently of other tracks and all tracks are simulated sequentially, making inter-track interactions impossible. However, all chemicals produced by the same primary particle, involving all chemicals produced by secondary particles of the same track, can react with each other. Thus, inter-track interactions were enabled by labeling primary particles as secondaries of one primary track. This adjustment allowed chemical radicals produced by initially different primary particles to interact. In order to achieve this, a phase space file, containing particle information such as position, direction, energy, and a label indicating the primary or secondary status of a particle, was modified by changing a particle's status from primary to secondary. This phase space file was first scored in the simulations applying the initial particle source, then modified and subsequently used as the source in the following simulation. Initially, in the phase space file, all particles shared the same label indicating them as primary particles since only primary particles were scored when generating the phase space file. To facilitate inter-track interaction of N primary tracks, $N - 1$ tracks were consecutively labeled as secondaries. This way, N particles were simulated simultaneously, and all chemicals produced by these N tracks could interact.

First, this method was applied for investigating the impact of inter-track interactions in simulations with a 60 eV electron source. Due to the fact that the generation of chemical radicals through radiolysis relies on physical inelastic interactions, having a detailed understanding of the precise step-by-step physical interactions is highly advantageous. Hence, the physics list G4EmDNAPhysics_option2 in detailed examined in the previous article was chosen. Furthermore, using this low energy, simulation times are in acceptable range and the yield of chemicals allows step-by-step tracking of each reaction without losing clarity or requiring excessive effort. Once a fundamental understanding of the influence of inter-track interaction was achieved by these simulations, further simulations with proton beams of 10 and 100 MeV were performed.

For all particle sources, G-values were simulated to investigate the influence of inter-track interactions on the dynamics of the chemical stage. The G-value $G(t)$ is defined as the total number $M(t)$ of molecules given at a specific time t normalized to 100 eV of deposited energy E whereas the chemical species may be consumed or produced through chemical reactions (see eq. 1.8 in 1.2). The amount of inter-track interactions was directly influenced and handled by systematically varying the number N of tracks that are able to perform inter-track interactions along each other between $N = 2$ and $N = 60$ using electrons and between $N = 2$ and $N = 100$ using protons. While for the electron simulations a sphere with radius of 1 μm was sufficient for calculating the G-value since all electron tracks and their chemicals stop in this geometry, using protons a sphere

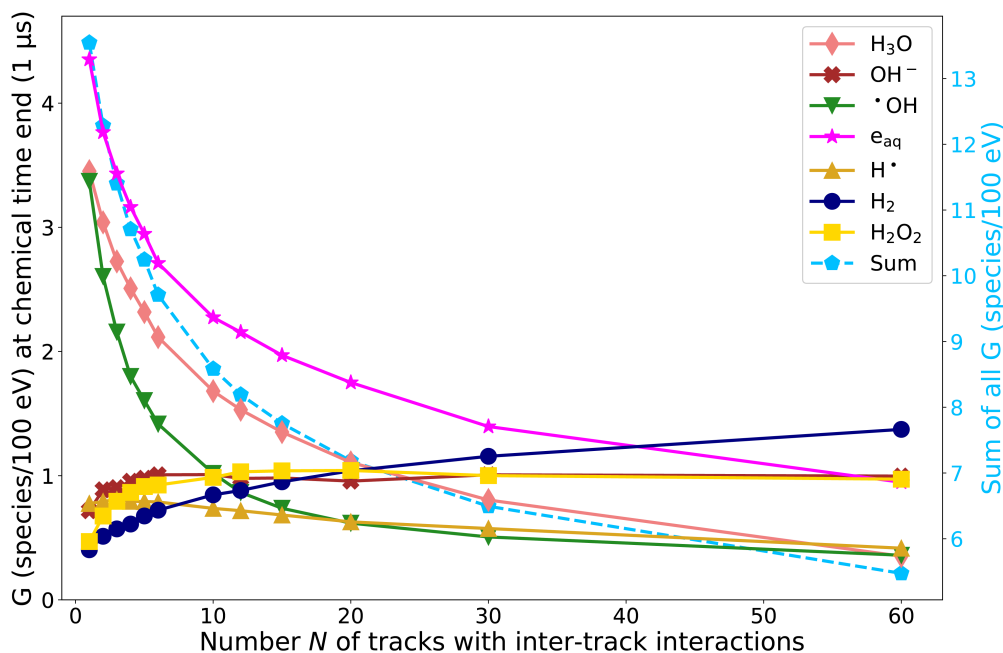


Figure 3.4: G-value in dependence of the number N of tracks with inter-track interactions for 60 eV electrons. Left axis: G-value for different chemical species at the end of the chemical stage at $t = 1 \mu\text{s}$. Right axis: total G-value of all molecules (dashed line). Data points are connected with a line for a more transparent visualization. The standard deviation ($k=1$) is smaller than the symbol size and, hence, not depicted. Figure taken and adapted from (Derksen et al., 2023). © Institute of Physics and Engineering in Medicine. Reproduced with permission. All rights reserved.

with a radius of $5 \mu\text{m}$ was chosen corresponding to the dimension of cell nuclei. The chemical stage was investigated by applying a list of 26 possible chemical reactions, including eleven different chemical species. The chemical reactions are listed in table 3.2.

Figure 3.4 (corresponding to figure 3 in **article 2**) presents the influence of inter-track interactions on the G-value as a function of the number N of tracks with inter-track interactions using electrons. While on the left axis, the G-values for various chemical species are displayed separately, the right axis illustrates the total G-value, G_{all} , adding up the G-values of all molecular species. All G-values are shown at the end of the chemical stage at $1 \mu\text{s}$. For reference, the G-value without inter-track interactions is shown at $N=1$. With increasing N , a reduction of the G-values $\bullet\text{OH}$, e_{aq} and H_3O is observed. In contrast, the G-value of OH^- , H_2O_2 and H_2 increases with increasing N . As an example, the G-value of H_2O_2 increases by a factor of two through inter-track interactions from the reference at $N=1$ to $N=60$. However, for H^\bullet no significant alteration of the G-values as a function of N was observed. Even though the variation of the G-value with N varies depending on the chemical species, a clear tendency of G_{all} can be identified. With increasing N , G_{all} decreases significantly. However, the higher N , the less the changes

Table 3.2: Chemical reactions and reaction rates k considered in the chemical stage. H_2O molecules are not listed in the reaction formulas, and no product means that the reaction product is H_2O . Table taken and adapted from (Derksen et al., 2023). © Institute of Physics and Engineering in Medicine. Reproduced with permission. All rights reserved.

No.	Reaction	k (10^{10} /M/s)*
1	$e_{\text{aq}}^- + e_{\text{aq}}^- \longrightarrow 2\text{OH}^- + \text{H}_2$	0.647
2	$e_{\text{aq}}^- + \bullet\text{OH} \longrightarrow \text{OH}^-$	2.953
3	$e_{\text{aq}}^- + \text{H}\bullet \longrightarrow \text{OH}^- + \text{H}_2$	2.652
4	$e_{\text{aq}}^- + \text{H}_3\text{O} \longrightarrow \text{H}\bullet$	2.109
5	$e_{\text{aq}}^- + \text{H}_2\text{O}_2 \longrightarrow \text{OH}^- + \bullet\text{OH}$	1.405
6	$\bullet\text{OH} + \bullet\text{OH} \longrightarrow \text{H}_2\text{O}_2$	0.475
7	$\bullet\text{OH} + \text{H}\bullet \longrightarrow \text{No product}$	1.438
8	$\text{H}\bullet + \text{H}\bullet \longrightarrow \text{H}_2$	0.503
9	$\text{H}_3\text{O} + \text{OH}^- \longrightarrow \text{No product}$	11.031
10	$\text{H}_2 + \bullet\text{OH} \longrightarrow \text{H}\bullet$	0.0045
11	$\bullet\text{OH} + \text{H}_2\text{O}_2 \longrightarrow \text{HO}_2$	0.0023
12	$\bullet\text{OH} + \text{HO}_2 \longrightarrow \text{O}_2$	1.0
13	$\bullet\text{OH} + \text{O}_2^- \longrightarrow \text{O}_2 + \text{OH}^-$	0.9
14	$\bullet\text{OH} + \text{HO}_{-2} \longrightarrow \text{HO}_2 + \text{OH}^-$	0.9
15	$e_{\text{aq}}^- + \text{HO}_2 \longrightarrow \text{HO}_{-2}$	2.0
16	$e_{\text{aq}}^- + \text{O}_2 \longrightarrow \text{O}_2^-$	1.9
17	$e_{\text{aq}}^- + \text{O}_2^- \longrightarrow \text{OH}^- + \text{HO}_{-2}$	1.3
18	$\text{H}\bullet + \text{H}_2\text{O}_2 \longrightarrow \bullet\text{OH}$	0.01
19	$\text{H}\bullet + \text{HO}_2 \longrightarrow \text{H}_2\text{O}_2$	2.0
20	$\text{H}\bullet + \text{O}_2 \longrightarrow \text{HO}_2$	2.0
21	$\text{H}\bullet + \text{OH}^- \longrightarrow e_{\text{aq}}^-$	0.002
22	$\text{H}\bullet + \text{O}_2^- \longrightarrow \text{HO}_{-2}$	2.0
23	$\text{H}_3\text{O} + \text{O}_2^- \longrightarrow \text{HO}_2$	3.0
24	$\text{H}_3\text{O} + \text{HO}_{-2} \longrightarrow \text{H}_2\text{O}_2$	2.0
25	$\text{HO}_2 + \text{HO}_2 \longrightarrow \text{H}_2\text{O}_2 + \text{O}_2$	0.000076
26	$\text{HO}_2 + \text{O}_2^- \longrightarrow \text{O}_2 + \text{HO}_{-2}$	0.0085

* $\text{M} = 1 \text{ mol/dm}^3$

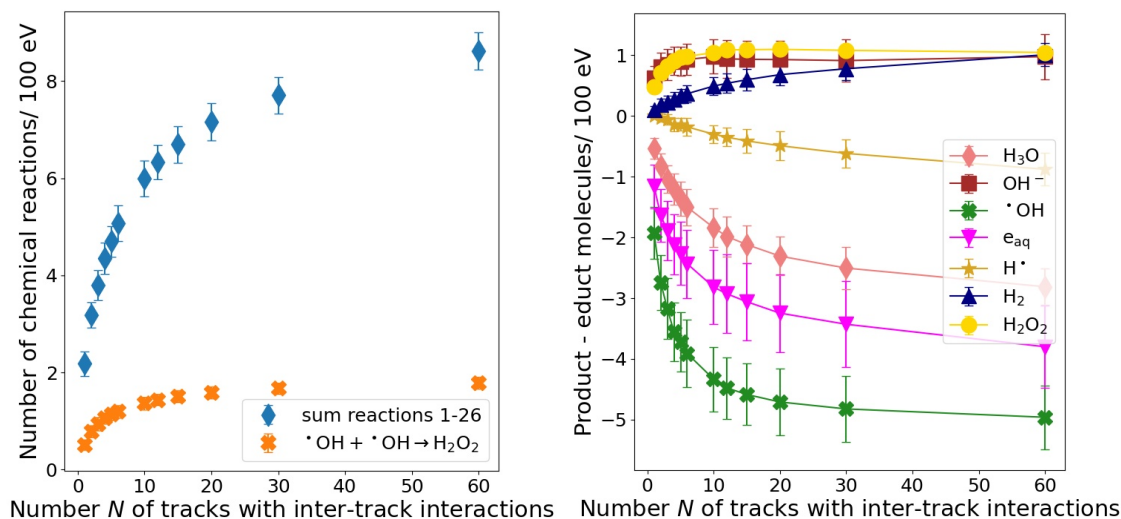


Figure 3.5: Investigation of chemical reactions during the overall chemical stage in dependence of the number N of tracks with inter-track interactions. Left: Total number of chemical reactions performed in the chemical stage normalized to 100 eV of deposited energy. Right: Difference of the number of product molecules and educt molecules for each chemical species normalized to 100 eV of deposited energy. Statistical uncertainties are represented by vertical error bars and correspond to one standard deviation. Figure taken and adapted from (Derksen et al., 2023). © Institute of Physics and Engineering in Medicine. Reproduced with permission. All rights reserved.

in the G-value. An explanation of the general development of the G-value is that with increasing N more inter-track interactions occur as the probability of chemical reactions increases due to a higher density of radicals. This is further demonstrated in figure 3.5 (corresponding to figure 4 in **article 2**), showing details of chemical reactions in dependence of N . Figure 3.5 (left) shows the total number of chemical reactions during the chemical stage up to $t = 1 \mu\text{s}$ normalized to 100 eV of deposited energy as a function of N . With increasing N , the number of chemical reactions increases significantly. For higher N , the curve shows a flattening trend, aligning with the observed saturation of the total G-value. As an example, the reaction of two $\cdot\text{OH}$ molecules to H_2O_2 is additionally shown to illustrate the increasing G-value of H_2O_2 and the decreasing G-value of $\cdot\text{OH}$ with increasing N displayed in figure 3.4. In figure 3.5, the differences of the number of chemical reactions producing or consuming each chemical are shown for all molecule types in dependence of N . For H_2O_2 , H_2 and OH^- an increasing number of product molecules with increasing N is registered whereas for all other molecules (H^\bullet , H_3O^+ , e_{aq} , $\cdot\text{OH}$) less product than educt molecules are observed. This results from a more pronounced increase of the frequency of certain chemical reactions in comparison to other reactions with increasing N . Consequently, this accounts for the varying increase or decrease of G-values for various chemicals as shown in figure 3.4.

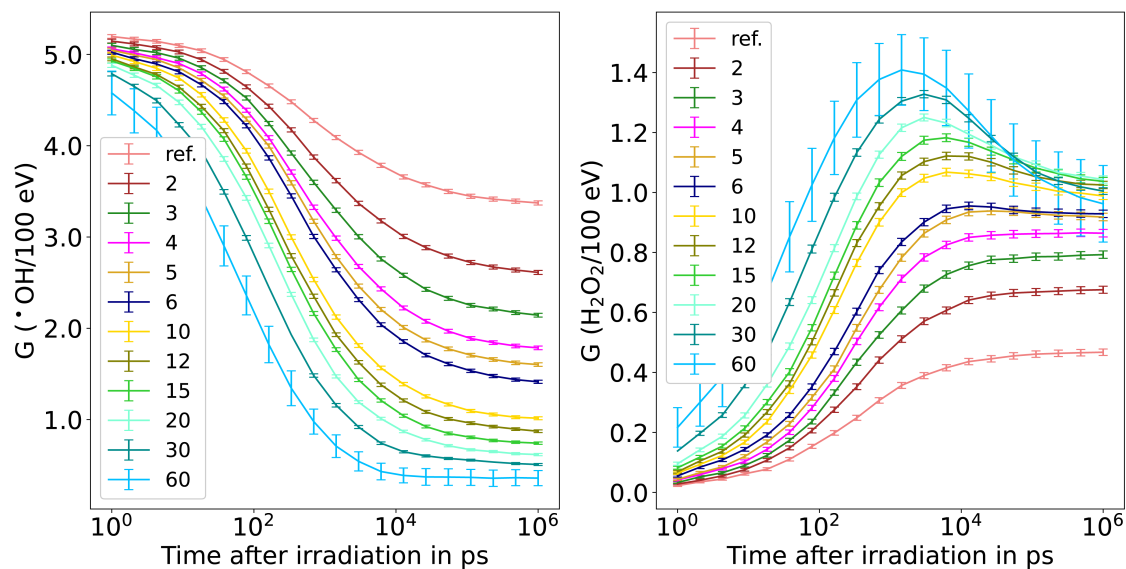


Figure 3.6: Time-dependent G-values of $\bullet\text{OH}$ (left) and H_2O_2 (right) for different numbers N of tracks with inter-track interaction. Data points are connected with a line for a more transparent visualization. The time on the x-axis is scaled logarithmically. Statistical uncertainties are represented by error bars and correspond to one standard deviation. Figure taken from (Derksen et al., 2023). © Institute of Physics and Engineering in Medicine. Reproduced with permission. All rights reserved.

In order to obtain additional insights into how inter-track interactions impact the dynamics of the chemical stage, time-resolved G-values were further examined. Figure 3.6 (corresponding to figure 5 in **article 2**) shows time-dependent G-values in the range of 1 ps to 1 μs for $\bullet\text{OH}$ (left) and H_2O_2 (right) using different N . For comparison, time-dependent G-values without inter-track interactions are also depicted and denoted with "ref.". Regarding $\bullet\text{OH}$, the G-values decrease for all N with time. A discrepancy of the G-values between different N can already be observed at the beginning of the chemical stage at 1 ps. This implies that the chemical density at 1 ps is sufficiently high reducing the need for chemicals to diffuse longer distances to meet another reactant. The same trends are observed for H_2O_2 . Also in this case, the effect of inter-track interactions can already be observed at 1 ps. But differently to $\bullet\text{OH}$, the G-value of H_2O_2 increases with time. For $N \geq 10$ a maximum G-value is obtained at around 1 ns, after which the G-value decreases. This characteristic behavior can be explained by an increase of chemical reactions consuming H_2O_2 . At the beginning of the chemical stage and for small N , the overall amount of H_2O_2 is relatively low, making such reactions less likely to occur. However, the amount of H_2O_2 increases substantially over time for higher N , which subsequently facilitates reactions that consume H_2O_2 (see reactions 5, 11 and 18 in table 3.2). Regarding both molecule types, in most cases (except of $N = 60$) the G-value saturates to the end of the chemical stage. This validates that simulations up to 1 μs should be sufficient in those cases representing the yield of chemicals

after irradiation.

With the investigations using the 60 eV electron source, fundamental influences of inter-track interactions affecting the dynamics of the chemicals were presented. Thus, the effect of inter-track interactions was further examined using proton sources of different LET. Figure 3.7 (corresponding to figure 6 in **article 2**) shows the G-values for various chemicals (left axis) and for G_{all} (right axis) at the end of the chemical stage at $t = 1 \mu\text{s}$ in dependence of N simulating 10 MeV (upper graph) and 100 MeV (bottom graph) protons. Similar to the variations observed for G-values using electrons, the G-value of $\bullet\text{OH}$, H_3O and e_{aq} decrease with increasing N for both proton energies. While the G-value of $\text{H}\bullet$ decreases also using the 10 MeV source, it remains constant when applying the 100 MeV source. Additionally, the G-value of H_2 and OH^- increase with increasing N for both proton sources. Furthermore, the G-value of H_2O_2 shows a remarkable increase, rising from 0.4 species/100 eV for the reference simulation at $N = 1$ to 0.7 species/100 eV for $N = 60$ using the 100 MeV proton source. In contrast, there are negligible changes for varying N when applying the 10 MeV source. For both proton energies, G_{all} decreases with increasing N . Moreover, the G-value of the 100 MeV proton source is consistently higher than that of the 10 MeV. Previous studies have highlighted the dependence of the yield of chemicals on the LET explaining those effects (Burns and Sims, 1981; Ramos-Méndez et al., 2018). Using a source with a higher LET, the density of chemicals is increased, resulting in a higher frequency of chemical reactions and subsequently in a reduced G-value. Thus, the results using protons show that the LET of the source has an influence on the magnitude of the G-values as well as on the extent of variations in the G-value with respect to N .

In this study, a method for implementing inter-track interactions in TOPAS-nBio was presented. The examination of the impact of inter-track interactions demonstrated that these reactions led to a reduction in the total number of simulated radicals at the end of the chemical stage.

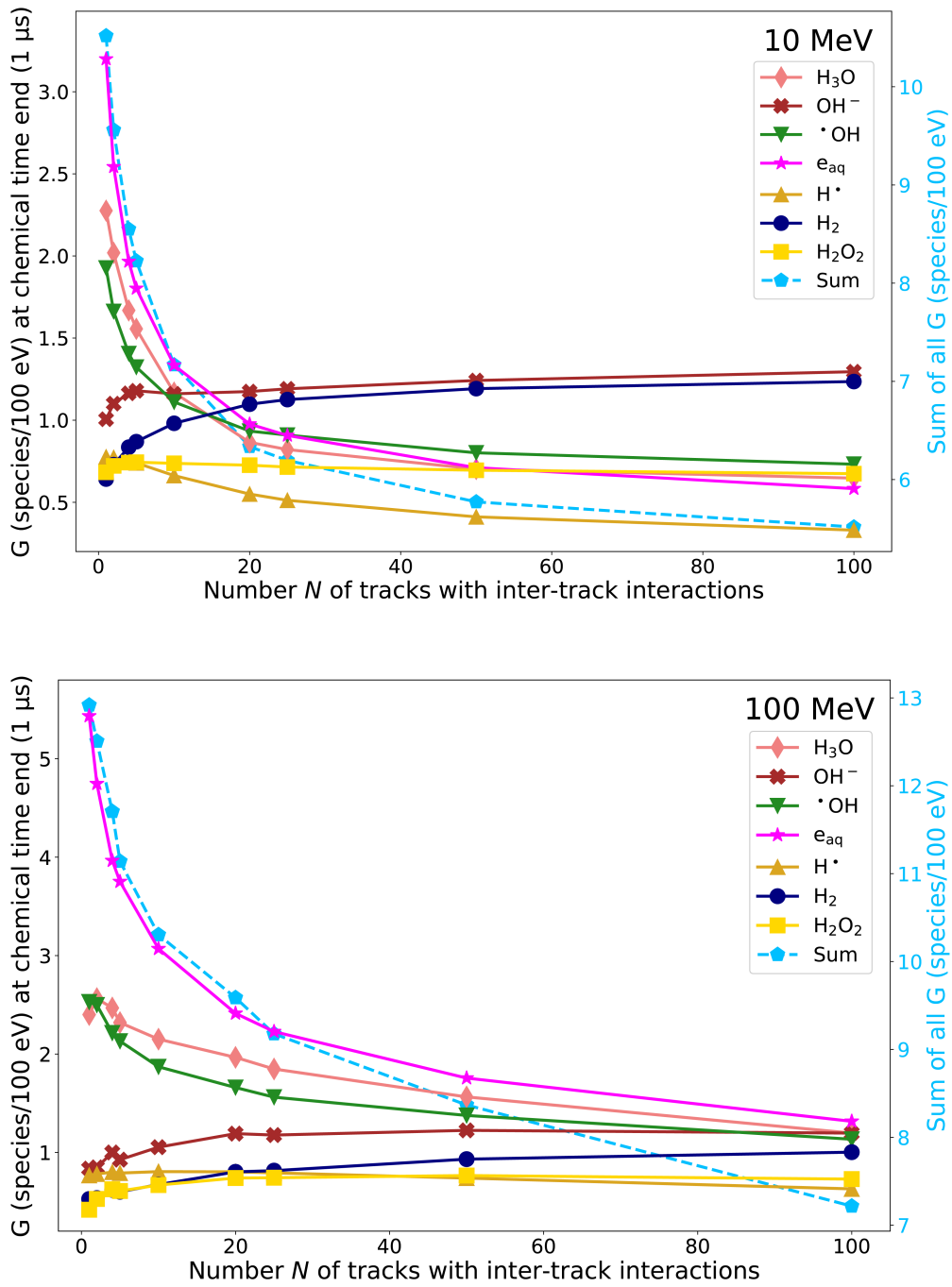


Figure 3.7: G-value in dependence of the number N of tracks with inter-track interactions for 10 MeV (top) and 100 MeV (bottom) protons. Left axis: G-value for different chemical species at the end of the chemical stage at $t = 1 \mu\text{s}$. Right axis: total G-value of all molecules (dashed line). Data points are connected with a line for a more transparent visualization. The standard deviation ($k = 1$) is smaller than the symbol size and, hence, not depicted. Figure taken and adapted from (Derksen et al., 2023). © Institute of Physics and Engineering in Medicine. Reproduced with permission. All rights reserved.

3.2.2 Contributions

L. Derksen designed the study and wrote the manuscript. She developed the method to enable inter-track interaction simulations in TOPAS-nBio and conducted all simulations.

V. Flatten helped with her knowledge in programming to develop the method enabling inter-track interactions in TOPAS-nBio.

R. Engenhardt-Cabillic substantively revised this manuscript and was supervising the work.

K. Zink had the idea to investigate the FLASH mechanism in TOPAS-nBio and aided in interpreting and discussing the results in relation to the FLASH effect.

K.-S. Baumann supervised the work and helped in designing the study. He aided designing the simulations set-ups, discussing the effect of inter-track interactions and substantively revised this manuscript.

3.3 Article 3: Comparison of two methods simulating inter-track interactions using the radiobiological Monte Carlo toolkit TOPAS-nBio

3.3.1 Summary of article 3

In the third article (Derksen et al., 2024), the developed method to enable inter-track interactions in TOPAS-nBio presented in **article 2**, further called the phsp method, was compared to a new method available in TOPAS-nBio provided by the TOPAS collaboration group, further referred to as the TsIRTInterTrack method.

As a reminder, the phsp method is based on a manipulation of a phase space file used in the simulations merging N initially primary particles as one primary particle by labeling $N - 1$ particles as secondaries. This allows the simultaneous simulation of all N tracks, encompassing both physical and chemical interactions, enabling inter-track interactions. In order to apply the TsIRTInterTrack method, available since TOPAS-nBio version 2.0¹, the toolkit provides a specified scorer named *TsIRTInterTrack* to investigate the impact of inter-track interactions on the yield of chemicals. With this scorer, the user can specify the number N of tracks with inter-track interaction. In this case, first, the physical stage of N tracks is performed independently and sequentially and second, the chemical stage of these N tracks is performed collectively, facilitating inter-track interactions.

¹The simulations applying the phsp method in **article 2** were performed with TOPAS-nBio 1.0, the latest version available during the study.

The TsIRTInterTrack method relies on a new implemented approach for simulating the yield of radicals on the chemical stage in TOPAS-nBio, known as the independent reaction time (IRT) method. While the default step-by-step (SBS) approach simulates chemical reactions based on in detail calculated diffusion steps, applying the IRT approach, chemical reactions are solely calculated based on the initial distribution of radicals and corresponding probability functions, making the simulations more time efficient. For additional information and a comparative analysis of the SBS and IRT approaches, refer to Ramos-Méndez et al. (2020). Even though the phsp method was initially developed and investigated using the SBS method, it is also applicable in conjunction with the IRT method. Thus, in this comparative study, the phsp method was also performed using the IRT approach in order to obtain consistent simulation setups.

To compare both independently developed methods, G-values of different numbers N of tracks with inter-track interactions were calculated. In the simulations, inter-track interactions were investigated using a 4.5 keV electron source placed in the center of a water-filled sphere of 5 μm radius. All simulation parameters, except for those affecting the modelling of inter-track interactions, were equal using both methods to ensure the same simulation setups.

In figure 3.8 (corresponding to figure 1 in **article 3**) and 3.9 (corresponding to figure 2 in **article 3**), the G-value, G_{all} , summarizing all molecule types, is shown using both methods in dependence of N , as well as for several various chemical species ($\bullet\text{OH}$, H_3O , OH^- , H_2 , H_2O_2 and e_{aq}) separately. Additionally, the G-value of recombined water molecules ($\text{H}_2\text{O}^{\text{f}}$) created through the reaction of $\bullet\text{OH}$ and H^{\bullet} or H_3O and OH^- (see reactions 7 and 9 in table 3.2 in section 3.2.1) are shown as the yield of $\text{H}_2\text{O}^{\text{f}}$ contributes to G_{all} . In the bottom part of each graph, the percentage difference between both methods is shown. Both methods exhibit a consistent decrease of G_{all} with increasing N , although some molecules, like H_2 and $\text{H}_2\text{O}^{\text{f}}$, show an increase. Compared to the previous presented work, differences in trends with N are attributed to diverse sources and an updated list of chemical reactions. Comparing G_{all} of both methods, it shows a high degree of agreement for all N and differs at a maximum of 0.2%. However, this minor deviation understates the discrepancies between the methods, which become evident when the molecules are individually examined and compared across the methods. Depending on the type of molecule, differences in the G-value up to 3.9% (H_2O_2) are observed. On average, considering all separately analyzed molecule types and all N , the deviations amount to 1.5%. Thus, the minimal differences between the two methods of G_{all} are the result of a compensation of positive and negative deviations between phsp and TsIRTInterTrack of separate molecule types.

Furthermore, time-dependent G-values were simulated using both methods enabling inter-track

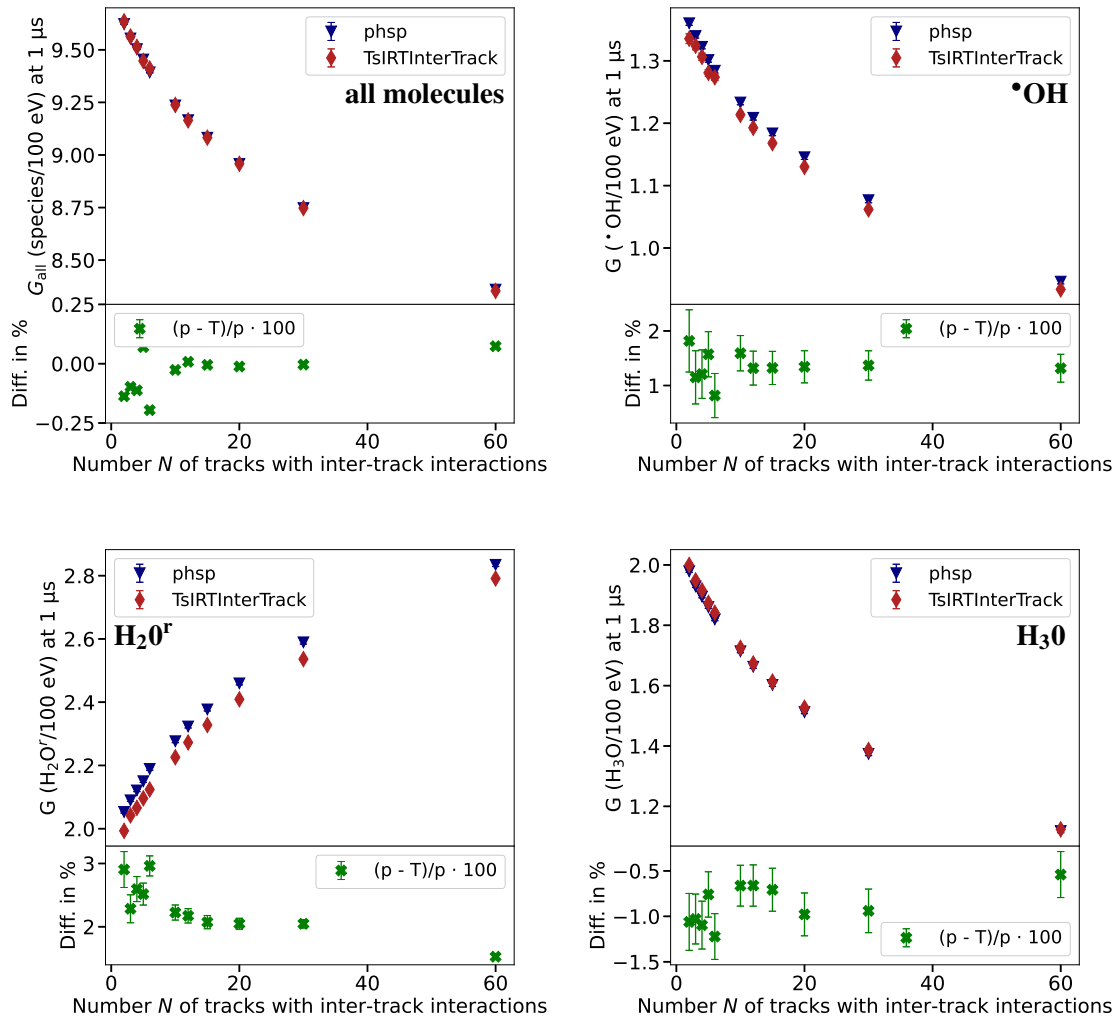


Figure 3.8: Comparison of the G-value G_{all} (upper left) and the G-values of $\bullet\text{OH}$ (upper right), H_2O^+ (bottom left) and H_3O (bottom right) at $1 \mu\text{s}$ using the phsp and TsIRTInterTrack method enabling inter-track interactions in dependence of the number N of tracks with inter-track interactions. In each upper panel, the G-value using both methods is depicted (phsp: blue triangles, TsIRTInterTrack: red diamonds) and in each bottom panel, the relative deviation of the TsIRTInterTrack (T) results to phsp (p) results are shown. Statistical uncertainties are represented by vertical error bars and correspond to one standard deviation. Figure taken from (Derksen et al., 2024). © Institute of Physics and Engineering in Medicine. Reproduced with permission. All rights reserved.

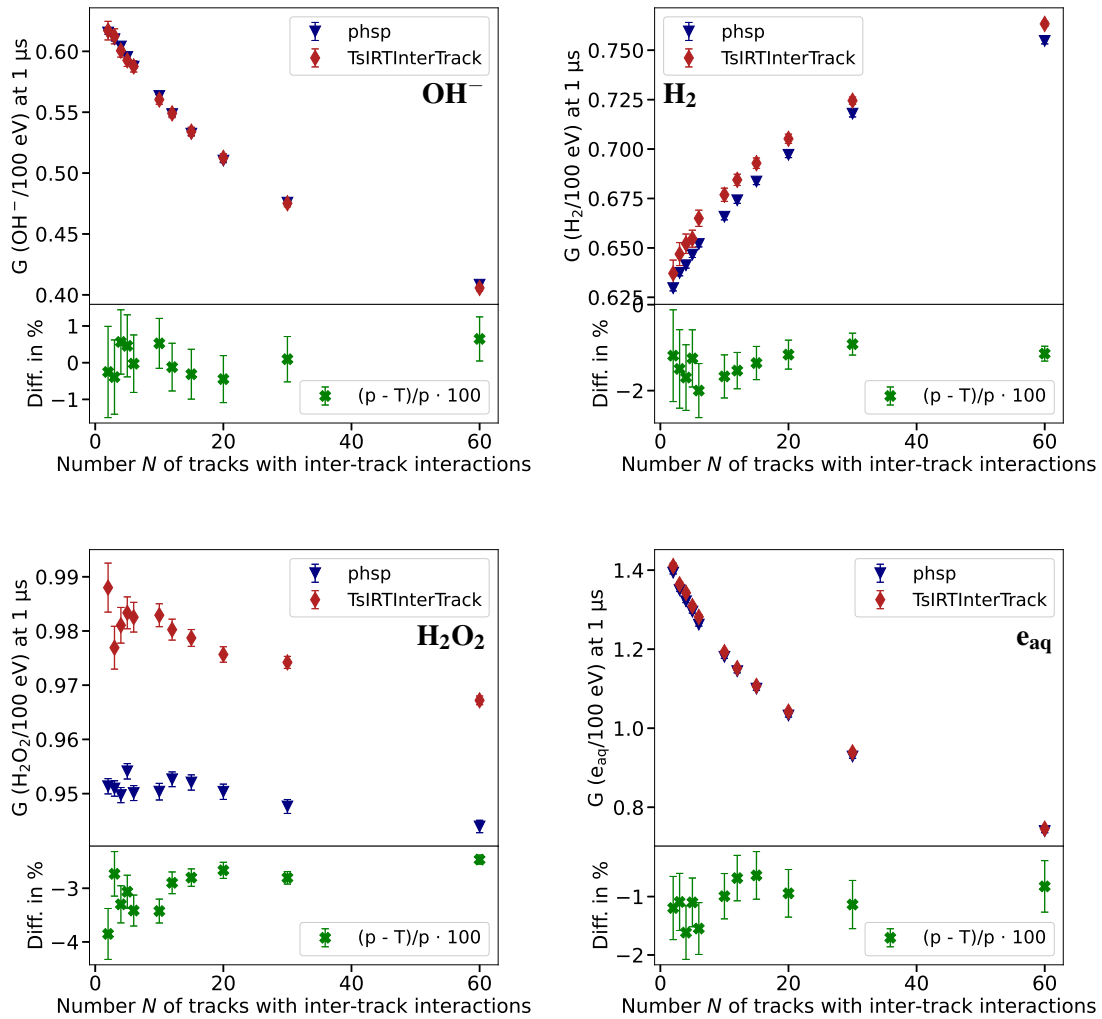


Figure 3.9: Comparison of the G-values of H^\bullet (upper left), H_2 (upper right), H_2O_2 (bottom left) and e_{aq} (bottom right) at $1 \mu\text{s}$ using the phsp and TsIRTInterTrack method enabling inter-track interactions in dependence of the number N of tracks with inter-track interactions. In each upper panel, the G-value using both methods is depicted (phsp: blue triangles, TsIRTInterTrack: red diamonds) and in each bottom panel the relative deviation of the TsIRTInterTrack (T) results to phsp (p) results are shown. Statistical uncertainties are represented by vertical error bars and correspond to one standard deviation. Figure taken from (Derksen et al., 2024). © Institute of Physics and Engineering in Medicine. Reproduced with permission. All rights reserved.

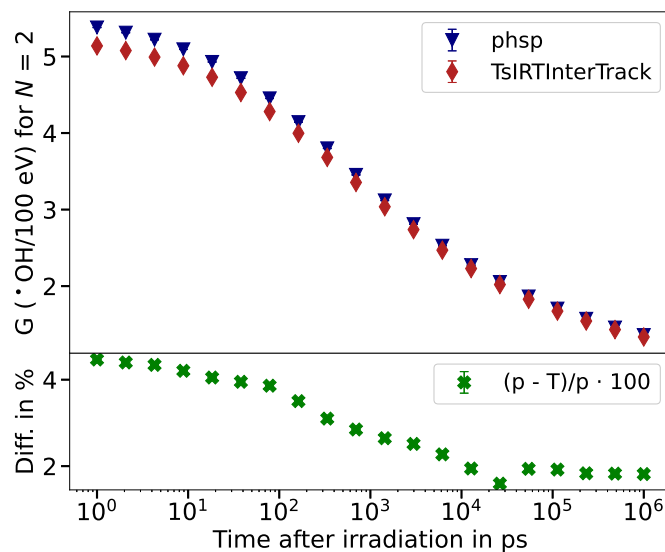


Figure 3.10: Comparison of time-dependent G-values of $\bullet\text{OH}$ for $N=2$ using the phsp and TsIRTInterTrack method. In the upper panel, the G-values are depicted for both methods and in the bottom panel, the difference of TsIRTInterTrack (T) results relative to phsp (p) results are shown. Statistical uncertainties represented by vertical error bars correspond to one standard deviation. Figure taken from (Derksen et al., 2024). © Institute of Physics and Engineering in Medicine. Reproduced with permission. All rights reserved.

interactions. In figure 3.10 (corresponding to figure 4 in **article 3**), time-dependent G-values of $\bullet\text{OH}$ are presented for $N=2$ using the phsp and TsIRTInterTrack method, as well as percentage differences between the methods. While percentage deviations are larger at the beginning of the chemical stage (1 ps: 4.5%), they decrease towards the end of the chemical stage (1 μs : 1.8%). Even though, in figure 3.10, this is shown for $N=2$ and $\bullet\text{OH}$ exemplary, this observation is consistent for all N and all molecule types. It demonstrates that although differences in the number of chemical species processing are present at 1 ps, chemical reactions reduce the differences towards the end of the chemical stage and the results of the two methods converge.

Even though the same TOPAS versions, the same physics and chemical modules including the same dissociation table for generating the chemical particles, chemical reactions and diffusion constants were applied for both methods generating inter-track interactions, notable differences of chemicals at the beginning of the chemical stage were observed. Only the implementation of inter-track interactions was different. To indicate the origin of these high differences at 1 ps, further examinations were conducted. Therefore, the number of inelastic processes and the number of chemical species processed at the beginning of the chemical stage were examined. Both of these factors play a crucial role in the production and dynamics of the yield of radicals in the chemical stage. Figure 3.11 (left) (corresponding to figure 3 in **article 3**), presents the number of

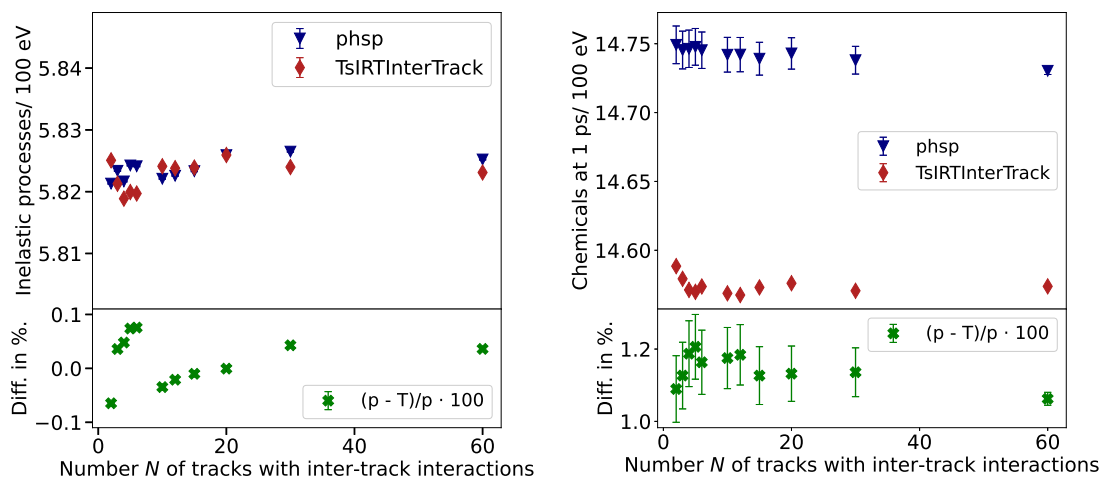


Figure 3.11: Number of inelastic processes and chemical species processing. Left: Number of inelastic processes creating chemical species normalized to 100 eV of deposited energy in dependence of N shown for both methods (phsp: blue triangles, TsIRTInterTrack: red diamonds). Right: Number of chemical species processing normalized to 100 eV of deposited energy in dependence of the number N of tracks with inter-track interactions using the phsp (blue triangles) and TsIRTIntertrack (red diamonds) method. Each bottom panel shows the relative difference of TsIRTIntertrack to phsp results. Statistical uncertainties are represented by vertical error bars and correspond to one standard deviation. Figure taken from (Derksen et al., 2024). © Institute of Physics and Engineering in Medicine. Reproduced with permission. All rights reserved.

inelastic processes normalized to 100 eV of deposited energy as a function of N . Differences in the number of inelastic processes are minimal, with an average difference of 0.01(4) % which is shown in the bottom part of the figure. This finding holds significance because the modelling of inter-track interactions should ideally only impact the chemical or at maximum the pre-chemical stage, which is proven with the results in figure 3.11 (left). In figure 3.11 (right), the number of chemicals that are processed at the beginning of the chemical stage at 1 ps are shown in dependence of N for the phsp and the TsIRTInterTrack method including their percentage differences. Noticeably, using the phsp method the number of chemical species at 1 ps is on average 1.13(4) % higher than for the TsIRTInterTrack. Since systematic differences in the physical stage can be excluded, but the number of chemicals processed at the beginning of the chemical stage is different, the pre-chemical stage, the conjunction of those to analyzed stages, seems to be influenced and handled differently by the two methods. However, due to the lack of reference data, it cannot be estimated which of the two methods is more accurate in simulating the pre-chemical stage. In conclusion, the phsp and TsIRTInterTrack method result in comparable G-values simulating inter-track interactions in TOPAS-nBio, whereas differences depend on the molecule type with a maximum observed difference between the methods of 3.9% at 1 μ s.

3.3.2 Contributions

L. Derksen prepared the manuscript and simulated and compared G-values using both methods to enable inter-track interactions in TOPAS-nBio.

S. Adeberg substantively revised this manuscript and was supervising the work.

K. Zink helped to discuss and interpreting the data and substantively revised this manuscript.

K.-S. Baumann supervised the work and supported the design of the study. He helped in interpreting the results and discussing the origin of the differences between both methods.

CHAPTER 4

Discussion

Detailed studies of the interactions of radiation with matter on nano- and micrometer scales and down to kinetic energies of a few eV were investigated using a step-by-step approach in TOPAS-nBio. The investigations were carried out according to the time sequence of the interaction of radiation. Based on this, first physical and then chemical processes were examined.

4.1 Simulation of the physical stage

The physical investigations demonstrated the importance of choosing consciously the applied physics list, as the number of electron processes can be influenced and significantly differ between different applied models. The reason for this varying number of electron processes is that for each applied physics list option, different models are used for each electron process resulting in different cross-section tables, and consequently different probabilities for the processes to occur. Additionally, the frequency of processes can be affected by the application of different tracking cuts (option 2: 7.4 eV, option 4: 10 eV, option 6: 11 eV (Incerti et al., 2018)), defining the energies above which an electron is no longer simulated due to the negligible consideration of further processes¹. Furthermore, option 2 incorporates two additional processes (vibrational excitation and dissociative attachment) compared to the other two methods, which may have an impact on the overall distribution of the processes.

Even though Incerti et al. (2018) examined an improved alignment of calculated key quantities for options 4 and option 6 in comparison to experimental data (option 6 aligns better with experimental stopping powers, while option 4 exhibits better agreement with experimental w-values than the default option 2), option 2 remains the recommended physics list. The lack of data on liquid water for energies < 1 keV and experimental uncertainties reaching up to 40% com-

¹While the corresponding article did not address the varying tracking cuts, new insights and perspectives on the issue have emerged since its release. Thus, this thesis presents these novel findings to contribute to a more comprehensive understanding of the subject.

plicates providing a definitive recommendation for any physics list option (Incerti et al., 2018; Bernal et al., 2015; Michaud et al., 2003). Therefore, option 2 provides the advantage of enabling simulations up to 1 MeV and incorporating sub-excitation levels of electrons. Meanwhile, new options are developed, such as option4rel, an extended and improved version of option 4, which allows simulations up to 1 MeV, and should be taken into consideration for further simulations (Kyriakou et al., 2022). However, currently, this option is not yet implemented in TOPAS-nBio. In conclusion, one should keep in mind the potential impact of different models for inelastic physical processes which may also have an impact on the following pre-chemical stage since inelastic processes deposit energy in surrounding molecules including the DNA and generate radicals through water radiolysis. Hence, the simulation of direct and indirect DNA damages could also be impacted.

In subsequent investigations, correlations among the frequency of individual processes, deposited energy and particle range were examined as functions of the initial energy. The ionization process has been found to be crucial for the fate of a particle. This process leads to the highest energy depositions, resulting in a decrease in the particle's remaining kinetic energy and thereby its range. Indeed, the observed maximum energy depositions for ionizations, electronic and vibrational excitation correspond to energy thresholds for an ionization at the valence shells, the five excitation levels, and nine excitation phonon modes for vibrational excitations which incorporates the fine structure of the water molecule. The respectively required energy values are listed in table 4.1. For ionization, the K shell is also included in the ionization model by Dingfelder et al. (1998) included in the physics list option 2, but was not observed in our simulations since the primary electron energy was smaller than the energy threshold required for an ionization at the K shell ($E_K^{\text{ion}} = 539 \text{ eV}$). Analyzing the consecutive steps of a particle aids in comprehending individual outcomes and the impact of particles with these low initial energies. In conclusion, our study underscores the highly diverse trajectories of individual particles examined on nanodosimetric scales, whereas the interactions without any energy loss are observed the most. This serves a basis for examining the spatial distribution and dynamics of chemicals in the subsequent stage.

4.2 Simulation of the chemical stage

After investigating the physical stage of ionizing radiation on a micrometer level, the chemical stage was analyzed, with a particular focus on the influence of inter-track interactions. The analysis revealed that chemical dynamics are significantly impacted by inter-track interactions for

Table 4.1: Deposited energies in eV by vibrational excitation, electronic excitation and ionization obtained in our simulations using the physics list G4EmDNAPhysics_option2. These energies correspond to the energy thresholds of the associated processes (E_T^{vib} for vibrational excitation, E_T^{ex} for excitation, E_T^{ion} for ionization) implemented in the different models. The vibrational modes are included in the Sanche excitation model described in the study of Michaud and Sanche (1987). The energy thresholds for electronic excitation are taken from the Emfietzoglou dielectric model (Emfietzoglou and Moscovitch, 2002) and ionization levels are described by Dingfelder et al. (1998). Table taken from (Derksen et al., 2021). © Institute of Physics and Engineering in Medicine.

vib. mode	E_T^{vib}	electr. excitation level	E_T^{ex}	molecular orbital	E_T^{ion}
$2(\nu_{1,3})$	0.835	A^1B^1	8.22	$1b_1$	10.79
ν_T''	0.024	b^1a^1	10.00	$3a_1$	13.39
ν_L'	0.061	Ryd A + B	11.24	$1b_2$	16.05
ν_L''	0.092	Ryd C + D	12.61	$2a_1$	32.29
ν_2	0.204	Diffuse Bands	13.77		
$\nu_{1,3}$	0.417				
ν_3	0.46				
$\nu_{1,3} + \nu_L$	0.5				
ν_T'	0.01				

both, electron and proton sources. As the number of inter-track interactions increased, the total G-value decreased for all investigated sources. However, the influence of inter-track interactions also varied depending on the molecule type due to different reaction rates and diffusion constants of the radicals. Similar trends were observed in simulations conducted by Kreipl et al. (2009), Lai et al. (2021) and Ramos-Méndez et al. (2021), in which the effects of inter-track interactions on the G-value were investigated. Interactions for $N = 1$ and $N = 2$ primary particle tracks were examined by Kreipl et al. (2009), using the Monte Carlo track structure code PARTRAC, while Lai et al. (2021), using the Monte Carlo code gMicroMC, and Ramos-Méndez et al. (2021), using TOPAS-nBio 2.0, varied the dose rates by altering the pulse width. In all cases, the smallest pulse width resulted in the maximum impact of inter-track interactions as a result of an increased number of those chemical reactions. Across all these studies investigating radiation sources of different LETs, growing inter-track interactions were associated with a decrease of $\bullet\text{OH}$ radicals and an increase of H_2O_2 . Comparing the quantity of all G-values in the studies, it is in alignment with the general LET dependence of the G-value (Burns and Sims, 1981). Similar to

an increasing LET, with increasing inter-track interactions, $\bullet\text{OH}$ decreases, and H_2O_2 increases. Considering the higher chemical density associated with either a higher LET or with the increased number of primary tracks generating inter-track interactions, these observations appear to be in agreement with each other.

In order to compare the developed method (phsp) for generating inter-track interactions in TOPAS-nBio presented in **article 2**, a comparison study with an independently developed method in TOPAS-nBio (TsIRTInterTrack) was conducted in **article 3**. It was demonstrated that both methods, phsp and TsIRTInterTrack, exhibited the same development of the G-values with respect to inter-track interactions. Differences in the G-value between the methods, however, depended on the molecule type, with a maximum difference of 3.9% observed at the end of the chemical simulation at 1 μs . Albeit, at the beginning of the chemical stage, substantial differences between the methods were observed. Influences at the physical stage have been excluded as a contributing factor to the observed difference at 1 ps. Therefore, it is suspected that the pre-chemical stage, situated between the physical and chemical stages, is treated differently by the two methods. In the pre-chemical stage, the dissociation pathways of ionized or excited water molecules are simulated, generating radicals that are further processed in the chemical stage. However, both models apply the same dissociation schemes, including identical probabilities for each pathway. Beside the generation of radicals, in the pre-chemical stage, chemical reactions can already occur. In **article 2**, it has been shown that the number of chemical reactions in the pre-chemical stage increased with an increasing number of inter-track interactions applying the phsp method (see figure C2 in **article 2**). However, analyzing the pre-chemical stage in TOPAS-nBio, especially the influence of the TsIRTInterTrack method on this stage, presents considerable challenges. It is recommended to identify and minimize methodological differences at the pre-chemical stage in future studies, especially for research projects focusing on the pre-chemical stage or early chemical times. In any case, both methods appeared suitable for analyzing the impact of inter-track interactions as the observed differences remain in the same order of magnitude or even smaller than those currently encountered when comparing simulated and experimental yields of radicals resulting from radiolysis (e.g. up to 7% for $\bullet\text{OH}$) (Ramos-Méndez et al., 2018). Despite the quantitative differences in the calculated G-values, there are operational differences between the methods. TsIRTInterTrack requires more simulation runs for accurate results. In contrast, with the phsp method adequate statistical results can be achieved in a single run but requires two separate simulations for generating inter-track interactions, one for scoring the phase space file and one for calculating G-values. The TsIRTInterTrack method offers the advantage of

enabling inter-track interactions in a single simulation without high programming effort. However, the method has the drawback that G-values are not provided directly, but must be calculated following the simulation since the number of molecules provided with the scorer are not normalized to 100 eV of deposited energy. Although G-values are obtained directly with the phsp method, programming effort is also required, particularly in the generation of inter-track interactions. While the TsIRTIntertrack method relies solely on the IRT approach, the phsp method can be utilized with both the SBS and IRT approaches.

In summary, both methods seem suitable for simulating inter-track interactions. The choice of the method for simulating inter-track interactions depends on trade-offs related to simulation setup and post-processing requirements.

4.3 The potential role of radiochemistry in the FLASH effect

Studying inter-track interactions served as a first principle approach to investigate fundamental influences occurring at the chemical stage of irradiation with different dose rates that could potentially contribute to the FLASH effect. These studies primarily focus on the theoretical impact of inter-track interactions, which may not always align with the real-world conditions experienced during irradiation of living cells and animal tissues with FLASH dose rates. Therefore, it is essential to identify these limitations and work towards their refinement in future research.

Primarily, a major limitation of this method for simulating inter-track interactions is the temporal dimension. Here, inter-track interactions occur from primary tracks that are initiated simultaneously and not from those that are temporally distributed within a pulse, which is, however, the case when irradiating at different, realistic dose rates. Nevertheless, simulating primary tracks simultaneously maximizes the effect of inter-track interactions and without other factors such as dose per pulse and pulse width, which detailed setting parameters are not yet fully understood in terms of achieving a FLASH effect, influencing the results.

Another restriction of the simulations is that the entire geometry is composed exclusively of pure water. Thus, all radicals generated through radiolysis primarily react with each other and the surrounding water molecules. However, the chemical mechanisms differ in the presence of living cells which can act as scavenger, influencing the dynamics of the chemical stage. It is assumed that those reactions with the biological system occur within 1 ns (Wardman, 2022), but since inter-track-interactions are present already at earlier time stages, their potential influence cannot be dismissed. Nevertheless, future research studies should include scavengers, in particu-

lar dissolved oxygen, which are becoming more accessible in GEANT4, enabling simulations to be conducted under progressively more realistic conditions. For example, Ramos-Méndez et al. (2021) showed that including scavengers in the chemical simulations improved the agreement of simulated G-values to experimental data.

Comparing experimental and simulated data, G-values for $\bullet\text{OH}$ exhibit consistent dependencies on dose rate, respectively the number of tracks with inter-track interactions between the simulations presented in **article 2** and experiments conducted by Kusumoto et al. (2020). In both cases, a notable reduction in the G-value of $\bullet\text{OH}$ is evident as the dose rate increases. In contrast to experimental studies (Montay-Gruel et al., 2019; Blain et al., 2022), which have shown lower levels of H_2O_2 at FLASH dose rates compared to conventional ones, the simulations presented here regarding inter-track interactions prove an increase or at least a stable amount of H_2O_2 , which is also observed in other simulation studies conducted by Lai et al. (2021) and Kreipl et al. (2009). This discrepancy may, on the one hand, underline that the absence of scavengers and the complexity of biological tissue can lead to other observations between experiment and simulations highlighting the need for improvements in modelling chemical processes. On the other hand, the difference may also occur since experimental studies can not always be conducted with absolute precision. Particular uncertainties in experiments arise from the preparation of the samples and the experimental timeline, considering the time-dependent dynamics of chemical reactions.

Furthermore, translating the results of inter-track interactions from this study to realistic dose rates presents a challenge due to the simulations performed on micrometer scales since the dose, and hence the dose rate, are macroscopic, dosimetric quantities that cannot be calculated on microscopic scales. To illustrate this issue, Abolfath et al. (2020) conducted an exemplary dose calculation considering first the calculated dose within a single nanometer-scaled box, and second filling a centimeter-scaled box with those nanometer-scaled boxes. Even though the dose calculation of the nanometer-scaled box resulted in an extremely high dose, Abolfath et al. (2020) discussed that this dose is not representative for the centimeter-scaled box. The substantial heterogeneity in the distribution of energy depositions across the nanometer-scaled boxes would result in a considerably lower average dose for the centimeter-scaled box since in a multitude of nanometer-scaled boxes no energy would be transferred at all. With this he emphasized the complexity of scaling up nanodosimetric simulations to macroscopic quantities.

An additional limitation of the simulation of inter-track interactions in relation to the question of the origin of the FLASH effect is the unresolved issue of the differing biological responses observed in normal and tumor tissues.

However, it is worth noting that inter-track interactions, impacting the chemical dynamics, may take place at ultra-high dose rates due to the temporal structure, and they could be one of many factors contributing to the FLASH effect. As articulated by Rothwell et al. (2021), the FLASH effect is indeed the result of a complex interplay of multiple parameters underscoring the significance of considering the impact of inter-track interactions in the context of the FLASH effect.

4.4 Applicability and limitations of the Monte Carlo toolkit TOPAS-nBio for nanodosimetric simulations

The simulations presented in all three articles demonstrated the versatility and feasibility of TOPAS-nBio as an application for Monte Carlo simulations on nanodosimetric scales. The tool exhibits great extensibility, allowing for extending the simulations with customized features at both the physical and chemical levels. In all studies conducted during this thesis, explicit scorers or specific procedures were not always available in this Monte Carlo tool. However, it was possible to extend and customized the code to meet the specific objectives of this research. For instance, the investigation of inter-track interactions became feasible, even though it was not initially supported in TOPAS-nBio 1.0. Consequently, TOPAS-nBio maintains the wide range of capabilities inherent in GEANT4 simulations making it a feasible tool for examining biological effects on small scales.

However, due to the step-by-step approach of the TS simulation, simulation times can be very high (weeks to months), especially if a high amount of chemical species is processed in the chemical stage. There are already approaches like the IRT method (Green et al., 1990; Schuemann et al., 2019; Ramos-Méndez et al., 2020) for accelerating the simulating the chemical stage, but more variance reduction techniques still need to be developed. Finding the right balance between an extremely precise and realistic simulation setup and one that can be simulated within reasonable time frames is a task that users need to determine for their individual simulations and research questions. This process often requires a substantial level of experience with the tool.

However, the tool gets updated frequently progressively enhancing physical and chemical models, models of geometries like cells and nuclei, and extending it with biological repair pathways (McMahon et al., 2016; Warmenhoven et al., 2020) while reducing computation times.

CHAPTER 5

Conclusions and outlook

In the context of this dissertation, physical and chemical interactions of ionizing radiation at micrometer scale were examined using the Monte Carlo toolkit TOPAS-nBio. The findings provide a base for validating simulations against corresponding experiments required for further exploring the biological effects, the subsequent stage of radiation effects, of proton irradiation. This, in turn, facilitates the optimization of the RBE of protons.

On the physical stage, the study highlighted the significance of validating simulations against experiments, particularly at low energies, where different models for electron processes included in TOPAS-nBio may yield divergent results. Furthermore, the unique development of each individual particle track on microscopic scales was demonstrated, which is particularly influenced by the process and deposited energies per step.

The dynamics of chemicals in TOPAS-nBio was analyzed with a focus on inter-track interactions with regard to the FLASH effect. A method was developed to enable the simulation of N particle tracks simultaneously, facilitating inter-track interactions of chemical species in TOPAS-nBio. With increasing N , which imitates higher dose rates, the total yield of chemicals at the end of the chemical simulation decreased. This is attributed to the elevated initial density of chemicals, resulting in an increase of chemical reactions. Consequently, with regard to the FLASH effect, a reduced number of radicals induced through inter-track interactions could reduce the number of indirect DNA damages. However, inter-track interactions alone do not account for the FLASH effect, and it remains challenging to discern the differences between normal and tumor tissues.

The established method for simulating inter-track interactions in TOPAS-nBio has been compared to an independently developed method enabling inter-track interactions. The simulation results were compared by calculating the G-values of various chemicals in dependence on the number N of tracks with inter-track interactions. For individual molecule types, differences up to 3.9% at the end of the chemical stage were identified, whereas differences were the highest at the beginning of the chemical stage. Overall, both methods showed the same qualitative dependence

on the number of inter-track interactions, making them both suitable approaches to investigate inter-track interactions.

All in all, TOPAS-nBio has proven to be a reliable and feasible tool to simulate physical interactions on small scales as well as chemical processes. However, experimental data on those scales are very limited, so that more studies need to be conducted to validate the simulation result and optimize their settings, ensuring the development of a reliable simulation tool.

In order to continue this essential research, the findings of this dissertation successfully secured additional financial support from two foundations¹. Experiments have already been conducted with the intention of validating the chemical stage of the simulations. Therefore, chemical dosimeters, including the Amplex®Red assay (Thermo Fisher Scientific Inc, 2023) and a Fricke solution (Fricke, H. and S. Morse, 1929; Fricke and Morse, 1927), were used. The AmplexRed assay can be used to measure the production of H₂O₂ through a chemical reaction of the solution, resulting in a fluorescent product. The Fricke dosimeter consists of an aqueous sulfuric acid solution containing ferrous ions (Fe²⁺) which undergo irreversible oxidation to ferric ions (Fe³⁺) upon irradiation, involving the radiolysis products •OH, H₂O₂ and HO₂•. This oxidation results in a change in the optical density of the solution in the UV range, spectrometrically measurable. In TOPAS-nBio, all chemicals and reactions are included involved in the oxidation of Fe²⁺ to Fe³⁺ ions after irradiation, enabling the simulation of the yield of Fe³⁺ ions. To optimize experimental setups and conditions for validating the chemical stage in the simulations, both experimental methods were examined and investigated for dependencies and external influences such as light exposure, temperature, oxygen, dose rate. After examining the chemical dosimeters, the radiochemistry in the simulations will be validated. To enhance alignment with experiments, adjustments may involve modelling extra chemical molecules and scavengers, expanding the list of chemical reactions, and optimizing reaction rates and diffusion constants.

Moreover, to experimentally assess the impact of ultra-high dose rates and compare results with simulated radical yields from inter-track interactions, the application of FLASH dose rates at the Marburg Ion-Beam Therapy Center (MIT) is currently under development. Preliminary measurements, presented at the FLASH Radiotherapy and Particle Therapy (FRPT) conference 2023, showed that dose rates up to 172 Gy/s (applying around 17.2 Gy in 100 ms with an 81 MeV proton pencil beam) can be achieved.

After validating the chemical stage, the validation of simulated DNA damage yields and the re-

¹Provided by the *Bundesministerium für Bildung und Forschung* and by a research promotion program of the state of Hesse, Germany, named *Landes-Offensive zur Entwicklung Wissenschaftlich-ökonomischer Exzellenz*.

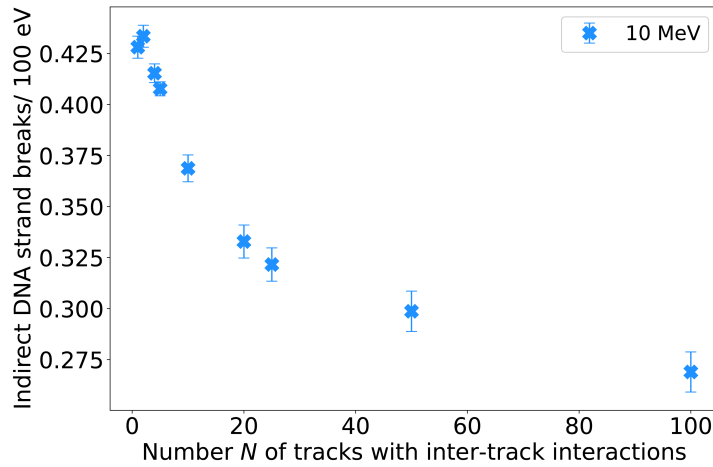


Figure 5.1: Total number of indirect DNA strand breaks normalized to 100 eV of deposited energy in dependence of the number N of tracks with inter-track interactions using a 10 MeV proton beam. Standard deviations ($k = 1$) are represented by vertical error bars.

pair processes becomes essential. Here, it is crucial to utilize accurate DNA and nucleus models in TOPAS-nBio, adjust parameters such as the probability of direct and indirect DNA damage, and enhance simulations for tissue-equivalent conditions. For the experimental validation, cell lines will be irradiated to determine cellular survival and the amount of DNA damage, especially the amount of DSBs. These strand breaks will be quantified by immunohistochemical staining using the γ -H2AX/53BP1 foci technique (Popp et al., 2017).

First simulations, translating the influence of the reduce radical yields with increasing number of inter-track interactions to the yield of DNA damages, have already been performed and presented during the FRPT 2022. Figure 5.1 shows indirect DNA strand breaks in dependence on the number N of tracks with inter-track interactions of a 10 MeV proton beam. In this case, indirect strand breaks are detected if $\bullet\text{OH}$ radicals interact with the DNA backbone. The number of indirect strand breaks decreases with increasing N which is in alignment with the decreasing G-value of $\bullet\text{OH}$.

Once the nanodosimetric Monte Carlo simulations are thoroughly validated, the simulations can be integrated into experiments that explore the impact of protons on a biological level and assist in interpreting the biological effects of proton irradiation. Thus, the refinement of RBE models becomes imperative to enhance the overall prediction of patient outcomes in proton therapy. This involves incorporating RBE models into treatment planning, ultimately reducing complications in normal tissue and optimizing the overall treatment results for proton therapy patients.

Bibliography

- Abolfath, R., D. Grosshans, and R. Mohan, 2020: Oxygen depletion in FLASH ultra-high-dose-rate radiotherapy: a molecular dynamics simulation. *Medical physics*, **47** (12), 6551–6561.
- Adler Jr, J. R., S. D. Chang, M. J. Murphy, J. Doty, P. Geis, and S. L. Hancock, 1997: The Cyberknife: a frameless robotic system for radiosurgery. *Stereotactic and functional neurosurgery*, **69** (1-4), 124–128.
- Agostinelli, S., J. Allison, K. a. Amako, J. Apostolakis, H. Araujo, P. Arce, M. Asai, D. Axen, S. Banerjee, G. Barrand, et al., 2003: GEANT4 - a simulation toolkit. *Nucl. Instrum. Methods Phys. Res. A*, **506**, 250–303.
- Allen, A. O., 1961: The radiation chemistry of water and aqueous solutions.
- Allison, J., K. Amako, J. Apostolakis, H. Araujo, P. A. Dubois, M. Asai, G. Barrand, R. Capra, S. Chauvie, R. Chytrcek, et al., 2006: Geant4 developments and applications. *IEEE Transactions on nuclear science*, **53** (1), 270–278.
- Autsavapromporn, N., J. Meesungnoen, I. Plante, and J.-P. Jay-Gerin, 2007: Monte Carlo simulation study of the effects of acidity and LET on the primary free-radical and molecular yields of water radiolysis — Application to the Fricke dosimeter. *Canadian journal of chemistry*, **85** (3), 214–229.
- Baack, L., C. Schuy, S. Brons, F. Horst, B. Voss, K. Zink, T. Haberer, M. Durante, and U. Weber, 2022: Reduction of recombination effects in large plane parallel beam monitors for FLASH radiotherapy with scanned ion beams. *Physica Medica*, **104**, 136–144.
- Bahn, E., J. Bauer, S. Harrabi, K. Herfarth, J. Debus, and M. Alber, 2020: Late Contrast Enhancing Brain Lesions in Proton-Treated Patients With Low-Grade Glioma: Clinical Evidence for Increased Periventricular Sensitivity and Variable RBE. *International Journal of Radiation Oncology*Biography*Physics*, **107** (3), 571–578.

- Belli, M., D. Bettega, P. Calzolari, F. Cera, R. Cherubini, M. D. Vecchia, M. Durante, S. Favaretto, G. Gialanella, and G. Grossi, 2000: Inactivation of human normal and tumour cells irradiated with low energy protons. *International journal of radiation biology*, **76** (6), 831–839.
- Belli, M., A. Campa, and I. Ermolli, 1997: A semi-empirical approach to the evaluation of the relative biological effectiveness of therapeutic proton beams: the methodological framework. *Radiation research*, **148** 6, 592–8.
- Belli, M., F. Cera, R. Cherubini, F. Ianzini, G. Moschini, O. Sapor, G. Simone, M. Tabocchini, and P. Tiveron, 1994: Dna double-strand breaks induced by low energy protons in v79 cells. *International Journal of Radiation Biology*, **65** (5), 529–536.
- Bentzen, S. M., L. S. Constine, J. O. Deasy, A. Eisbruch, A. Jackson, L. B. Marks, R. K. Ten Haken, and E. D. Yorke, 2010: Quantitative Analyses of Normal Tissue Effects in the Clinic (QUANTEC): an introduction to the scientific issues. *International Journal of Radiation Oncology* Biology* Physics*, **76** (3), S3–S9.
- Bernal, M. A., M. C. Bordage, J. M. C. Brown, M. Davídková, E. Delage, Z. El Bitar, S. A. Enger, Z. Francis, S. Guatelli, V. N. Ivanchenko, et al., 2015: Track structure modeling in liquid water: A review of the Geant4-DNA very low energy extension of the Geant4 Monte Carlo simulation toolkit. *Physica Medica*, **31** (8), 861–874.
- Bethe, H., 1930: Zur Theorie des Durchgangs schneller Korpuskularstrahlen durch Materie. *Annalen der Physik*, **397** (3), 325–400.
- Blain, G., J. Vandenborre, D. Villoing, V. Fiegel, G. R. Fois, F. Haddad, C. Koumeir, L. Maigne, V. Métivier, F. Poirier, et al., 2022: Proton Irradiations at Ultra-High Dose Rate vs. Conventional Dose Rate: Strong Impact on Hydrogen Peroxide Yield. *Radiation Research*.
- Bloch, F., 1933: Zur Bremsung rasch bewegter Teilchen beim Durchgang durch Materie. *Annalen der Physik*, **408** (3), 285–320.
- Bordage, M., J. Bordes, S. Edel, M. Terrissol, X. Franceries, M. Bardiès, N. Lampe, and S. Incerti, 2016: Implementation of new physics models for low energy electrons in liquid water in Geant4-DNA. *Physica Medica*, **32** (12), 1833 – 1840.
- Borras, J. M., Y. Lievens, P. Dunscombe, M. Coffey, J. Malicki, J. Corral, C. Gasparotto, N. De-fourny, M. Barton, R. Verhoeven, et al., 2015: The optimal utilization proportion of external

- beam radiotherapy in European countries: an ESTRO-HERO analysis. *Radiotherapy and Oncology*, **116** (1), 38–44.
- Boscolo, D., E. Scifoni, M. Durante, M. Krämer, and M. C. Fuss, 2021: May oxygen depletion explain the FLASH effect? A chemical track structure analysis. *Radiotherapy and Oncology*, **162**, 68–75.
- Buonanno, M., V. Grilj, and D. J. Brenner, 2019: Biological effects in normal cells exposed to FLASH dose rate protons. *Radiotherapy and Oncology*, **139**, 51–55.
- Burns, W. G. and H. E. Sims, 1981: Effect of radiation type in water radiolysis. *Journal of the Chemical Society, Faraday Transactions 1: Physical Chemistry in Condensed Phases*, **77** (11), 2803–2813.
- Buxton, G., 1987: Radiation chemistry of the liquid state. *Radiation chemistry*.
- Chandra, R. A., F. K. Keane, F. E. Voncken, and C. R. Thomas, 2021: Contemporary radiotherapy: present and future. *The Lancet*, **398** (10295), 171–184.
- Chen, Y. and S. Ahmad, 2011: Empirical model estimation of relative biological effectiveness for proton beam therapy. *Radiation Protection Dosimetry*, **149** (2), 116–123.
- Chvetsov, A. V. and S. L. Paige, 2010: The influence of CT image noise on proton range calculation in radiotherapy planning. *Physics in Medicine & Biology*, **55** (6), N141.
- ClinicalTrials.gov, 2023: Irradiation of Melanoma in a Pulse (IMPulse). URL <https://clinicaltrials.gov/study/NCT04986696>.
- Daugherty, E. C., A. Mascia, Y. Zhang, E. Lee, Z. Xiao, M. Sertorio, J. Woo, C. McCann, K. Russell, L. Levine, et al., 2023: FLASH radiotherapy for the treatment of symptomatic bone metastases (FAST-01): protocol for the first prospective feasibility study. *JMIR Research Protocols*, **12** (1), e41 812.
- Denifl, S., T. Märk, and P. Scheier, 2012: *The Role of Secondary Electrons in Radiation Damage*, 45–58. Springer Netherlands, Dordrecht.
- Derksen, L., S. Adeberg, K. Zink, and K.-S. Baumann, 2024: Comparison of two methods simulating inter-track interactions using the radiobiological Monte Carlo toolkit TOPAS-nBio. *Physics in Medicine & Biology*.

- Derksen, L., V. Flatten, R. Engenhart-Cabillic, K. Zink, and K.-S. Baumann, 2023: A method to implement inter-track interactions in Monte Carlo simulations with TOPAS-nBio and their influence on simulated radical yields following water radiolysis. *Physics in Medicine and Biology*, **68** (13), 135 017.
- Derksen, L., T. Pfuhl, R. Engenhart-Cabillic, K. Zink, and K.-S. Baumann, 2021: Investigating the feasibility of TOPAS-nBio for Monte Carlo track structure simulations by adapting GEANT4-DNA examples application. *Physics in Medicine & Biology*, **66** (17), 175 023.
- Dingfelder, M., D. Hantke, M. Inokuti, and H. G. Paretzke, 1998: Electron inelastic-scattering cross sections in liquid water. *Radiation Physics and Chemistry*, **53** (1), 1–18.
- Draganic, I., 2012: *The radiation chemistry of water*, Vol. 26. Elsevier.
- Draganic, Z. and I. Draganic, 1971: Formation of primary yields of hydrogen peroxide and molecular hydrogen (GH₂O₂ and GH₂) in the. gamma. radiolysis of neutral aqueous solutions. *The Journal of Physical Chemistry*, **75** (26), 3950–3957.
- Emami, B., J. Lyman, A. Brown, L. Cola, M. Goitein, J. Munzenrider, B. Shank, L. Solin, and M. Wesson, 1991: Tolerance of normal tissue to therapeutic irradiation. *International Journal of Radiation Oncology* Biology* Physics*, **21** (1), 109–122.
- Emfietzoglou, D. and M. Moscovitch, 2002: Inelastic collision characteristics of electrons in liquid water. *Nuclear Instruments and Methods in Physics Research Section B: Beam Interactions with Materials and Atoms*, **193** (1), 71 – 78.
- España, S. and H. Paganetti, 2011: Uncertainties in planned dose due to the limited voxel size of the planning CT when treating lung tumors with proton therapy. *Physics in Medicine & Biology*, **56** (13), 3843.
- Faddegon, B., J. Ramos-Méndez, J. Schuemann, A. McNamara, J. Shin, J. Perl, and H. Paganetti, 2020: The TOPAS tool for particle simulation, a Monte Carlo simulation tool for physics, biology and clinical research. *Physica Medica*, **72**, 114–121.
- Favaudon, V., L. Caplier, V. Monceau, F. Pouzoulet, M. Sayarath, C. Fouillade, M.-F. Poupon, I. Brito, P. Hupé, J. Bourhis, et al., 2014: Ultrahigh dose-rate FLASH irradiation increases the differential response between normal and tumor tissue in mice. *Science translational medicine*, **6** (245), 245ra93–245ra93.

- Fouillade, C., S. Curras-Alonso, L. Giuranno, E. Quelennec, S. Heinrich, S. Bonnet-Boissinot, A. Beddok, S. Leboucher, H. U. Karakurt, M. Bohec, et al., 2020: FLASH irradiation spares lung progenitor cells and limits the incidence of radio-induced senescence. *Clinical Cancer Research*, **26 (6)**, 1497–1506.
- Fowler, J. F., 1989: The linear-quadratic formula and progress in fractionated radiotherapy. *The British journal of radiology*, **62 (740)**, 679–694.
- Fricke, H. and S. Morse, 1927: The chemical action of roentgen rays on dilute ferrosulphate solutions as a measure of dose. *Am. J. Roentgenol. Radium Therapy Nucl. Med.*, **18**, 430–432.
- Fricke, H. and S. Morse, 1929: XIII. The action of X-rays on ferrous sulphate solutions. *The London, Edinburgh, and Dublin Philosophical Magazine and Journal of Science*, **7 (41)**, 129–141.
- Froidevaux, P., V. Grilj, C. Bailat, W. R. Geyer, F. Bochud, and M.-C. Vozenin, 2023: FLASH irradiation does not induce lipid peroxidation in lipids micelles and liposomes. *Radiation Physics and Chemistry*, **205**, 110733.
- Fuss, M., K. Poljanc, D. W. Miller, J. O. Archambeau, J. M. Slater, J. D. Slater, and E. B. Hug, 2000: Normal tissue complication probability (NTCP) calculations as a means to compare proton and photon plans and evaluation of clinical appropriateness of calculated values. *International journal of cancer*, **90 (6)**, 351–358.
- Gao, Y., R. Liu, C.-W. Chang, S. Charyyev, J. Zhou, J. D. Bradley, T. Liu, and X. Yang, 2022: A potential revolution in cancer treatment: A topical review of FLASH radiotherapy. *Journal of Applied Clinical Medical Physics*, e13790.
- Giantsoudi, D., R. V. Sethi, B. Y. Yeap, B. R. Eaton, D. H. Ebb, P. A. Caruso, O. Rapalino, Y.-L. E. Chen, J. A. Adams, T. I. Yock, et al., 2016: Incidence of CNS injury for a cohort of 111 patients treated with proton therapy for medulloblastoma: LET and RBE associations for areas of injury. *International Journal of Radiation Oncology* Biology* Physics*, **95 (1)**, 287–296.
- Gómez, F., D. M. Gonzalez-Castaño, N. G. Fernández, J. Pardo-Montero, A. Schüller, A. Gasparini, V. Vanreusel, D. Verellen, G. Felici, R. Kranzer, et al., 2022: Development of an ultra-thin parallel plate ionization chamber for dosimetry in FLASH radiotherapy. *Medical Physics*, **49 (7)**, 4705–4714.

- Goodhead, D. T., 1994: Initial events in the cellular effects of ionizing radiations: clustered damage in DNA. *International journal of radiation biology*, **65** (1), 7–17.
- Green, L., D. Murray, D. Tran, A. Bant, G. Kazarians, M. Moyers, and G. Nelson, 2001: Response of thyroid follicular cells to gamma irradiation compared to proton irradiation. I. Initial characterization of DNA damage, micronucleus formation, apoptosis, cell survival, and cell cycle phase redistribution. *Radiation research*, **155** (1), 32–42.
- Green, N., M. Pilling, S. Pimblott, and P. Clifford, 1990: Stochastic modeling of fast kinetics in a radiation track. *Journal of Physical Chemistry*, **94** (1), 251–258.
- Grimes, D. R. and M. Partridge, 2015: A mechanistic investigation of the oxygen fixation hypothesis and oxygen enhancement ratio. *Biomedical physics & engineering express*, **1** (4), 045 209.
- Group, I. M. R. T. C. W. et al., 2001: Intensity-modulated radiotherapy: current status and issues of interest. *International Journal of Radiation Oncology* Biology* Physics*, **51** (4), 880–914.
- Grün, R., T. Friedrich, M. Krämer, K. Zink, M. Durante, R. Engenhart-Cabillic, and M. Scholz, 2013: Physical and biological factors determining the effective proton range. *Medical physics*, **40** (11), 111 716.
- Hiroki, A., S. M. Pimblott, and J. A. LaVerne, 2002: Hydrogen peroxide production in the radiolysis of water with high radical scavenger concentrations. *The Journal of Physical Chemistry A*, **106** (40), 9352–9358.
- Holliday, E. B., A. S. Garden, D. I. Rosenthal, C. D. Fuller, W. H. Morrison, G. B. Gunn, J. Phan, B. M. Beadle, X. R. Zhu, X. Zhang, et al., 2015: Proton therapy reduces treatment-related toxicities for patients with nasopharyngeal cancer: a case-match control study of intensity-modulated proton therapy and intensity-modulated photon therapy. *International Journal of Particle Therapy*, **2** (1), 19–28.
- Hornsey, S. and T. Alper, 1966: Unexpected dose-rate effect in the killing of mice by radiation. *Nature*, **210** (5032), 212–213.
- ICRU, 2007: Prescribing, recording, and reporting proton-beam therapy. ICRU Report No. 78 (Bethesda, MD: ICRU).

- Incerti, S., G. Baldacchino, M. Bernal, R. Capra, C. Champion, Z. Francis, S. Guatelli, P. Guèye, A. Mantero, B. Mascialino, P. Moretto, P. Nieminen, A. Rosenfeld, C. Villagrasa, and C. Zacharatou, 2010a: The Geant4-DNA project The Geant4-DNA collaboration. *International Journal of Modeling, Simulation, and Scientific Computing*, **1** (2), 157.
- Incerti, S., A. Ivanchenko, M. Karamitros, A. Mantero, P. Moretto, H. N. Tran, B. Mascialino, C. Champion, V. N. Ivanchenko, M. A. Bernal, Z. Francis, C. Villagrasa, G. Baldacchino, P. Gùye, R. Capra, P. Nieminen, and C. Zacharatou, 2010b: Comparison of GEANT4 very low energy cross section models with experimental data in water. *Medical Physics*, **37** (9), 4692–4708.
- Incerti, S., I. Kyriakou, M. Bernal, M. Bordage, Z. Francis, S. Guatelli, V. Ivanchenko, M. karamitros, N. Lampe, S. Lee, S. Meylan, C. Min, W. Shin, P. Nieminen, D. Sakata, N. Tang, C. Villagrasa, H. Tran, and J. Brown, 2018: Geant4-DNA example applications for track structure simulations in liquid water: A report from the Geant4-DNA Project. *Medical Physics*, **45** (8), e722–e739.
- Indelicato, D. J., S. Flampouri, R. L. Rotondo, J. A. Bradley, C. G. Morris, P. R. Aldana, E. Sandler, and N. P. Mendenhall, 2014: Incidence and dosimetric parameters of pediatric brainstem toxicity following proton therapy. *Acta oncologica*, **53** (10), 1298–1304.
- Jackson, S. P., 2002: Sensing and repairing DNA double-strand breaks. *Carcinogenesis*, **23** (5), 687–696.
- Jansen, J., J. Knoll, E. Beyreuther, J. Pawelke, R. Skuza, R. Hanley, S. Brons, F. Pagliari, and J. Seco, 2021: Does FLASH deplete oxygen? Experimental evaluation for photons, protons, and carbon ions. *Medical physics*, **48** (7), 3982–3990.
- Jenner, T., C. Delara, P. O'Neill, and D. Stevens, 1993: Induction and rejoining of dna double-strand breaks in v79-4 mammalian cells following γ - and α -irradiation. *International Journal of Radiation Biology*, **64** (3), 265–273.
- Jones, B., 2015: Towards achieving the full clinical potential of proton therapy by inclusion of LET and RBE models. *Cancers*, **7** (1), 460–480.
- Karamitros, M., S. Luan, M. A. Bernal, J. Allison, G. Baldacchino, M. Davidkova, Z. Francis, W. Friedland, V. Ivantchenko, A. Ivantchenko, et al., 2014: Diffusion-controlled reactions modeling in GEANT4-DNA. *Journal of Computational Physics*, **274**, 841–882.

- Karamitros, M., A. Mantero, S. Incerti, W. Friedland, G. Baldacchino, P. Barberet, M. Bernal, R. Capra, C. Champion, Z. El Bitar, et al., 2011: Modeling radiation chemistry in the GEANT4 toolkit. *Prog. Nucl. Sci. Technol*, **2**, 503–508.
- Kirsch, D. G. and N. J. Tarbell, 2004: New technologies in radiation therapy for pediatric brain tumors: the rationale for proton radiation therapy. *Pediatric blood & cancer*, **42** (5), 461–464.
- Kreipl, M. S., W. Friedland, and H. G. Paretzke, 2009: Interaction of ion tracks in spatial and temporal proximity. *Radiation and environmental biophysics*, **48** (4), 349–359.
- Kusumoto, T., H. Kitamura, S. Hojo, T. Konishi, and S. Kodaira, 2020: Significant changes in yields of 7-hydroxy-coumarin-3-carboxylic acid produced under FLASH radiotherapy conditions. *RSC advances*, **10** (63), 38 709–38 714.
- Kyriakou, I., D. Emfietzoglou, and S. Incerti, 2022: Status and extension of the GEANT4-DNA dielectric models for application to electron transport. *Frontiers in Physics*, **9**, 711 317.
- Kyriakou, I., S. Incerti, and Z. Francis, 2015: Technical Note: Improvements in geant4 energy-loss model and the effect on low-energy electron transport in liquid water. *Medical Physics*, **42** (7), 3870–3876.
- Labarbe, R., L. Hotoiu, J. Barbier, and V. Favaudon, 2020: A physicochemical model of reaction kinetics supports peroxy radical recombination as the main determinant of the FLASH effect. *Radiotherapy and Oncology*, **153**, 303–310.
- Lai, Y., X. Jia, and Y. Chi, 2021: Modeling the effect of oxygen on the chemical stage of water radiolysis using GPU-based microscopic Monte Carlo simulations, with an application in FLASH radiotherapy. *Physics in Medicine & Biology*, **66** (2), 025 004.
- Leszczynski, K. and S. Boyko, 1997: On the controversies surrounding the origins of radiation therapy. *Radiotherapy and oncology*, **42** (3), 213–217.
- Lieber, M. R., 2008: The mechanism of human nonhomologous DNA end joining. *Journal of Biological Chemistry*, **283** (1), 1–5.
- Limoli, C. L. and M.-C. Vozenin, 2023: Reinventing radiobiology in the light of FLASH radiotherapy. *Annual Review of Cancer Biology*, **7**, 1–21.

- Lin, L. L., S. Vennarini, A. Dimofte, D. Ravanelli, K. Shillington, S. Batra, Z. Tochner, S. Both, and G. Freedman, 2015: Proton beam versus photon beam dose to the heart and left anterior descending artery for left-sided breast cancer. *Acta Oncologica*, **54** (7), 1032–1039.
- Liu, C., J. A. Bradley, D. Zheng, R. B. M. Vega, C. J. Beltran, N. Mendenhall, and X. Liang, 2022: RBE-weighted dose and its impact on the risk of acute coronary event for breast cancer patients treated with intensity modulated proton therapy. *Journal of applied clinical medical physics*, **23** (4), e13 527.
- Lomax, M., L. Folkes, and P. O’neill, 2013: Biological consequences of radiation-induced DNA damage: relevance to radiotherapy. *Clinical oncology*, **25** (10), 578–585.
- Mairani, A., I. Dokic, G. Magro, T. Tessonier, J. Bauer, T. Böhlen, M. Ciocca, A. Ferrari, P. Sala, O. Jäkel, et al., 2017: A phenomenological relative biological effectiveness approach for proton therapy based on an improved description of the mixed radiation field. *Physics in Medicine & Biology*, **62** (4), 1378.
- Marinelli, M., G. Felici, F. Galante, A. Gasparini, L. Giuliano, S. Heinrich, M. Pacitti, G. Prestopino, V. Vanreusel, D. Verellen, et al., 2022: Design, realization, and characterization of a novel diamond detector prototype for FLASH radiotherapy dosimetry. *Medical Physics*, **49** (3), 1902–1910.
- Mascia, A. E., E. C. Daugherty, Y. Zhang, E. Lee, Z. Xiao, M. Sertorio, J. Woo, L. R. Backus, J. M. McDonald, C. McCann, et al., 2023: Proton FLASH radiotherapy for the treatment of symptomatic bone metastases: The FAST-01 nonrandomized trial. *JAMA oncology*, **9** (1), 62–69.
- McDonald, M. W., Y. Liu, M. G. Moore, and P. A. Johnstone, 2016: Acute toxicity in comprehensive head and neck radiation for nasopharynx and paranasal sinus cancers: cohort comparison of 3D conformal proton therapy and intensity modulated radiation therapy. *Radiation oncology*, **11** (1), 1–10.
- McMahon, S. J., 2021: Proton RBE models: Commonalities and differences. *Physics in Medicine & Biology*, **66** (4), 04NT02.
- McMahon, S. J., J. Schuemann, H. Paganetti, and K. M. Prise, 2016: Mechanistic modelling of DNA repair and cellular survival following radiation-induced DNA damage. *Scientific reports*, **6** (1), 1–14.

- Melton, C. E., 1972: Cross Sections and Interpretation of Dissociative Attachment Reactions Producing OH, O, and H in H₂O. *The Journal of Chemical Physics*, **57** (10), 4218–4225.
- Metropolis, N. and S. Ulam, 1949: The Monte Carlo method. *Journal of the American statistical association*, **44** (247), 335–341.
- Michaud, M. and L. Sanche, 1987: Absolute vibrational excitation cross sections for slow-electron (1–18 eV) scattering in solid H₂O. *Phys. Rev. A*, **36**, 4684–4699.
- Michaud, M., A. Wen, and L. Sanche, 2003: Cross Sections for Low-Energy (1–100 eV) Electron Elastic and Inelastic Scattering in Amorphous Ice. *Radiation Research*, **159** (1), 3–22.
- Miralbell, R., A. Lomax, and M. Russo, 1997: Potential role of proton therapy in the treatment of pediatric medulloblastoma/primitive neuro-ectodermal tumors: spinal theca irradiation. *International journal of radiation oncology, biology, physics*, **38** (4), 805–811.
- Mock, U., D. Georg, J. Bogner, T. Auberger, and R. Pötter, 2004: Treatment planning comparison of conventional, 3D conformal, and intensity-modulated photon (IMRT) and proton therapy for paranasal sinus carcinoma. *International Journal of Radiation Oncology* Biology* Physics*, **58** (1), 147–154.
- Montay-Gruel, P., M. M. Acharya, K. Petersson, L. Alikhani, C. Yakkala, B. D. Allen, J. Ollivier, B. Petit, P. G. Jorge, A. R. Syage, et al., 2019: Long-term neurocognitive benefits of FLASH radiotherapy driven by reduced reactive oxygen species. *Proceedings of the National Academy of Sciences*, **116** (22), 10943–10951.
- Munck af Rosenschold, P., S. A. Engelholm, P. N. Brodin, M. Jørgensen, D. R. Grosshans, R. X. Zhu, M. Palmer, C. N. Crawford, and A. Mahajan, 2016: A retrospective evaluation of the benefit of referring pediatric cancer patients to an external proton therapy center. *Pediatric Blood & Cancer*, **63** (2), 262–269.
- Nanda, R. H., R. G. Ganju, E. Schreibmann, Z. Chen, C. Zhang, N. Jegadeesh, R. Cassidy, C. Deng, B. R. Eaton, and N. Esiashvili, 2017: Correlation of acute and late brainstem toxicities with dose-volume data for pediatric patients with posterior fossa malignancies. *International Journal of Radiation Oncology* Biology* Physics*, **98** (2), 360–366.
- Ödén, J., K. Eriksson, and I. Toma-Dasu, 2017: Inclusion of a variable RBE into proton and photon plan comparison for various fractionation schedules in prostate radiation therapy. *Medical physics*, **44** (3), 810–822.

- Otto, K., 2008: Volumetric modulated arc therapy: IMRT in a single gantry arc. *Medical physics*, **35 (1)**, 310–317.
- Paganetti, H., 2003: Significance and implementation of RBE variations in proton beam therapy. *Technology in cancer research & treatment*, **2 (5)**, 413–426.
- Paganetti, H. and M. Goitein, 2000: Radiobiological significance of beamline dependent proton energy distributions in a spread-out bragg peak. *Medical physics*, **27 (5)**, 1119–1126.
- Paganetti, H., A. Niemierko, M. Ancukiewicz, L. E. Gerweck, M. Goitein, J. S. Loeffler, and H. D. Suit, 2002: Relative biological effectiveness (RBE) values for proton beam therapy. *International Journal of Radiation Oncology* Biology* Physics*, **53 (2)**, 407–421.
- Paganetti, Harald, 2012: Range uncertainties in proton therapy and the role of Monte Carlo simulations. *Physics in Medicine & Biology*, **57 (11)**, R99–R117.
- Paganetti, Harald, 2014: Relative biological effectiveness (RBE) values for proton beam therapy. Variations as a function of biological endpoint, dose, and linear energy transfer. *Physics in Medicine & Biology*, **59 (22)**, R419.
- Pastina, B. and J. A. LaVerne, 1999: Hydrogen peroxide production in the radiolysis of water with heavy ions. *The Journal of Physical Chemistry A*, **103 (11)**, 1592–1597.
- Peeler, C. R., D. Mirkovic, U. Titt, P. Blanchard, J. R. Gunther, A. Mahajan, R. Mohan, and D. R. Grosshans, 2016: Clinical evidence of variable proton biological effectiveness in pediatric patients treated for ependymoma. *Radiotherapy and Oncology*, **121 (3)**, 395–401.
- Perl, J., J. Shin, J. Schümann, B. Faddegon, and H. Paganetti, 2012: TOPAS: An innovative proton Monte Carlo platform for research and clinical applications. *Medical Physics*, **39 (11)**, 6818–6837.
- Pimblott, S. M. and J. A. LaVerne, 2007: Production of low-energy electrons by ionizing radiation. *Radiation Physics and Chemistry*, **76 (8-9)**, 1244–1247.
- Plante, I., 2011: A Monte-Carlo step-by-step simulation code of the non-homogeneous chemistry of the radiolysis of water and aqueous solutions—Part II: calculation of radiolytic yields under different conditions of LET, pH, and temperature. *Radiation and environmental biophysics*, **50**, 405–415.

- Popp, H. D., S. Brendel, W.-K. Hofmann, and A. Fabarius, 2017: Immunofluorescence Microscopy of γ H2AX and 53BP1 for Analyzing the Formation and Repair of DNA Double-strand Breaks. *JoVE (Journal of Visualized Experiments)*, **(129)**, e56 617.
- Potters, L., M. Steinberg, C. Rose, R. Timmerman, S. Ryu, J. M. Hevezi, J. Welsh, M. Mehta, D. A. Larson, and N. A. Janjan, 2004: American Society for Therapeutic Radiology and Oncology* and American College of Radiology Practice Guideline for the performance of stereotactic body radiation therapy. *International journal of radiation oncology, biology, physics*, **60 (4)**, 1026–1032.
- PTCOG, 2023: Particle therapy facilities in clinical operation. URL <https://ptcog.site/index.php/facilities-in-operation-public>.
- Ramos-Méndez, J., N. Domínguez-Kondo, J. Schuemann, A. McNamara, E. Moreno-Barbosa, and B. Faddegon, 2020: LET-dependent intertrack yields in proton irradiation at ultra-high dose rates relevant for FLASH therapy. *Radiation research*, **194 (4)**, 351–362.
- Ramos-Méndez, J., J. LaVerne, N. Domínguez-Kondo, J. Milligan, V. Štěpán, K. Stefanová, Y. Perrot, C. Villagrasa, W. Shin, S. Incerti, et al., 2021: TOPAS-nBio validation for simulating water radiolysis and DNA damage under low-LET irradiation. *Physics in Medicine & Biology*, **66 (17)**, 175 026.
- Ramos-Méndez, J., J. Perl, J. Schuemann, A. McNamara, H. Paganetti, and B. Faddegon, 2018: Monte Carlo simulation of chemistry following radiolysis with TOPAS-nBio. *Physics in Medicine & Biology*, **63 (10)**, 105 014.
- Ramos-Méndez, J., W.-G. Shin, M. Karamitros, J. Domínguez-Kondo, N. H. Tran, S. Incerti, C. Villagrasa, Y. Perrot, V. Štěpán, S. Okada, E. Moreno-Barbosa, and B. Faddegon, 2020: Independent reaction times method in Geant4-DNA: Implementation and performance. *Medical physics*, **47 (11)**, 5919–5930.
- Rogers, D., 2006: Fifty years of Monte Carlo simulations for medical physics. *Physics in Medicine & Biology*, **51 (13)**, R287.
- Romesser, P. B., O. Cahlon, E. Scher, Y. Zhou, S. L. Berry, A. Rybkin, K. M. Sine, S. Tang, E. J. Sherman, R. Wong, et al., 2016: Proton beam radiation therapy results in significantly reduced toxicity compared with intensity-modulated radiation therapy for head and neck tumors that require ipsilateral radiation. *Radiotherapy and Oncology*, **118 (2)**, 286–292.

- Rørvik, E., L. F. Fjæra, T. J. Dahle, J. E. Dale, G. M. Engeseth, C. H. Stokkevåg, S. Thörnqvist, and K. S. Ytre-Hauge, 2018: Exploration and application of phenomenological RBE models for proton therapy. *Physics in Medicine & Biology*, **63** (18), 185 013.
- Rothwell, B. C., N. Kirkby, M. J. Merchant, A. Chadwick, M. Lowe, R. I. Mackay, J. H. Hendry, and K. J. Kirkby, 2021: Determining the parameter space for effective oxygen depletion for FLASH radiation therapy. *Physics in Medicine & Biology*, **66** (5), 055 020.
- Schaffner, B. and E. Pedroni, 1998: The precision of proton range calculations in proton radiotherapy treatment planning: experimental verification of the relation between CT-HU and proton stopping power. *Physics in Medicine & Biology*, **43** (6), 1579.
- Schneider, U., A. Lomax, and N. Lombriser, 2000: Comparative risk assessment of secondary cancer incidence after treatment of hodgkin's disease with photon and proton radiation. *Radiation research*, **154** (4), 382–388.
- Schuemann, J., A. L. McNamara, J. Ramos-Méndez, J. Perl, K. D. Held, H. Paganetti, S. Incerti, and B. Faddegon, 2019: TOPAS-nBio: An Extension to the TOPAS Simulation Toolkit for Cellular and Sub-cellular Radiobiology. *Radiation Research*, **191**, 125.
- Shrivastav, M., L. P. De Haro, and J. A. Nickoloff, 2008: Regulation of DNA double-strand break repair pathway choice. *Cell research*, **18** (1), 134–147.
- Sonoda, E., H. Hochegger, A. Saberi, Y. Taniguchi, and S. Takeda, 2006: Differential usage of non-homologous end-joining and homologous recombination in double strand break repair. *DNA repair*, **5** (9-10), 1021–1029.
- Štefanić, I. and J. A. LaVerne, 2002: Temperature dependence of the hydrogen peroxide production in the γ -radiolysis of water. *The Journal of Physical Chemistry A*, **106** (2), 447–452.
- Sung, H., J. Ferlay, R. L. Siegel, M. Laversanne, I. Soerjomataram, A. Jemal, and F. Bray, 2021: Global cancer statistics 2020: GLOBOCAN estimates of incidence and mortality worldwide for 36 cancers in 185 countries. *CA: a cancer journal for clinicians*, **71** (3), 209–249.
- Tatsuzaki, H., M. M. Urie, and R. Linggood, 1992: Comparative treatment planning: proton vs. x-ray beams against glioblastoma multiforme. *International Journal of Radiation Oncology* Biology* Physics*, **22** (2), 265–273.

- Testa, M., J. Schuemann, H.-M. Lu, J. Shin, B. Faddegon, J. Perl, and H. Paganetti, 2013: Experimental validation of the TOPAS Monte Carlo system for passive scattering proton therapy. *Medical Physics*, **40** (12), 1–16.
- Thermo Fisher Scientific Inc, 2023: Amplex Red Hydrogen Peroxide/ Peroxidase Assay Kit. URL <https://www.thermofisher.com/order/catalog/product/de/de/A22188>.
- Tilly, N., J. Johansson, U. Isacson, J. Medin, E. Blomquist, E. Grusell, and B. Glimelius, 2005: The influence of RBE variations in a clinical proton treatment plan for a hypopharynx cancer. *Physics in Medicine & Biology*, **50** (12), 2765.
- Tobias, C., J. Lawrence, J. Born, R. McCombs, J. Roberts, H. Anger, B. Low-Beer, and C. Huggins, 1958: Pituitary irradiation with high-energy proton beams a preliminary report. *Cancer research*, **18** (2), 121–134.
- Ward, J. F., 1988: DNA damage produced by ionizing radiation in mammalian cells: identities, mechanisms of formation, and reparability. *Progress in nucleic acid research and molecular biology*, **35**, 95–125.
- Wardman, P., 2022: Approaches to modeling chemical reaction pathways in radiobiology. *International Journal of Radiation Biology*, **98** (9), 1399–1413.
- Warmenhoven, J. W., N. T. Henthorn, S. P. Ingram, A. L. Chadwick, M. Sotiropoulos, N. Korabel, S. Fedotov, R. I. Mackay, K. J. Kirkby, and M. J. Merchant, 2020: Insights into the non-homologous end joining pathway and double strand break end mobility provided by mechanistic in silico modelling. *DNA Repair*, **85**, 102743.
- Wedenberg, M., B. K. Lind, and B. Hårdemark, 2013: A model for the relative biological effectiveness of protons: the tissue specific parameter α/β of photons is a predictor for the sensitivity to LET changes. *Acta oncologica*, **52** (3), 580–588.
- Wedenberg, M. and I. Toma-Dasu, 2014: Disregarding RBE variation in treatment plan comparison may lead to bias in favor of proton plans. *Medical physics*, **41** (9), 091706.
- Wilkens, J. and U. Oelfke, 2004: A phenomenological model for the relative biological effectiveness in therapeutic proton beams. *Physics in Medicine & Biology*, **49** (13), 2811.
- Wilson, R. R., 1946: Radiological use of fast protons. *Radiology*, **47** (5), 487–491.

- Withers, H. R., 1975: The four R's of radiotherapy. *Advances in radiation biology*, Elsevier, Vol. 5, 241–271.
- World Health Organization, 2020: The top 10 causes of death. URL <https://www.who.int/news-room/fact-sheets/detail/the-top-10-causes-of-death>.
- Wouters, B., G. Lam, U. Oelfke, K. Gardey, R. Durand, and L. Skarsgard, 1996: Measurements of relative biological effectiveness of the 70 MeV proton beam at TRIUMF using Chinese hamster V79 cells and the high-precision cell sorter assay. *Radiation research*, **146 (2)**, 159–170.
- Wouters, B. G., L. D. Skarsgard, L. E. Gerweck, A. Carabe-Fernandez, M. Wong, R. E. Durand, D. Nielson, M. R. Bussiere, M. Wagner, P. Biggs, et al., 2015: Radiobiological intercomparison of the 160 MeV and 230 MeV proton therapy beams at the Harvard Cyclotron Laboratory and at Massachusetts General Hospital. *Radiation Research*, **183 (2)**, 174–187.
- Zhu, H., A. L. McNamara, J. Ramos-Mendez, S. J. McMahon, N. T. Henthorn, B. Faddegon, K. D. Held, J. Perl, J. Li, H. Paganetti, et al., 2020: A parameter sensitivity study for simulating DNA damage after proton irradiation using TOPAS-nBio. *Physics in Medicine & Biology*, **65 (8)**, 085015.

Published articles

Article 1, article 2 and article 3 are printed with permission from the Institute of Physics and Engineering in Medicine. Reproduced with permission. All rights reserved. All articles have been published with an open access and are freely available.



PAPER

OPEN ACCESS

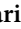


RECEIVED
12 April 2021REVISED
27 July 2021ACCEPTED FOR PUBLICATION
12 August 2021PUBLISHED
31 August 2021

Original content from this work may be used under the terms of the [Creative Commons Attribution 4.0 licence](#).

Any further distribution of this work must maintain attribution to the author(s) and the title of the work, journal citation and DOI.



Investigating the feasibility of TOPAS-nBio for Monte Carlo track structure simulations by adapting GEANT4-DNA examples application

Larissa Derksen¹, Tabea Pfuhl² , Rita Engenhardt-Cabillic^{3,4}, Klemens Zink^{1,3,4}  and Kilian-Simon Baumann^{1,3,4} 

¹ University of Applied Sciences, Institute of Medical Physics and Radiation Protection, Giessen, Germany

² GSI Helmholtzzentrum für Schwerionenforschung, Darmstadt, Germany

³ University Medical Center Giessen-Marburg, Department of Radiotherapy and Radiooncology, Marburg, Germany

⁴ Marburg Ion-Beam Therapy Center (MIT), Marburg, Germany

E-mail: larissa.derksen@biotecmed.thm.de

Keywords: Monte Carlo, GEANT4, GEANT4-DNA, TOPAS, TOPAS-nBio, track structure, low-energy electrons

Abstract

Purpose. The purpose of this work is to investigate the feasibility of TOPAS-nBio for track structure simulations using tuple scoring and ROOT/Python-based post-processing. **Materials and methods.** There are several example applications implemented in GEANT4-DNA demonstrating track structure simulations. These examples are not implemented by default in TOPAS-nBio. In this study, the tuple scorer was used to re-simulate these examples. The simulations contained investigations of different physics lists, calculation of energy-dependent range, stopping power, mean free path and W -value. Additionally, further applications of the TOPAS-nBio tool were investigated, focusing on physical interactions and deposited energies of electrons with initial energies in the range of 10–60 eV, not covered in the recently published GEANT4-DNA simulations. Low-energetic electrons are currently of great interest in the radiobiology research community due to their high effectiveness towards the induction of biological damage. **Results.** The quantities calculated with TOPAS-nBio show a good agreement with the simulations of GEANT4-DNA with deviations of 5% at maximum. Thus, we have presented a feasible way to implement the example applications included in GEANT4-DNA in TOPAS-nBio. With the extended simulations, an insight could be given, which further tracking information can be gained with the track structure code and how cross sections and physics models influence a particle's fate. **Conclusion.** With our results, we could show the potentials of applying the tuple scorer in TOPAS-nBio Monte Carlo track structure simulations. Using this scorer, a large amount of information about the track structure can be accessed, which can be analyzed as preferred after the simulation.

1. Introduction

In the field of radiotherapy and radiation protection, Monte Carlo simulations are a frequently used tool in research and clinical applications (Rogers 2006). However, since Monte Carlo simulations often require very good programming skills, many codes are not suitable for clinical applications, and medical physicists without advanced programming skills. Therefore, the Monte Carlo toolkit TOPAS (TOol for PArticle Simulation) (Perl *et al* 2012, Faddegon *et al* 2020) was developed, which makes Monte Carlo simulations more accessible for researchers and clinical users due to its ease of use. The toolkit is based on the already established open access Monte Carlo code GEANT4 (Agostinelli *et al* 2003, Allison *et al* 2006). This means that TOPAS implies the same physics models and cross section data as GEANT4, but with the difference that the simulations do not have to be written in programming language C++. Simulation geometries, particle sources, scorers, and physics parameters are defined using simple text-based commands. The user can choose from a large variety of

predefined options, however, TOPAS can still be used flexibly since advanced users can make use of extensions. Initially, it was applied for proton therapy, but now it can also be used in many other areas of radiation therapy and some medical imaging applications. The tool has already been well-validated against experimental data in previous studies (Perl *et al* 2012, Testa *et al* 2013).

Additionally, the TOPAS collaboration has released an extension named TOPAS-nBio (Schuemann *et al* 2019) (available since August 2019), based on the Monte Carlo Code GEANT4-DNA, for running radiobiology simulations at cellular and sub-cellular scales. For typical clinical applications like dose calculations and dosimetry, simulations are performed on macroscopic scales, while in most cases the condensed history approach is used to reduce computing time. In the condensed history approach, several single scattering events are condensed into one multiple scattering event, while the energy deposition and scattering angle are being determined statistically using corresponding algorithms. The disadvantage of this approach is, however, that it only achieves a reduced spatial resolution of the local deposited energy. In contrast, simulations on small scales like cellular and sub-cellular levels are usually performed using Monte Carlo track structure codes such as GEANT4-DNA to track particles step by step until they reach energies of a few eV. Track structure codes provide the required physics models and precise cross section data, which are not included in conventional codes. Still, this approach is more time consuming than the condensed history approach (Tajik-Mansoury *et al* 2017). For clinical applications on mm-scales, cut-off energies of 1–10 keV are usually used, whereas for simulations investigating the biological response directly at the DNA or on cellular levels (nm- μ m), the particles have to be tracked down to a few eV. For example, electrons with an energy of 10 keV have a residual range in water of ca. 2.5 μ m, which is sufficient for macroscopic simulations. However, for simulations on the microscopic level, residual ranges of ca. 3 nm with corresponding electron energies of 20 eV are crucial.

Making use of track structure codes, nanodosimetric quantities like DNA strand breaks and the distribution of ionization clusters can be investigated, which is expected to improve the prediction of the biological effectiveness of heavy charged particle radiation. This might lead to a development of new models of the relative biological effectiveness (RBE) or to the refinement of already existing radiobiological models. In addition to the TOPAS-nBio extension, there is also a microdosimetric extension available focusing on simulations on cellular scales. This extension can be applied to simulate microdosimetric spectra and perform calculations of RBE as well. To calculate microdosimetric quantities, a special microdosimetric scorer is used, which scores each interaction with an energy deposition greater than zero in a corresponding microdosimeter. Contrary to TOPAS-nBio, g4em-standard physics lists are used. Details are described by Zhu *et al* (2019).

TOPAS-nBio is used to link GEANT4-DNA (Incerti *et al* 2010a) with TOPAS making new physics lists available in order to simulate track structures down to the eV-regime. Geometry components for biological targets e.g. several DNA models and cellular structures are also accessible in this tool. These are described in detail by McNamara *et al* (2018). In addition to the simulation of physical interactions, chemical interactions (Karamitros *et al* 2011) and also biological aspects like DNA repair models (McMahon *et al* 2016, Warmenhoven *et al* 2020) can be taken into consideration in order to study the biological damage induced by ionizing particles. Chemical interactions are of particular interest for low-LET radiation since a great amount of damage to the DNA is caused by indirect effects of the radiation such as chemical radicals (Sanche 2012). This toolkit of TOPAS based on the physics lists and chemistry models from GEANT4-DNA has been validated against previous simulation studies and experimental data. This was done by comparing the prediction of DNA damage in different geometries to measurement data and previously performed simulation studies (McNamara *et al* 2017). More studies have already been published investigating TOPAS-nBio for nanodosimetric simulations showing the potential of this extension. Zhu *et al* (2020) investigated the effect of different physics and chemical models in TOPAS-nBio on the yield of the single strand break (SSB) and double strand break (DSB) in proton simulations. Furthermore, in a study by Hahn and Villate (2021), the extension was used to determine the effect of different geometric models of the distribution of nanoparticles within a cell in simulations using gold nanoparticles for dose enhancement by simulation the radioactive decay of ^{198}Au and focusing on the deposited energy of different cell organelles.

With the release of GEANT4-DNA, the example repertoire of GEANT4 was extended with eleven examples considering track structure simulations with GEANT4-DNA, which are described and analyzed in detail by Incerti *et al* (2018) (hereinafter Incerti2018). These simulations include the examples *dnaphysics*, *range*, *spower*, *mfp*, and *w value*, which will be further specified in sections 2.1.1–2.1.5. In TOPAS-nBio, these examples are not in any way pre-programmed and the corresponding values of those examples cannot be scored directly. In the first part of this research, the main focus was to investigate the feasibility of performing these example simulations in TOPAS-nBio. We present a solution to determine the physical properties by taking advantage of the tuple scorer, which stores detailed tracking information of track structure simulations in one single output file. Using this method, a high programming effort is avoided. We intended to re-simulate especially the five examples that were investigated by Incerti2018 with TOPAS-nBio since they are often used as key quantities for

evaluating track structure codes. Further, to validate this model, simulation results using TOPAS-nBio were compared to those performed with the pre-programmed examples in GEANT4-DNA.

In a second part, further applications of the TOPAS-nBio tool were investigated, focusing on physical interactions and deposited energies of electrons of low energies in the range of 10–60 eV. This energy range was chosen since the most probable energy of secondary electrons produced by a primary ion of clinically relevant energies is approximately 10 eV and the mean energy is about 50–60 eV (Pimblott and LaVerne 2007). By using the tuple scorer, the individual fate of each electron could be examined and analyzed in detail.

2. Materials and methods

2.1. GEANT4-DNA example applications

At the beginning of this section, we will briefly introduce the examples that were re-simulated during this study and previously carried out with GEANT4-DNA by Incerti2018. All simulations were performed in liquid water. Details such as simulation parameters will be further discussed in the following subsections.

2.1.1. Dnaphysics example

The occurrence of various electron, proton, and hydrogen processes is counted from a total of 100 primary protons with an initial energy of 100 keV.

2.1.2. Range example

The energy-dependent range r of one particle is determined as the sum of all step lengths between two interaction points. The step length is calculated using the three-dimensional Pythagorean theorem and the coordinates x, y, z of each trajectory point s :

$$r = \sum_{s=1}^{N_s-1} \sqrt{(x_s - x_{s+1})^2 + (y_s - y_{s+1})^2 + (z_s - z_{s+1})^2}, \quad (1)$$

where N_s is the maximum step number.

2.1.3. Spower example

The energy-dependent stopping power s of the particles is studied. For this purpose, the sum of the deposited energy E_s of each step s per primary particle is divided by the corresponding range r (see above):

$$s = \frac{\sum_{s=1}^{N_s} E_s}{r}. \quad (2)$$

2.1.4. Mean free path (Mfp) example

The mfp is the average length of the first step of a particle with a certain kinetic energy. The inelastic mean free path (imfp) is the average length of the first step of a particle considering only inelastic interactions, in which case elastic interactions are not simulated. Since the coordinates of the first trajectory point are located in the origin, this results in the following expression:

$$\text{mfp} = \frac{\sum_{e=0}^N \sqrt{x_{1,e}^2 + y_{1,e}^2 + z_{1,e}^2}}{N}. \quad (3)$$

Here N is the number of events e . This equation is also valid for the calculation of the imfp.

2.1.5. W value example

The W -value w is determined by the ratio of the initial particle energy E and the mean number of ionizations $\overline{N_{ion}}$ per event:

$$w = \frac{E}{\overline{N_{ion}}}. \quad (4)$$

2.2. Simulations of GEANT4-DNA example applications using TOPAS-nBio

In the simulations performed with TOPAS (Perl *et al* 2012), we used TOPAS version 3.2.p2, which is based on the GEANT4 version 10.05.p01. The features of TOPAS-nBio are made accessible by several extensions provided by the TOPAS collaboration. We used TOPAS-nBio v1.0-beta.1. Even though the latest GEANT4 version (GEANT4 10.07) is already released, there is no disadvantage of running the simulations based on GEANT4

version 10.05, as there are no significant differences when comparing the example results from those two different GEANT4 versions as shown in the [appendix](#).

Most of the necessary simulation parameters, such as those concerning geometry and radiation source, are described in Incerti2018 and could thus be easily adapted in the TOPAS simulations. All remaining parameters were extracted from the simulation files provided on GitHub⁵ by the GEANT4 collaboration. These are summarized in table 1. In each simulation, except of the *dnaphysics* example, an isotropic particle source was placed at the center of a sphere with a radius of 1 m. This was filled with liquid water (*G4_WATER*) since cross sections data in GEANT4-DNA are only available for liquid water and DNA-related materials. Using *G4_WATER*, water has a density of 1.0 g cm^{-3} and a mean ionization potential of $I_W = 78 \text{ eV}$. In the *dnaphysics* example application the particle source was placed in the middle of a box with an edge length of $100 \mu\text{m}$. The physics lists *G4EmDNAPhysics_option2*, *G4EmDNAPhysics_option4* and *G4EmDNAPhysics_option6* were used in separate runs for all simulations concerning electrons. Simulations for protons and alpha particles in the range example were performed using *G4EmDNAPhysics_option2*. For a correct calculation of the stopping power of electrons, *G4EmDNAPhysics_stationary_opt2*, *G4EmDNAPhysics_stationary_opt4* and *G4EmDNAPhysics_stationary_opt6* needed to be used, since here the kinetic energy of the particle is constant in each step as described by Incerti2018. In most simulations the default tracking cut of the particles was applied; details are listed in table 1. The number of primary particles was set between 10^2 and 10^4 depending on the particle type and example application similar to Incerti2018. In the *mfp* example, the *mfp* was once investigated including all electron processes and a second time considering only inelastic interactions (*imfp*) as done by Incerti2018. For the calculation of the *imfp*, we used a physics list adopted from *TsEmDNAPhysics*, so that elastic interactions could be inactivated. All other physics models and processes were implemented as it is the case in *G4EmDNAPhysics_option2*, *G4EmDNAPhysics_option4*, and *G4EmDNAPhysics_option6* which is specified in table 2.

Contrary to GEANT4, the simulations are not pre-programmed in TOPAS, and the results are not directly obtained after running the simulation as it is the case in GEANT4. In order to still be able to calculate these corresponding quantities, we used the tuple scorer in our simulations. This scorer stores information related to a particle track such as the particle type and the *x*-, *y*- and *z*-position of the trajectory step point in one file. In addition, the user can decide whether additional tracking information should be included in the output file by selecting items from the following list:

- EventID (number of the primary particle)
- TrackID (identification number to differentiate between tracks of primary and secondary particles)
- Step number (number of the step of the corresponding track)
- Particle name
- Process name
- Volume name
- Volume copy number (copy number of a volume, if its geometry is copied in the simulation)
- ParentID (track identification numbers of the parent tracks of chemical reactions)
- Vertex position *x/y/z* (coordinates of the step points of secondary particle tracks in relation to their origin)
- Global time (time of flight)
- Energy deposited
- Kinetic energy (before interaction)

The respective quantity of each example could then be calculated from the corresponding tracking information. For some simulations, it was also useful to add filters to the scorers, e.g. when focusing exclusively on primary particles or particles of a given type. This can be a helpful feature, for example, to keep the output files small and to simplify and speed up the analysis. An overview of possible scoring filters is provided on the TOPAS documentation website⁶ by the TOPAS collaboration. The tuple scorer provided by TOPAS does only account for interactions with an energy transfer larger than 0 eV. In order to score elastic scatterings also, the tuple scorer was adapted to score events with an energy transfer of 0 eV. All data were stored in a ROOT file.

⁵ <https://github.com/Geant4/geant4/tree/master/examples/extended/medical/dna>

⁶ <https://topas.readthedocs.io/en/latest/>

Table 1. Overview of the relevant simulation parameters applied in the different examples in this study using TOPAS-nBio.

	Dnaphysics	Range	Spower	Mfp	W value
Geometry	TsBox with edge length of 100 μm	TsSphere $r = 1 \text{ m}$	TsSphere $r = 1 \text{ m}$	TsSphere $r = 1 \text{ m}$	TsSphere $r = 1 \text{ m}$
Material Source	G4_WATER Particle type: p Particle energy: 100 keV	G4_WATER Particle type: e-, p, α Particle energy: e-: 10–10 ⁶ eV p: 10 ³ –10 ⁶ eV α : 10 ³ –10 ⁶ eV	G4_WATER Particle type: e- Particle energy: e-: 10–10 ⁶ eV	G4_WATER Particle type: e- Particle energy: 10–10 ⁶ eV	G4_WATER Particle type: e- Particle energy: 10–10 ⁶ eV
Physics lists	g4em-dna_opt2/4/6	g4em-dna_opt2/4/6	g4em-dna- stationary_opt2/4/6	g4em-dna_opt2/4/6, TsEmDNAPhysics2 ^a	g4em-dna_opt2/4/6
Transport Parameters	Tracking cut: default ^b	Tracking cut: e-: 10 eV p: 400 eV–3 keV ^c α : 1 keV	Tracking cut: default ^b	Tracking cut: default ^b	Tracking cut: default ^b
Scoring	MaxStepNumber: default ^d TupleAll ^e Process name	MaxStepNumber: default ^d TupleAll ^e EventID Deposited energy only primary particles	MaxStepNumber: 1000 TupleAll ^e EventID Only primary particles	MaxStepNumber: 1 TupleAll ^e (all) pTuple (incl.) EventID	MaxStepNumber: default ^d pTuple EventID Process name
Histories in Run	10 ²	e-: 10 ³ p, α : 10 ²	10 ⁴	10 ⁴	10 ⁴

^a Extension adapted from TsEMDNAPhysics to inactivate elastic scattering. Models for the different processes were selected according to the dna physics list options.

^b Default tracking cut for e-: opt2 = 7.4 eV, opt4 = 10 eV, opt6 = 11 eV, for p, H⁺ = 100 eV, for α = 1 keV.

^c The tracking cut was set to 400 eV at initial proton energies of 1 keV and to 3 keV for initial energies greater than or equal to 500 keV. For all intermediate energies the tracking cut was interpolated logarithmically.

^d Default MaxStepNumber = 10⁶.

^e Extension adapted from pTuple-Scorer, but modified so that all processes (also those with edep = 0 \rightarrow elastic scattering) are included.

Table 2. Settings of the physics models used for the simulation of the imfp so that they correspond to the physics lists *G4EmDNAPhysics_option2/4/6*. Elastic scattering is switch off, since only inelastic interactions are taking into account when calculating imfp. Electron solvation does not need to be specified since it just operates as tracking cut.

Process	Option 2	Option 4	Option 6
Ionization	Born ^a	Emfietzoglou ^b	CPA100 ^c
Excitation	Born ^a	Emfietzoglou ^b	CPA100 ^c
Attachment	True	False	False
Vibrational excitation	True	False	False
Elastic scattering	False	False	False

^a Incerti *et al* (2010b).

^b Kyriakou *et al* (2015).

^c Bordage *et al* (2016).

Table 3. Brief overview of all possible electron processes included in GEANT4-DNA.

Process name	Definition
Attachment	Electron sub-excitation process; capture of an electron by a electrically neutral molecule, when the kinetic energy is less than the ionization potential and matches the quasibound state of the molecule. OH ⁻ , H ⁻ and O ⁻ ions are produced by the electron interacting with liquid water (Melton 1972, Denifl <i>et al</i> 2012).
Elastic scattering	Scattering of the particle interacting with free and bound atoms. In <i>G4EmDNAPhysics_option2</i> and <i>G4EmDNAPhysics_option4</i> , there is no energy transfer, whereas in <i>G4EmDNAPhysics_option6</i> a tiny fraction of energy is transferred and the total momentum of the whole system is conserved.
Electron solvation	Accumulation of water molecules around a free electron. In GEANT4-DNA, the tracking cut is represented by this process when chemical processes are inactivated. Electrons that reach the tracking cut are then assumed to be solvated (Incerti <i>et al</i> 2018).
Electronic excitation	Energy transfer to a bound electron of a molecule with the result that it is excited to a higher energy level. Consideration of the electron excitation states of liquid water.
ionization	Detachment of an electron from the electron shell of a neutral atom or molecule, resulting in a positive ion. Taking into account the ionization energies for the valence electrons and the K-shell.
Vibrational excitation	Small energy depositions inducing excitation of the vibrational state of the interacting molecule (Michaud <i>et al</i> 2003). Nine excitation phonon modes are taken into account.

To validate our method, simulation results using TOPAS-nBio based on GEANT4 version 10.05 were benchmarked with those of GEANT4-DNA using the same software version. The simulations with GEANT4-DNA were performed using the pre-programmed example files included in GEANT4. When running the simulation files, the user directly receives a file in which the results are listed. Thus, there is no need for additional calculations.

2.3. Extended simulation to investigate the processes of low-energy electrons

The occurrence of physical processes stated in table 3 for electrons of energies between 10 and 60 eV was studied using the physics list *G4EmDNAPhysics_opt2*. An isotropic source emitting 100 electrons was placed at the center of a cube with an edge length of 100 μm filled with liquid water. The tracking of the particles was terminated by applying the default tracking cut of 7.4 eV. The tuple scorer was applied to investigate detailed track structure information. Post-processing those data, the following investigations were made:

- (i) The frequency of electron processes was investigated by counting each process in total of all 100 primary particles and their secondaries.
- (ii) Since the deposited energy is of particular interest when considering the effect of radiation on DNA scales, this parameter was studied in more detail. The mean deposited energy of a single interaction was calculated per process.
- (iii) Additionally, the sum of the deposited energy of each process per primary particle was calculated.
- (iv) The maximum energy deposited for each process was investigated.
- (v) The chronological order in which the processes of different events and for different initial energies occur along one track was investigated.

2.4. Analysis of the TOPAS simulations

In order to evaluate the output of the simulations from TOPAS, we used ROOT version 6.20.04, an open-source analysis framework developed and provided by CERN (Brun and Rademakers 1997), and Python 2.7.17. ROOT offers the user the possibility to choose Python for an evaluation of the ROOT files by importing the module `root_numpy` into Python. More precisely, we used the function `root2array` for converting a tree, a special structure in a ROOT file containing the stored data, into a numpy structured array. Then, all tracking data could be commonly accessed and processed with Python.

In this study, the corresponding properties were determined in each event individually and then averaged over the complete set of events to determine a mean value and the associated standard deviation. Since no statistical values can be estimated by simulating just one run of the *dnaphysics* example, the standard deviation was calculated using the results of 20 independent runs performed with different random seeds.

3. Results and discussion

3.1. Simulations of GEANT4-DNA example applications using TOPAS-nBio

3.1.1. *Dnaphysics*

Figure 1 shows the frequency of individual processes simulated with TOPAS-nBio and GEANT4-DNA using different physics lists. In the bottom panels, the relative deviation from TOPAS-nBio to GEANT4-DNA is visualized. For each process the deviations are smaller than 1.2%. Comparing the counts of each process using *G4EmDNAPhysics_opt2*, the greatest deviation is 1.2% for electron attachment and the average deviation of all processes using is physics list option 0.2%. Using *G4EmDNAPhysics_opt4* and *G4EmDNAPhysics_opt6*, a maximum deviation of 1.2% and 1.1% respectively is observed for hydrogen excitation. On average the values of TOPAS-nBio and GEANT4-DNA deviate by 0.1% using these two physics lists. However, all values between TOPAS-nBio and GEANT4-DNA coincide within one standard deviation.

In addition, figure 2 shows the comparison of the counts per process simulated with TOPAS-nBio using these three physics list options by calculating the percentage deviation between two options. The physics list that is listened first in the legend was always selected as the ‘original data’. For example, the calculation of the data series 2 versus 4 was performed as follows:

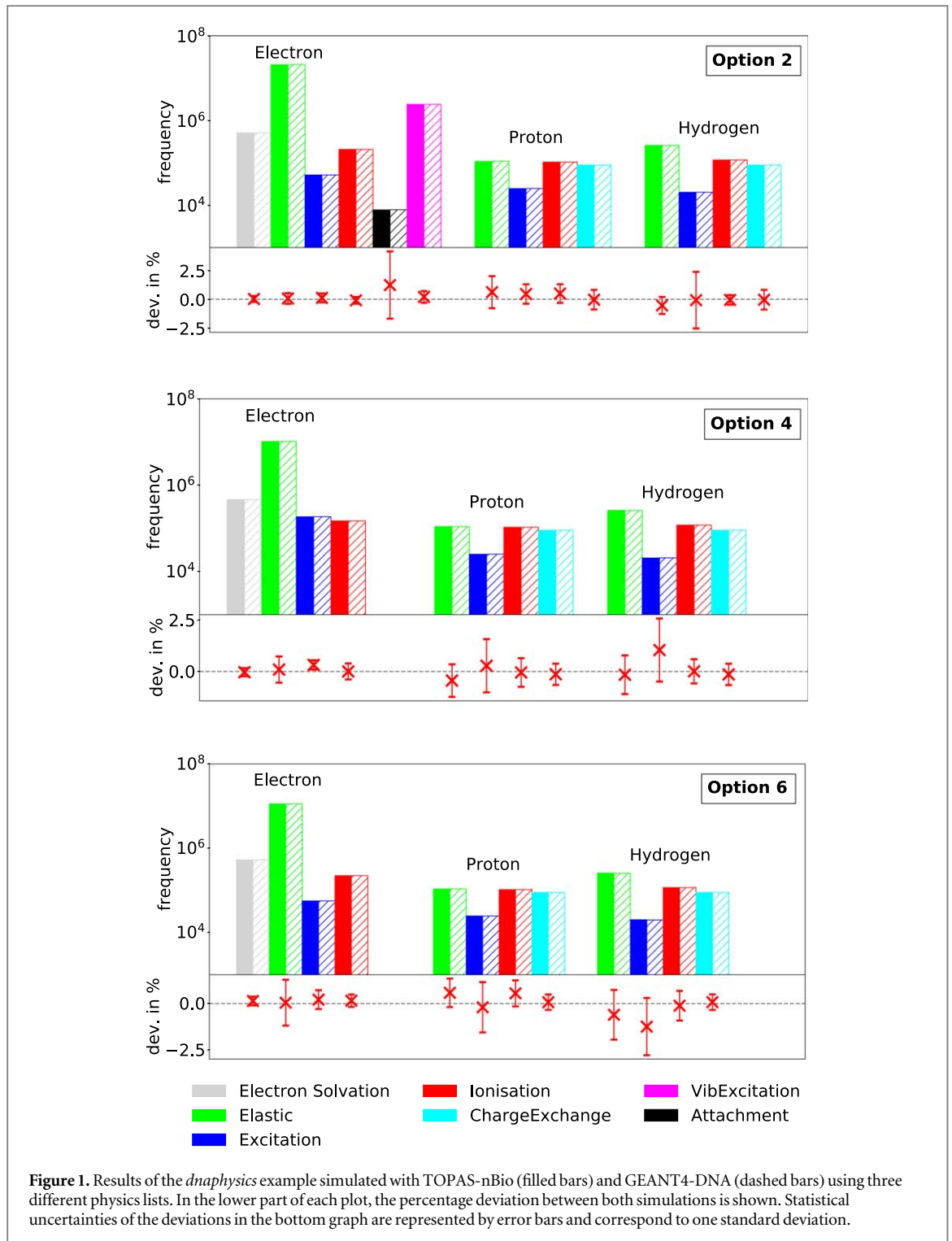
$$d_p = \frac{x_{p,opt2} - x_{p,opt4}}{x_{p,opt2}} * 100. \quad (5)$$

Here, d_p is the percentage difference of process p , $x_{p,opt2}$ the counts of process p using physics lists option 2 and $x_{p,opt4}$ the counts of process p using physics lists option 4.

The differences between the individual physics lists are quite low for proton and hydrogen processes since the models of these processes are the same for each physics list option. The deviations are of statistical nature. For electron processes, the absolute differences are between 3.6% and 255%. On average, electron processes deviate by 46% for the different physic list options, thus, the correct choice for simulations in TOPAS-nBio is of great importance since simulation results can differ significantly depending on the applied physics list.

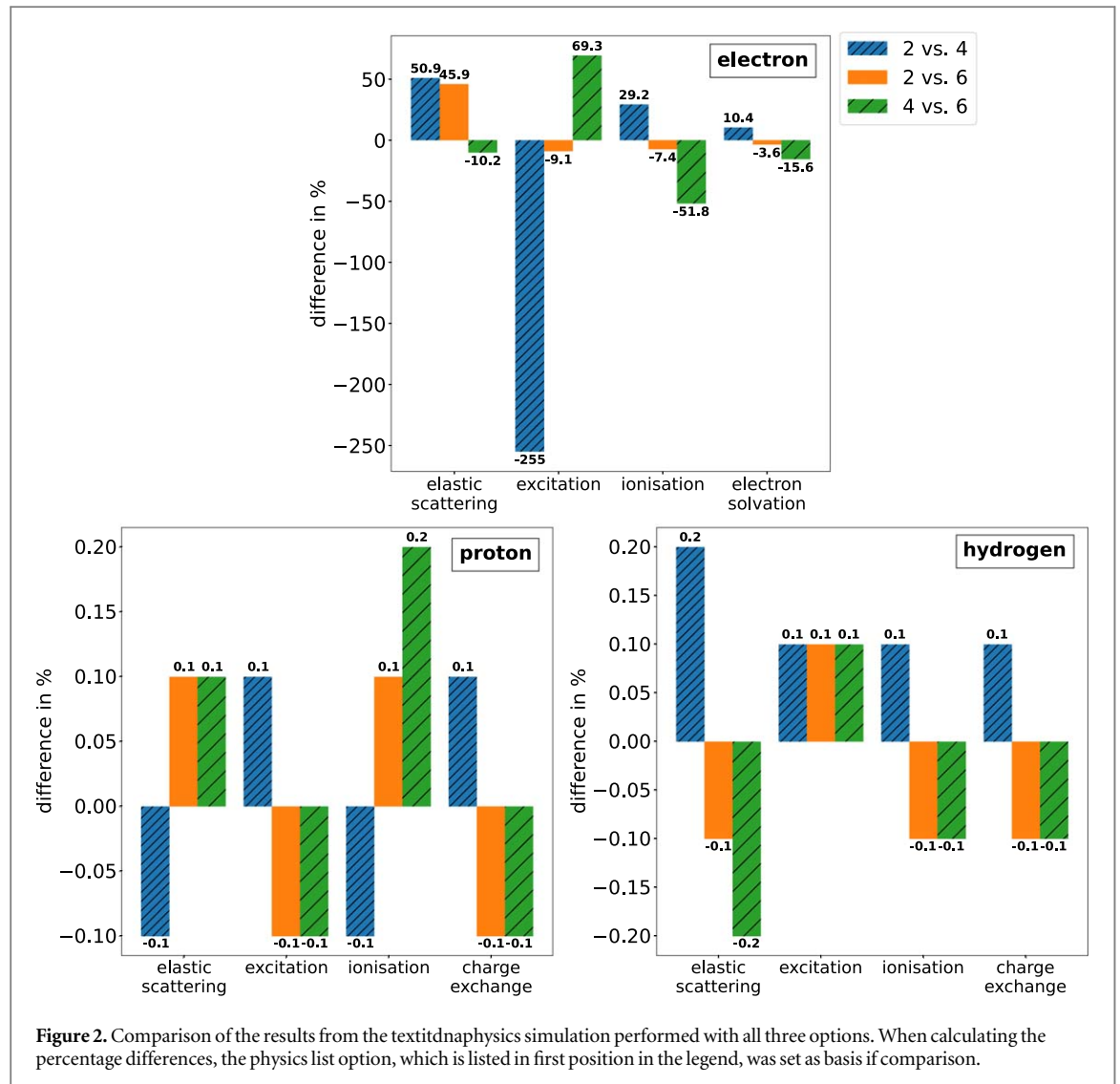
3.1.2. Range

In figure 3(a), the range of the investigated particles is shown as a function of initial energy calculated with TOPAS-nBio and GEANT4-DNA using different physics lists. In TOPAS-nBio, more initial energies were investigated compared to the GEANT4-DNA simulations. Hence, the individual data points produced with TOPAS-nBio are connected by a line to guide the eye. Additionally, the ICRU90 (ICRU 2016) ranges of the particles are illustrated. In figure 3(b), the deviations between the TOPAS-nBio simulations and GEANT4-DNA are portrayed. Considering electrons, large relative deviation can only be observed at small, absolute ranges. For initial electron energies above 500 eV, deviations are smaller than 2%. Regarding option 4, the maximum deviation is slightly above 20%; considering option 2, the deviations range from -7.7% to 14.2% , and using option 6, a maximum deviation of 11.9% at an energy of 40 eV is observed. Nevertheless, the mean deviation for electrons using all three options is statistically disturbed around zero and all deviations are in order of one standard deviation. Here, no systematic deviations can be observed. In figure 3(c), the ranges for electrons of energies from 10 to 100 eV are shown in a zoom-in view. As described by Francis *et al* (2011), this range profile results from cross sections of inelastic scattering processes implemented in the physics list, which are significantly changing for small energies. This is a consequence of the tresholds for inelastic interactions located in this energy range. By undergoing an inelastic interaction, the particle loses kinetic energy reducing the residual range. Thus, these peaks at lower energies occur as the initial energy exceeds new tresholds for inelastic interactions. Since the tresholds and cross sections of each process differ in the different physics list



G4EmDNAPhysics_opt2, *G4EmDNAPhysics_opt4* and *G4EmDNAPhysics_opt6*, the profile of the range at low energies is also different for each simulated physics list.

When comparing the proton ranges in figure 3(d), it is interesting to note that the deviations between TOPAS-nBio and GEANT4-DNA are largest at an initial energy of 1 keV (30%) and then decrease systematically down to a minimum value of 0.6%. These deviations result from the fact that in the GEANT4-DNA pre-programmed examples the tracking cut was not adjusted as described in the study by Incerti2018. In the TOPAS-nBio simulations the tracking cut was set higher resulting in a lower range. Comparing the ranges calculated with TOPAS-nBio and GEANT4-DNA with ICRU90 data, it can be seen that the agreement between TOPAS-nBio and ICRU values is more accurately compared to GEANT4-DNA. For a more accurate comparison between GEANT4-DNA and TOPAS-nBio, the simulations were repeated in TOPAS-nBio, this time using the same



tracking cut (100 eV) as in GEANT4-DNA. With this adjustment, the values agree well with those of GEANT4-DNA (see figure 3(e)) and a maximum deviation of 0.6% could be obtained.

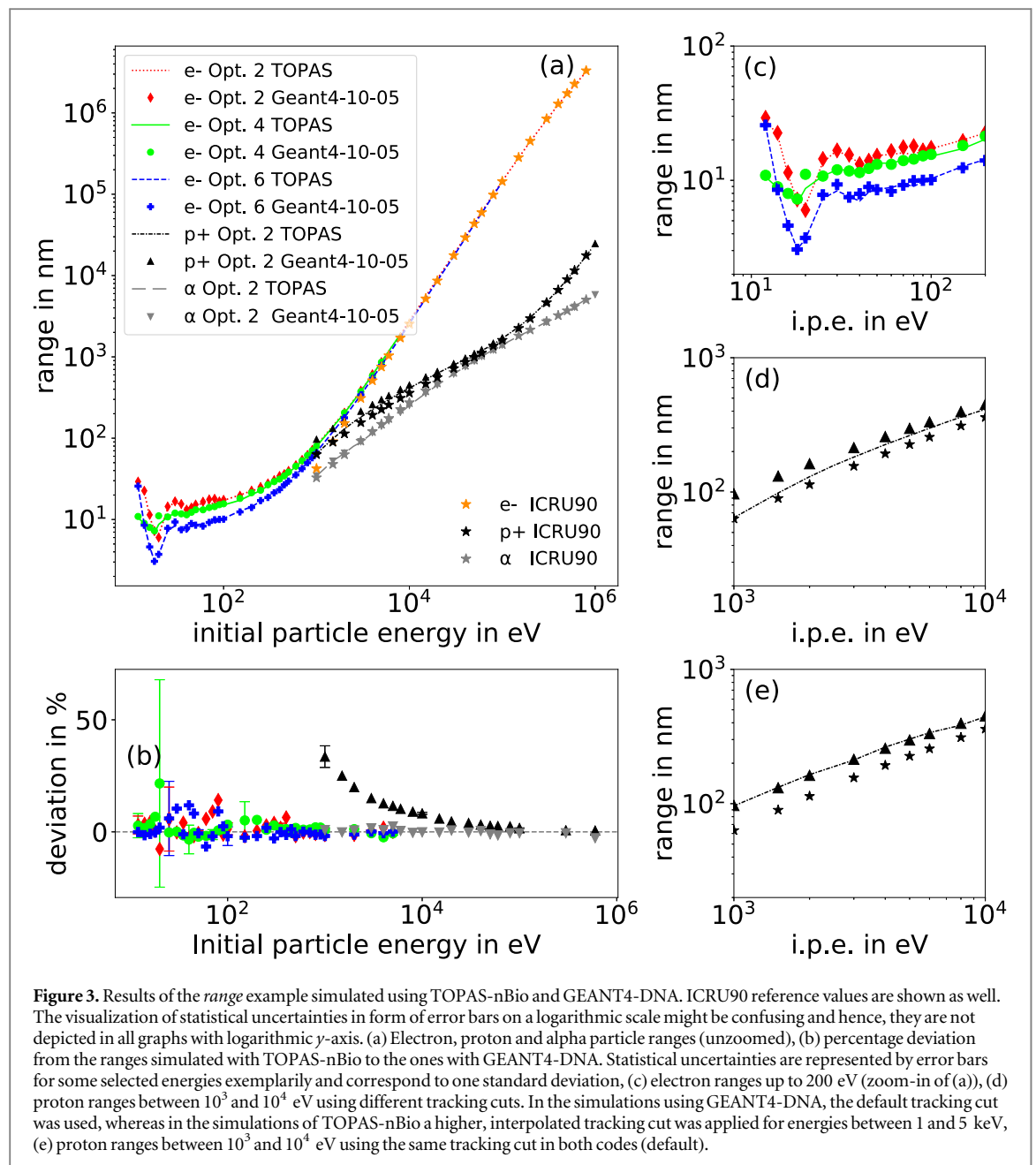
The ranges of alpha particles (see figure 3(a)) comply well with both the GEANT4-DNA values and the ICRU values, while deviations are smaller than 3% for all considered energies and coincide within one standard deviation.

3.1.3. *Spower*

Figure 4(a) shows the mean value of the stopping powers of all three physics list options as a function of the initial particle energy for electrons. Due to practical reasons, only four values were simulated in TOPAS-nBio per physics list. Therefore, the *x*-axis in 4(a) is discrete and the values of TOPAS-nBio and GEANT4-DNA are plotted side by side for a more concise illustration of the results. While using *G4EmDNAPhysics_stationary_opt2* and *G4EmDNAPhysics_stationary_opt6* a percentage deviation of 0.12% at maximum of the electron stopping powers is obtained, the deviation for *G4EmDNAPhysics_stationary_opt4* is ten times larger with 1.3%. It is noticeable that for *G4EmDNAPhysics_stationary_opt2* and *G4EmDNAPhysics_stationary_opt6*, the stopping powers obtained with TOPAS-nBio are always larger than those from GEANT4-DNA, and contrarily for *G4EmDNAPhysics_stationary_opt4*, all values from TOPAS-nBio are smaller than those from GEANT4-DNA. However, all values between TOPAS-nBio and GEANT4-DNA agree within one standard uncertainty. For transparency, the uncertainties of the *spower* example are shown in figure 4(a).

3.1.4. *Mfp*

In figure 4(b), the *mfp* including all processes for electrons is visualized and the *imfp* is shown in figure 4(c). The difference between TOPAS-nBio and GEANT4-DNA is smaller than 3% for the *mfp* simulation and 4% at

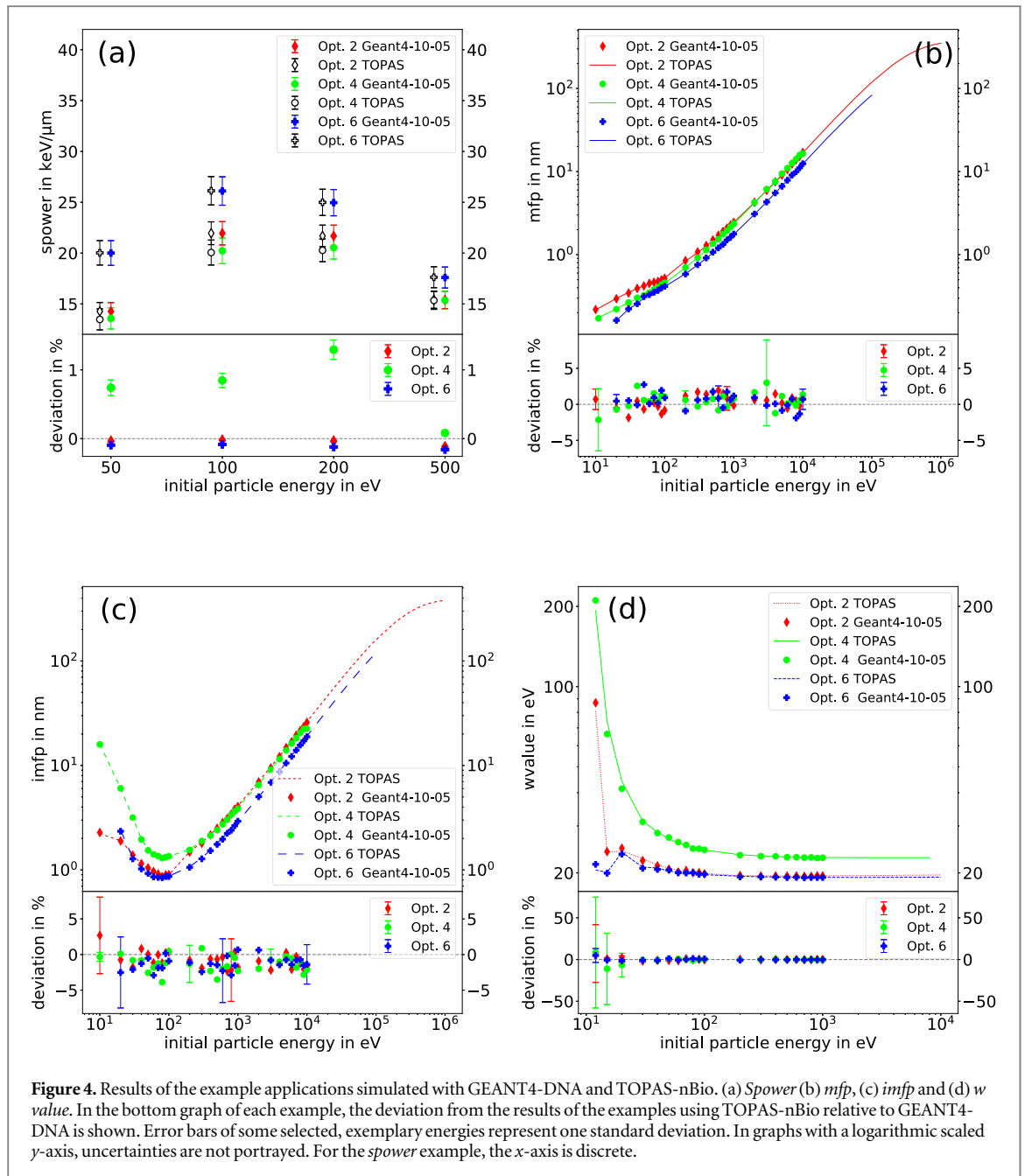


maximum for the *imfp* simulation. Nevertheless, all values coincide within one standard deviation and no systematic uncertainties can be recognized.

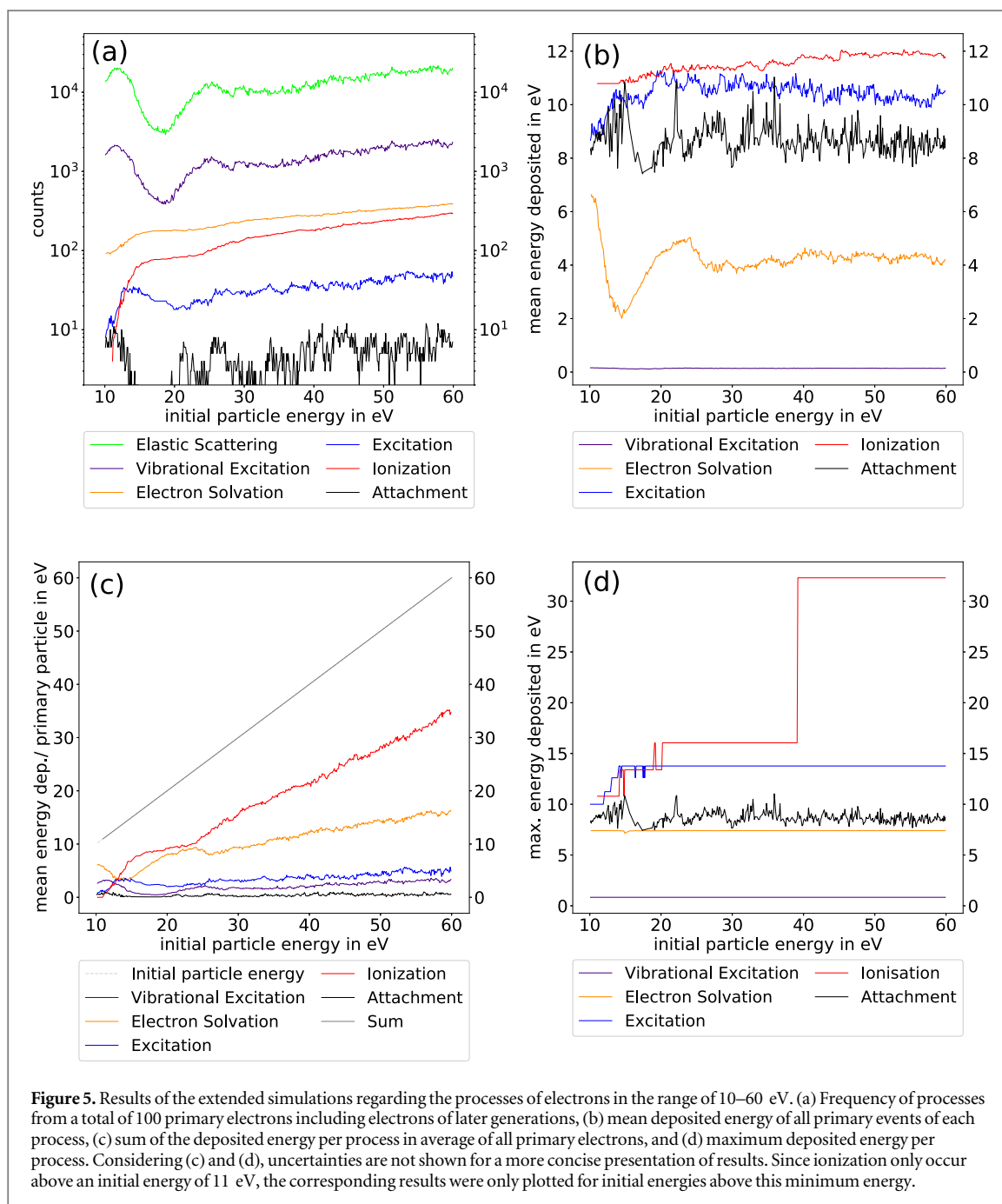
3.1.5. W value

Figure 4(d) shows the W -value as a function of the initial particle energy. The agreement between TOPAS-nBio and GEANT4-DNA is better than 2% for high energies. For smaller energies the deviations can be larger due to the fact that statistical fluctuations are more common since very few interactions occur. In all cases, the deviations are smaller than one standard deviation.

In conclusion, the results obtained with TOPAS-nBio agree well with those generated using GEANT4-DNA. Apart from a few exceptions, deviations are smaller than 5%. All deviations between TOPAS-nBio and GEANT4-DNA are within one standard uncertainty. Hence, the results show that the implementation of the example simulations in TOPAS-nBio as well as the post-processing of the simulation results using ROOT and Python were successful. In addition, it was illustrated that the results vary significantly depending on the used physics list options.



In general, the implementation of the GEANT4-DNA example applications in TOPAS-nBio was easily achievable. Using the tuple scorer, which stores all information relevant to a track in one output file, the user is given the opportunity to evaluate the particle track in a variety of ways. Additionally, this method has the advantage that aspects can be investigated after the simulation that were not considered before since all tracking information are being stored. In case of evaluating the tracking information after a simulation, it must be considered that knowledge of other evaluation programs, in our case ROOT and Python, is required. The implementation of the examples was possible in TOPAS because the user is given the possibility to write own extensions in order to be able to use the entire capacity of GEANT4. In our case, extensions, which are already inserted in TOPAS, could be used as a template, which facilitated the writing of own extensions. In most cases, even just two or three lines had to be edited in the extension files. Probably more complicated extensions could have been written, e.g. to reduce the amount of data or to avoid carrying out a calculation after the simulation, but our goal was to use the simplicity of TOPAS and avoid writing complicated scripts. The amount of data in our simulations was very high because we used the tuple scorer storing all track information. This implies that the more particles are simulated and the more they interact, the larger the file becomes. For example, having a look at the *dnaphysics* example, the file size for one run using *G4EmDNAPhysics_opt2* is around 500 MB. In this file, all tracking information of the 100 primary particles and all particles of further generations are stored



step-by-step. If the physics list *G4EmDNAPhysics_opt4* or *G4EmDNAPhysics_opt6* of the same simulation is used, the output file is smaller, since all in all less interactions occurred (see figure 1).

Altogether, our approach to simulate the examples in TOPAS is simple enough for getting started, however, we recommend to write own extensions according to the quantities, if it is desired to make use of them more frequently.

3.2. Extended simulations regarding the processes of low-energy electrons

In figure 5(a) the frequency of each process in relation to the initial particle energy is illustrated. The most common process for all energies is elastic scattering followed by vibrational excitation. In general, the number of those processes increases with the initial energy, due to the increasing range of the particles noting that in figure 5(a) the y-axis is plotted logarithmically. Both, elastic scattering and vibrational excitation, show a minimal occurrence at an energy of ~ 18 eV. Above an energy of 11 eV, the probability of ionization increases since more ionization energy thresholds are exceeded and the related cross sections also increase (Incerti *et al* 2010b, Bordage *et al* 2016). The energy thresholds required for an ionization as well as for an electronic or vibrational excitation are listed in table 4. These processes reduce the range and hence the amount of elastic

Table 4. Deposited energies in eV by vibrational excitation, electronic excitation and ionization found in our simulations. These energies correspond to the energy thresholds of the associated processes (E_T^{vib} for vibrational excitation, E_T^{ex} for excitation, E_T^{ion} for ionization) implemented in the different models. The vibrational modes are included in the Sanche Excitation Model described in the study of Michaud and Sanche (1987). The energy thresholds for electronic excitation are taken from the Emfietzoglou Dielectric Model (Emfietzoglou and Moscovitch 2002) and ionization levels are described by Dingfelder *et al* (1998).

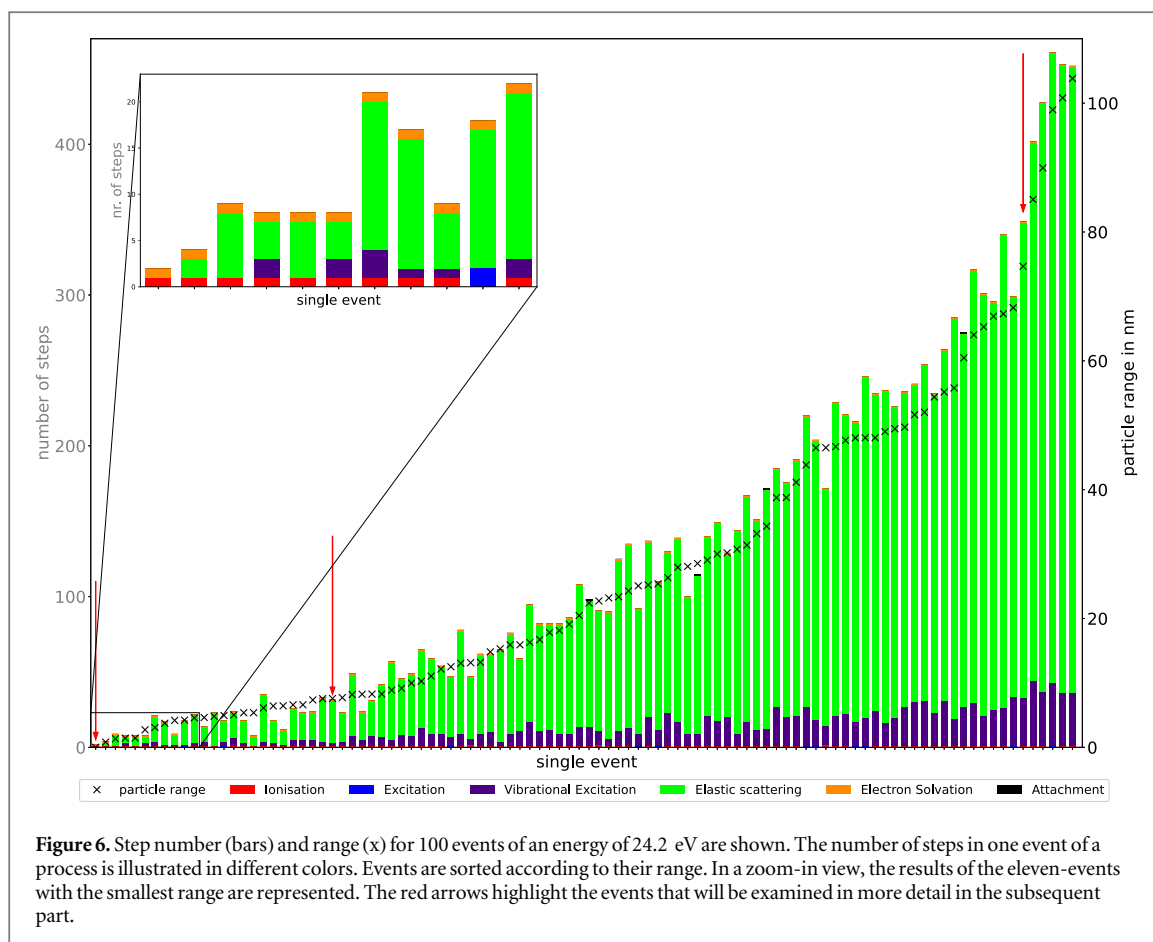
Vib. mode	E_T^{vib}	Electr. excitation level	E_T^{ex}	Molecular orbital	E_T^{ion}
$2(\nu_{1,3})$	0.835	A ¹ B ¹	8.22	1b ₁	10.79
ν_T''	0.024	b ¹ a ¹	10.00	3a ₁	13.39
ν_L'	0.061	Ryd A + B	11.24	1b ₂	16.05
ν_L''	0.092	Ryd C + D	12.61	2a ₁	32.29
ν_2	0.204	Diffuse bands	13.77		
$\nu_{1,3}$	0.417				
ν_3	0.46				
$\nu_{1,3} + \nu_L$	0.5				
ν_T'	0.01				

interactions significantly due to a noticeable energy loss. The number of elastic interactions fluctuate further with increasing initial energy because on the one hand, starting with a higher initial energy more interactions, i.e. also usually a greater range, are possible which results in a higher number of elastic interactions. On the other hand, the kinetic energy of the particle and thus the range is reduced since with increasing initial energy more thresholds for inelastic interactions are exceeded and a higher number of inelastic interactions might occur in one event. The electron solvation process operates as a tracking cut because no chemical interactions are taken into account in any simulations. Since secondary particles were also considered in this simulation, more than 100 electron solvations can take place in each simulation with 100 primary particles as with increasing initial energy more secondary particles are being produced. The tracking of those produced electrons is again terminated by this process.

In figure 5(b) the average deposited energy in one single inelastic interaction is shown as a function of the initial energy separately for each process. For most of the processes, the mean deposited energy remains almost constant over the whole energy range as a consequence of the corresponding energy thresholds (see table 4). The latter is also observed for ionization, which has the highest mean deposited energy in this energy range. Only for electron solvation an energy-dependent mean deposited energy can be observed. The amount of the energy deposition by this process depends on the kinetic energy, which remains after an inelastic interaction if the threshold of 7.4 eV is reached. Since at low energies, only a few eV are left after an ionization or excitation, the mean deposited energy by electron solvation is very small. In figure 5(c), the mean energy deposited in total per primary particle is shown as a function of the initial energy for each process. Those profiles result from the combination of the frequency of each electron process (figure 5(a)) and the corresponding mean deposited energy (figure 5(b)). Altogether, it can be seen that ionization constitutes the largest amount of deposited energy in this energy range.

Figure 5(d) shows the maximum deposited energies for each process as a function of the initial energy. The steps in the line of ionization and excitation visualize the initial energy needed to reach the different thresholds of these processes. The deposited energy always corresponds exactly to the energy thresholds listed in table 4, since the deposited energy in TOPAS-nBio refers to the locally deposited energy, not the kinetic energy loss of the particles. This becomes especially apparent for ionization because the energy thresholds in this case vary the most. Electron solvation results in a maximum deposited energy of 7.4 eV, since this is the tracking cut applied in *G4EmDNAPhysics_opt2*.

To further examine the interactions of low-energy electrons, the frequency and sequence of different processes were investigated for electrons with an initial energy of 24.2 eV. In figure 6, the number of steps is illustrated as bars with different colors for each process for electrons with an initial energy of 24.2 eV for 100 single events. On a second y -axis, the corresponding range of the electrons is plotted. An electron energy of 24.2 eV was chosen because, on the one hand, particles with this initial energy have sufficient kinetic energy so that all processes occur, and on the other hand, not too many inelastic interactions take place. In figure 6, it can be seen that the more steps occur per event, the larger the range and the more elastic scattering and vibrational excitation takes place. Furthermore, it is noticeable that when two ionizations or excitations appear in one event, the number of steps and the range are small, as it can be observed exemplarily in the zoom-in view. In a further step, the sequence of the processes and the deposition of the energy of individual events were examined. In figure 7, the order of the occurring processes of three different events, which are marked with a red arrow in figure 6, is shown. In this representation, the processes are illustrated as consecutive bars, filled with a different color for each process, and plotted against their corresponding step number on the x -axis. The width of the bars

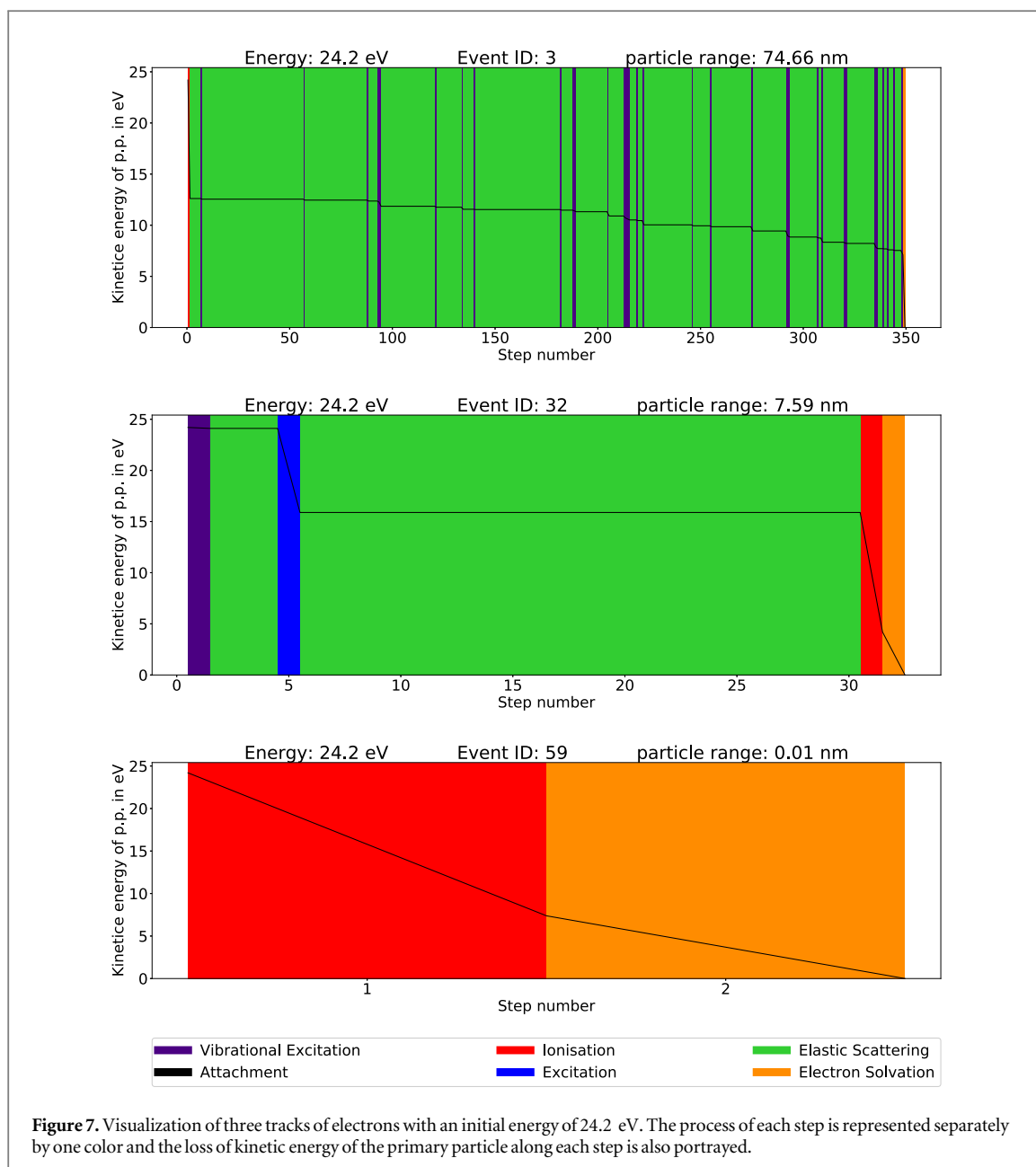


has no further meaning, it only gets smaller the more steps occur in the track. Additionally, the loss of kinetic energy along the steps is shown in each graph.

Beginning with the track of Event ID 3, the track starts with an ionization, for which reason the particle already loses quite a lot of its kinetic energy. After that, a kinetic energy of only roughly 12 eV is left. This process is followed by a number of elastic interactions alternating with vibrational excitations. The vibrational excitations cause the particle to lose a tiny fraction of its kinetic energy until it reaches the tracking cut of 7.4 eV. The track is then terminated with electron solvation, whereby the remaining kinetic energy is deposited locally. In event 32, the number of steps is significantly smaller and fewer elastic interactions and vibrational excitations are present. However, two additional inelastic processes, ionization and excitation, occur for this purpose through which the particle loses a lot of kinetic energy simultaneously. It is also typical for particles in this energy regime that if there are two inelastic interactions (except of vibrational excitations) in one event, the second one occurs at the end of the track. In this case, the remaining kinetic energy is smaller than the tracking cut, which means that the energy is deposited locally by electron solvation as a last step of the track.

In addition to these two characteristic histories of a particle with an initial energy of 24.2 eV, in Event ID 59, the particle reaches the tracking cut already after having conducted only one step. Such a scenario is only possible if ionization occurs as the first process and such a large amount of energy is transferred to the secondary particle that the residual energy of the primary particle is smaller than the tracking cut. Since in most cases only small fractions of kinetic energy are transferred to secondary particles, this kind of track is rather unlikely.

In conclusion, the simulations regarding electrons of energies between 10 and 60 eV showed that the most frequent process is elastic scattering, while the largest amount of energy is deposited by ionization. Thus, the selection of the correct model for ionization is very important for simulations on molecular levels and for DNA damage studies, and should therefore be well considered. The models vary with the different physics lists and can also be selected independently in TOPAS using TsEmDNAPhysics. The model of the processes could not be validated yet due to the absence of experimental data below 1 keV. However, this investigation should give an insight of how damage on molecular levels and DNA is produced. Especially, when further simulations are made with these models to determine, for example, the distribution and amount of SSB and DSB in relation to the effect of radiation at biological levels.



4. Conclusion

Examples pre-programmed in GEANT4, addressing the possibilities of GEANT4-DNA, were coded and re-simulated in TOPAS-nBio to check the feasibility and handling of the toolkit TOPAS. The tuple scorer can be used for further post-processing the tracking information in order to calculate corresponding variables or to carry out detailed investigations of the particle track. A comparison of the original results with GEANT4-DNA showed that the implementation of the GEANT4-DNA example applications in TOPAS-nBio was successful, as deviations in the results of the examples were less than 5.6% in most cases. Furthermore, no significant deviations could be observed. In TOPAS, not always the latest version of GEANT4 is available. However, running the simulations with TOPAS based on GEANT4 version 10.05 shows no significant differences in comparison to simulations performed with GEANT4 version 10.07. The extended simulations provided an insight into the step-by-step interactions of electrons with initial energies between 10 and 60 eV. Using the tuple scorer, it could be shown that in this energy range, the largest part of the energy is deposited by ionizations which influences a particle's fate with respect to its range and the frequency of other occurring processes.

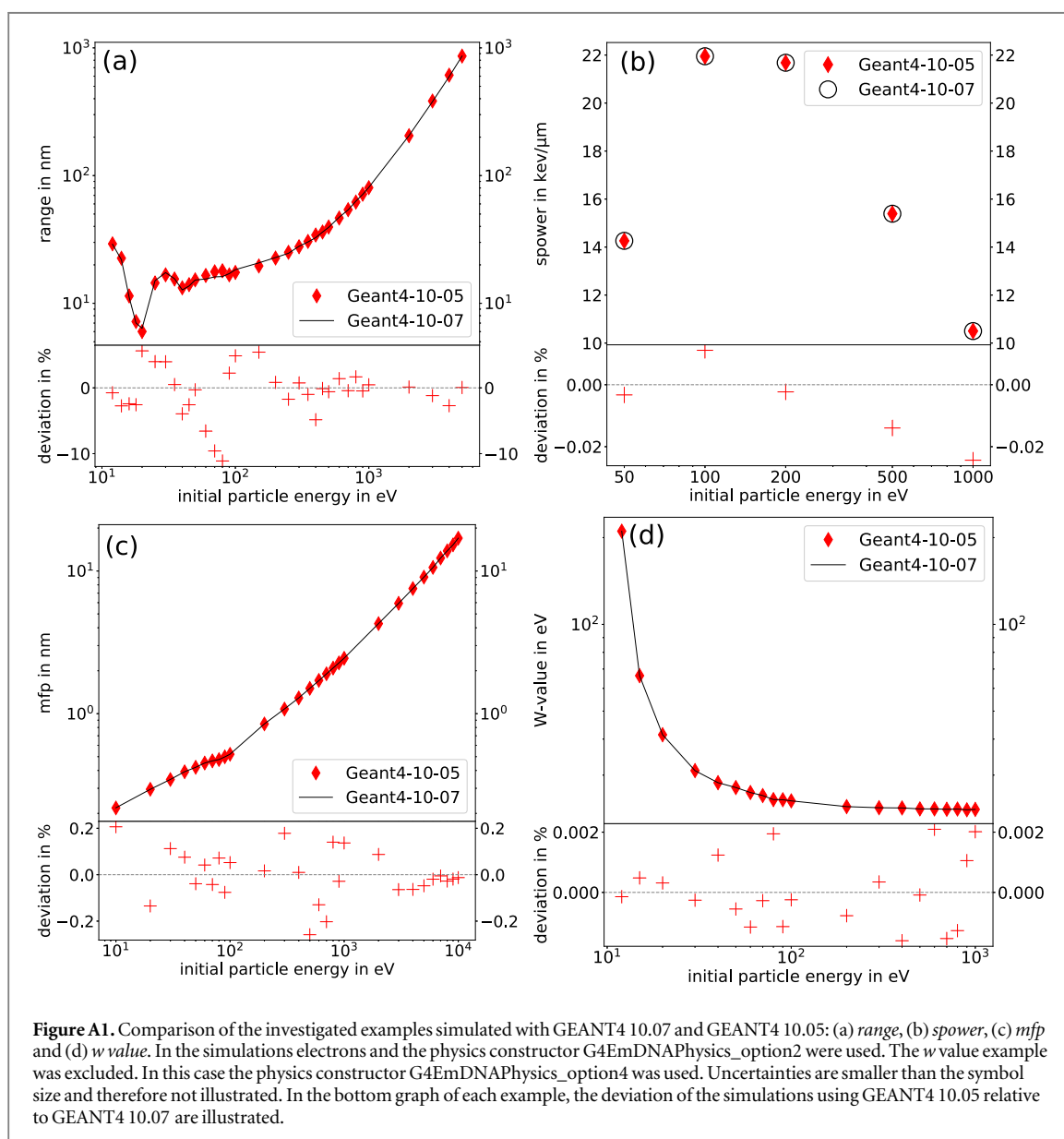
The project was supported by the Federal Ministry of Education and Research within the scope of the grant 'Physikalische Modellierung für die individualisierte Partikel-Strahlentherapie und Magnetresonanztomographie', (MiPS, grant number 13FH726IX6).

Appendix

Although there is no indication in the release note of version 10.06 and 10.07 that the results concerning our simulations would be affected by the update from version 10.05 to version 10.07, we wanted to ensure that the simulations with TOPAS-nBio based on GEANT4 version 10.05, do not lead to significantly different results than with the current GEANT4 version 10.07. Therefore, the examples simulated in GEANT4 10.05 were additionally compared with the simulation results of the current version published on GitHub. For this purpose, the simulations of the example applications were run exactly as they are included in GEANT4 to make sure that all simulation variables are the same. Results could not be compared for all simulations as described in table 1 since only a selection of calculated data is available on GitHub. The *dnaphysics* example could not be compared with our GEANT4-DNA results since the data are not available on GitHub (probably due to the large amount of data).

As it can be seen in figure A1, the results of both different GEANT4 versions agree well for all simulated examples. In the range simulation, deviations are generally smaller than 5%, except of some individually cases. Considering all other examples, deviations are well below 1%. All deviations are distributed around 0 which proves that these are of statistical nature and not of a systematic deviation.

In conclusion, this comparison of the two software versions confirmed that no parameters in the physics lists concerning these simulations changed due to the update. Therefore, there is no disadvantage in simulating the examples for a more detailed comparison with TOPAS3.2 based on GEANT410.05.



ORCID iDs

Tabea Pfuhl  <https://orcid.org/0000-0002-9430-2872>

Klemens Zink  <https://orcid.org/0000-0001-5785-4101>

Kilian-Simon Baumann  <https://orcid.org/0000-0003-1223-523X>

References

- Agostinelli S *et al* 2003 Geant4—a simulation toolkit *Nucl. Instrum. Methods Phys. Res. A* **506** 250–303
- Allison J *et al* 2006 Geant4 developments and applications *IEEE Trans. Nucl. Sci.* **53** 270–8
- Bordage M, Bordes J, Edel S, Terrissol M, Franceries X, Bardi's M, Lampe N and Incerti S 2016 Implementation of new physics models for low energy electrons in liquid water in Geant4-DNA *Physica Med.* **32** 1833–40
- Brun R and Rademakers F 1997 ROOT—an object oriented data analysis framework *Nucl. Instrum. Methods Phys. Res. A* **389** 81–6
- Denifl S, Märk T and Scheier P 2012 The Role of Secondary Electrons in Radiation Damage *Radiation Damage in Biomolecular Systems* (Dordrecht: Springer Netherlands) 45–58
- Dingfelder M, Hantke D, Inokuti M and Paretzke H G 1998 Electron inelastic-scattering cross sections in liquid water *Radiat. Phys. Chem.* **53** 1–18
- Emfietzoglou D and Moscovitch M 2002 Inelastic collision characteristics of electrons in liquid water *Nucl. Instrum. Methods Phys. Res. B* **193** 71–8
- Faddegon B, Ramos-Mendez J, Schuemann J, McNamara A, Shin J, Perl J and Paganetti H 2020 The TOPAS tool for particle simulation, a Monte Carlo simulation tool for physics, biology and clinical research *Phys. Med.* **72** 114–21
- Francis Z, Incerti S, Karamitros M, Tran H N and Villagrasa C 2011 Stopping power and ranges of electrons, protons and alpha particles in liquid water using the Geant4-DNA package *Nucl. Instrum. Methods Phys. Res. B* **269** 2307–11
- Hahn M B and Villate J M Z 2021 Combined cell and nanoparticle models for TOPAS to study radiation dose enhancement in cell organelles *Sci. Rep.* **11** 1–10
- ICRU 2016 Key data for ionizing radiation dosimetry: measurement standards and applications *ICRU Report No. 90* (<https://doi.org/10.1093/jicru/ndw040>)
- Incerti S *et al* 2010a The Geant4-DNA project the Geant4-DNA collaboration *Int. J. Model. Simul. Sci. Comput.* **1** 157–78
- Incerti S *et al* 2010b Comparison of GEANT4 very low energy cross section models with experimental data in water *Med. Phys.* **37** 4692–708
- Incerti S *et al* 2018 Geant4-DNA example applications for track structure simulations in liquid water: a report from the Geant4-DNA Project *Med. Phys.* **45** e722–39
- Karamitros M *et al* 2011 Modeling radiation chemistry in the Geant4 toolkit *Prog. Nucl. Sci. Technol.* **2** 503–8
- Kyriakou I, Incerti S and Francis Z 2015 Technical note: improvements in geant4 energy-loss model and the effect on low-energy electron transport in liquid water *Med. Phys.* **42** 3870–6
- McMahon S J, Schuemann J, Paganetti H and Prise K M 2016 Mechanistic modelling of DNA repair and cellular survival following radiation-induced DNA damage *Sci. Rep.* **6** 1–14
- McNamara A, Geng C, Turner R, Mendez J R, Perl J, Held K, Faddegon B, Paganetti H and Schuemann J 2017 Validation of the radiobiology toolkit TOPAS-nBio in simple DNA geometries *Phys. Med.* **33** 207–15
- McNamara A L *et al* 2018 Geometrical structures for radiation biology research as implemented in the TOPAS-nBio toolkit *Phys. Med. Biol.* **63** 1–19
- Melton C E 1972 Cross sections and interpretation of dissociative attachment reactions producing OH, O, and H in H₂O *J. Chem. Phys.* **57** 4218–25
- Michaud M and Sanche L 1987 Absolute vibrational excitation cross sections for slow-electron (1–18 eV) scattering in solid H₂O *Phys. Rev. A* **36** 4684–99
- Michaud M, Wen A and Sanche L 2003 Cross sections for low-energy (1–100 eV) electron elastic and inelastic scattering in amorphous ice *Radiat. Res.* **159** 3–22
- Perl J, Shin J, Schümann J, Faddegon B and Paganetti H 2012 TOPAS: an innovative proton Monte Carlo platform for research and clinical applications *Med. Phys.* **39** 6818–37
- Pimblott S M and LaVerne J A 2007 Production of low-energy electrons by ionizing radiation *Radiat. Phys. Chem.* **76** 1244–7
- Rogers D W 2006 Fifty years of Monte Carlo simulations for medical physics *Phys. Med. Biol.* **51**
- Sanche L 2012 Nanoscale Dynamics of Radiosensitivity: Role of Low Energy Electrons *Radiation Damage in Biomolecular Systems* (Dordrecht: Springer Netherlands) 3–43
- Schuemann J, McNamara A L, Ramos-Méndez J, Perl J, Held K D, Paganetti H, Incerti S and Faddegon B 2019 TOPAS-nBio: an extension to the TOPAS simulation toolkit for cellular and sub-cellular radiobiology *Radiat. Res.* **191** 125–38
- Tajik-Mansoury M, Rajabi H and Mozdarani H 2017 A comparison between track-structure, condensed-history Monte Carlo simulations and MIRD cellular S-values *Phys. Med. Biol.* **62** N90–N106
- Testa M, Schuemann J, Lu H-M, Shin J, Faddegon B, Perl J and Paganetti H 2013 Experimental validation of the TOPAS Monte Carlo system for passive scattering proton therapy *Med. Phys.* **40** 1–16
- Warmenhoven J W, Henthorn N T, Ingram S P, Chadwick A L, Sotiropoulos M, Korabel N, Fedotov S, Mackay R I, Kirkby K J and Merchant M J 2020 Insights into the non-homologous end joining pathway and double strand break end mobility provided by mechanistic in silico modelling *DNA Repair* **85** 102743
- Zhu H *et al* 2019 The microdosimetric extension in TOPAS: development and comparison with published data *Phys. Med. Biol.* **64** 145004
- Zhu H *et al* 2020 A parameter sensitivity study for simulating DNA damage after proton irradiation using TOPAS-nBio *Phys. Med. Biol.* **65** 085015



PAPER

OPEN ACCESS

RECEIVED
11 January 2023REVISED
23 May 2023ACCEPTED FOR PUBLICATION
7 June 2023PUBLISHED
30 June 2023

Original content from this work may be used under the terms of the [Creative Commons Attribution 4.0 licence](#).

Any further distribution of this work must maintain attribution to the author(s) and the title of the work, journal citation and DOI.



A method to implement inter-track interactions in Monte Carlo simulations with TOPAS-nBio and their influence on simulated radical yields following water radiolysis

Larissa Derksen¹, Veronika Flatten² , Rita Engenhardt-Cabillic^{2,3}, Klemens Zink^{1,2,3} and Kilian-Simon Baumann^{1,2,3}

¹ University of Applied Sciences, Institute of Medical Physics and Radiation Protection, Giessen, Germany

² University Medical Center Giessen-Marburg, Department of Radiotherapy and Radiooncology, Marburg, Germany

³ Marburg Ion-Beam Therapy Center (MIT), Marburg, Germany

E-mail: larissa.derksen@biotecmed.thm.de

Keywords: Monte Carlo simulation, GEANT4-DNA, TOPAS-nBio, inter-track interaction, radiolysis, radiation chemistry, FLASH radiotherapy

Abstract

Objective. In FLASH radiotherapy (dose rates $\geq 40 \text{ Gy s}^{-1}$), a reduced normal tissue toxicity has been observed, while maintaining the same tumor control compared to conventional radiotherapy (dose rates $\leq 0.03 \text{ Gy s}^{-1}$). This protecting effect could not be fully explained yet. One assumption is that interactions between the chemicals of different primary ionizing particles, so-called inter-track interactions, trigger this outcome. In this work, we included inter-track interactions in Monte Carlo track structure simulations and investigated the yield of chemicals (G -value) produced by ionizing particles. **Approach.** For the simulations, we used the Monte Carlo toolkit TOPAS, in which inter-track interactions cannot be implemented without further effort. Thus, we developed a method enabling the simultaneous simulation of N original histories in one event allowing chemical species to interact with each other. To investigate the effect of inter-track interactions we analyzed the G -value of different chemicals using various radiation sources. We used electrons with an energy of 60 eV in different spatial arrangements as well as a 10 MeV and 100 MeV proton source. For electrons we set N between 1 and 60, for protons between 1 and 100. **Main results.** In all simulations, the total G -value decreases with increasing N . In detail, the G -value for $\cdot\text{OH}$, H_3O and e_{aq} decreases with increasing N , whereas the G -value of OH^- , H_2O_2 and H_2 increases slightly. The reason is that with increasing N , the concentration of chemical radicals increases allowing for more chemical reactions between the radicals resulting in a change of the dynamics of the chemical stage. **Significance.** Inter-track interactions resulting in a variation of the yield of chemical species, may be a factor explaining the FLASH effect. To verify this hypothesis, further simulations are necessary in order to evaluate the impact of varying G -values on the yield of DNA damages.

1. Introduction

In radiotherapy (RT), a permanent compromise has to be found between the greatest tumor control and the least toxicity to the surrounding normal tissue. To best achieve both, techniques in the areas of imaging, dosimetry, and radiation delivery are constantly developing. For example, these innovations include intensity-modulated radiation therapy (IMRT) (Group *et al* 2001), volumetric modulated arc therapy (VMAT) (Otto 2008) and proton therapy (Wilson 1946, Mohan and Grosshans 2017). Currently, a new and promising irradiation technique, the so-called FLASH-RT, is attracting much attention (Gao *et al* 2022).

Using FLASH-RT, ultra-high dose rates above 40 Gy s^{-1} (Favaudon *et al* 2014) are applied delivering a high dose in very short pulses. In comparison to radiotherapy using conventional dose rates of $\leq 0.03 \text{ Gy s}^{-1}$, FLASH-RT dose rates can be higher by a factor of 1000. The most important effect of FLASH-RT is a reduced normal

tissue toxicity whereas the tumor control is maintained compared to conventional RT (see for example Favaudon *et al* (2014), Montay-Gruel *et al* (2019) and Fouillade *et al* (2020)). Even though this radiation technique is currently not implemented in the clinical routine, there are many ongoing studies investigating the potential effect of these technique clinically (Bourhis *et al* 2019, Mascia *et al* 2023), experimentally (Buonanno *et al* 2019, Jansen *et al* 2021, Small *et al* 2021) or by performing simulations (Ramos-Méndez *et al* 2020, Boscolo *et al* 2021, Lai *et al* 2021). Detailed summaries about the studies can be found in several FLASH related reviews, e.g. Wilson *et al* (2020), Kim *et al* (2021), Kacem *et al* (2021) and Zhou (2020).

Although in most studies an increase of normal tissue protection was found, in some other studies this effect could not be observed indicating limitations of the FLASH effect as for example seen by Venkatesulu *et al* (2019). These limitations show that not only the dose rate is essential, but also other parameters like pulse duration, number of pulses and dose per pulse are crucial factors (Ruan *et al* 2021) and need to be further investigated.

In addition, more investigations are needed to determine to underlying causes of the FLASH effect since the reason for the observed normal tissue-sparing effect in many FLASH related experimental studies remains unclear. One assumption is that so-called *inter-track interactions*, that means reactions between the chemicals of different primary particle tracks, partly contribute to this effect. Kreipl *et al* (2009) investigated radical-radical interactions of two different primary particle tracks using Monte Carlo simulations with protons, which had an effect on the yield of chemical radicals, but did not find significant changes in the DNA damage yield. Furthermore, Ramos-Méndez *et al* (2020) observed an LET-dependent yield of chemical radicals by simulating inter-track interactions in TOPAS-nBio, which means that chemical species produced by different primary particles can react with each other. In their work, they used the independent reaction time method for simulations of the chemical stage. Alanazi *et al* (2021) investigated inter-track interactions of 300 MeV proton tracks and detected differences in the radical yield beyond 1 ns after irradiation in dependence of different dose rates.

The main goal of our research was first, to provide a method implementing inter-track interactions in TOPAS-nBio using the step-by-step method for chemistry simulations and second, to perform a fundamental and detailed investigation of the impact of these inter-track interactions in the chemical stage following water radiolysis. Especially, this stage after irradiation is important to analyze since it is the first stage after the physical interactions. Even changes at these early points in time after irradiation can have an impact on later stages and are therefore important to investigate.

In the chemical stage, using conventional dose rates, inter-track interactions are highly improbable. The reason for this is that the duration of the chemical stage of 1 μ s of one primary particle is significantly shorter than the time lapse between the generation of two primary particles which could be shown through exemplary calculations by Lai *et al* (2021). However, the time lapse becomes shorter when considering ultra-high dose rates used in FLASH-RT and the chemical stages of different primary particles can overlap. In this case, inter-track interactions may occur. However, the spatial and temporal separation of the tracks are crucial factors allowing the chemical species of different tracks to react with each other. With regard to FLASH-RT, Monte Carlo based track structure investigations of the potential of inter-track interactions showed contradictory results. Whereas Thompson *et al* (2023) concludes that inter-track interactions do not occur at ultra-high dose rates, the calculations of Lai *et al* (2021) and Baikalov *et al* (2022) show the opposite. Since this illustrates that there are many factors influencing the potential of inter-track interactions, we initially analyzed the effect of inter-track interactions on their own. In this way, we create a basic understanding of how inter-track interactions affect chemical dynamics before considering them in more complex systems. Contrary to other simulation studies, we systematically increased the number of inter-track interactions in our simulations to investigate their influence on the amount of chemicals during the chemical stage. Another characteristic is that the particles are simulated at the same time. This is comparable to pulse width in the picosecond regime which are used, for instance, at the R&D platform *FLASHlab@PITZ* to perform experimental measurements (Stephan *et al* 2022). The effects of inter-track interactions were studied by determining the yield of chemical species during and at the end of the chemical stage using electron and proton sources with different LET. Since chemical species, in particular hydroxyl (\cdot OH), can cause indirect DNA damages, inter-track interactions may have an effect on the biological outcome using FLASH-RT.

2. Materials and methods

2.1. Monte Carlo track structure simulations

We used TOPAS-nBio version 1.0 (Schuermann *et al* 2019) with TOPAS version 3.7 (Perl *et al* 2012, Faddegon *et al* 2020) to perform Monte Carlo track structure simulations based on the open access Monte Carlo Code GEANT4/GEANT4-DNA version 10.05.p01 (Agostinelli *et al* 2003, Allison *et al* 2006, Incerti *et al* 2010a). Based on GEANT4, TOPAS applies the same physics modules and cross section data as in the natural GEANT4 code.

However, in the toolkit TOPAS various simulation configurations are already predefined, which can be accessed via simple text-based commands. This way, the toolkit enables the application of the Monte Carlo Code even for users without advanced programming skills or experience. TOPAS has already been well-validated against experimental data (Perl *et al* 2012, Testa *et al* 2013).

While TOPAS was initially designed for simulations at the macroscopic scale, the extension TOPAS-nBio allows simulations on the nanoscopic scale since particles are tracked step-by-step down to kinetic energies of some eV.⁴ Thus, the radiation effect can be studied at cellular and sub-cellular levels. In this study, the interactions of primary particles as well as chemical radicals and species in the vicinity of the DNA are of particular interest as this is the key component of radiobiological effects. For radiobiological simulations, a variety of biological structures such as different DNA models, cell nuclei and cell models are included in TOPAS-nBio. McNamara *et al* (2018) have published a detailed description of these geometries. Along with these predefined geometry components, TOPAS provides several scorers for classifying the DNA damage by e.g. single strand breaks (SSB) and double strand breaks (DSB).

In addition to the extended physics and geometrical features, chemical interactions of the radiolysis products can be simulated (Karamitros *et al* 2011). Thus, the indirect damaging of the DNA can be investigated. An even more accurate simulation of the expected biological response can be achieved by combining DNA repair models with the simulation. Currently, two different mechanistic repair models can be applied for modeling biological end points like cell survival curves in conjunction with the track structure simulations performed with TOPAS-nBio (McMahon *et al* 2016, Warmenhoven *et al* 2020).

In previous studies, validation of TOPAS-nBio was performed and the radiobiology extension of TOPAS has been proven to be an accurate, well performing Monte Carlo tool regarding radiolysis and DNA damage simulations. McNamara *et al* (2017) showed a good agreement of simulated yields of direct SSB and DSB on simple DNA models with other simulation results and experimental data. Ramos-Méndez *et al* (2018) performed chemistry simulations and compared the resulting yields of chemical products following water radiolysis with other Monte Carlo simulation results and experimental data. Furthermore, TOPAS-nBio was used in several studies to simulate the DNA damage induced by ionizing radiation (Zhu *et al* 2020a, 2020b, Ramos-Méndez *et al* 2021). Another application of the toolkit are investigations of irradiation including gold nanoparticles for dose enhancement (Rudek *et al* 2019, Hahn and Villate 2021, Klapproth *et al* 2021). Moreover, the radiobiology effect of gadolinium dose enhancement in neutron capture therapy was studied using TOPAS-nBio by Van Delinder *et al* (2021).

2.2. Generation of inter-track interactions in TOPAS-nBio

The purpose of this study was to examine the yield of chemicals, the so called G -value, in dependence of inter-track interaction. According to Karamitros *et al* (2011), the G -value G is defined as the total number $N(t)$ of chemicals at a given time t produced or consumed per 100 eV of total deposited energy E in an irradiated system:

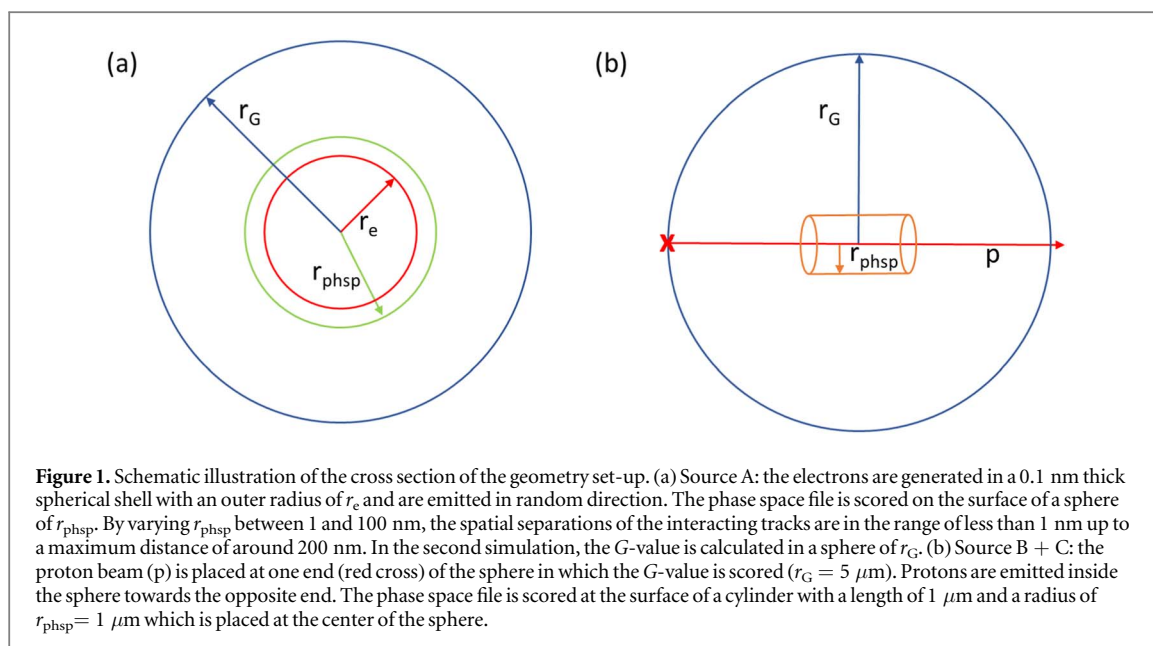
$$G = \frac{N(t) \cdot 100}{E \text{ (eV)}}. \quad (1)$$

Since, per default, it is not possible to model inter-track interactions TOPAS-nBio, we first developed an approach for modeling inter-track interactions using this Monte Carlo toolkit.

In general, in TOPAS-nBio the radiation effect, i.e. the physical and chemical stage, of one primary particle, or more precisely of one history, is simulated in one event after each other and independently from each other. That means, at the chemical stage, reactions between the chemical species produced by the same primary particle and its secondary particles are taken into account. However, no chemical reactions between chemicals produced in two or more different events (i.e. primary particles) can be considered, so that inter-track interactions are by default not possible in TOPAS-nBio. In order to enable inter-track interactions using TOPAS-nBio, we benefited from the fact that TOPAS-nBio is able to simulate the reactions between chemical species produced by the same primary particle and its secondary particles, i.e. all chemicals with the same event number. That means to allow inter-track interactions of chemicals produced by N primary particles and its secondaries, we simulated N original histories in one event. This way the radiation effect of each history is not simulated one after the other as per default but N histories are simulated simultaneously. By varying the number N of histories simulated simultaneously in one event, we could directly handle a factor proportional to the particle fluence and dose rate. In brief, in order to realize the simulation of N histories in one event in TOPAS, we scored a phase space file of the source and modified. A more detailed description of the implementation of our method in TOPAS is given in appendix A.

All in all, to perform simulations in TOPAS-nBio with inter-track interactions according to our approach, we followed these three steps:

⁴The default tracking cuts for electrons are between 7.4 eV and 11 eV depending on the applied physics list (Incerti *et al* 2018).



1. Scoring a phase space file of the original primary particle source.
2. Modification of the phase space file so that N histories are simulated simultaneously in one event.
3. Using the modified phase space file in further simulations to investigate water radiolysis and inter-track interactions by examining the yield of chemical radicals.

2.3. Simulation setup

We applied our approach for realizing inter-track interactions to three different particle sources, which are characterized in the following subsections. First, we investigated the effect of inter-track interactions in detail using a simple source of electrons of low energy (60 eV). With these simulations, we aim to obtain fundamental and basic understanding of the impact of inter-track interactions on the chemical stage of radiobiological simulations. Using this low energy, we compromised between simulation time and detailed track information for analysis. Second, once the basic impacts are identified, we applied our approach on proton beams of two different, higher energies (10 and 100 MeV).

All simulations were performed in *G4_WATER*, which has a density of 1 g cm^{-3} and a mean ionization potential of 78 eV. Reference simulations, in which no inter-track interactions take place, were performed without modifying the phase space file.

2.3.1. Particle source a: electron source

In the first simulation scoring the phase space file to enable inter-track interactions, 60 primary electrons with an energy of 60 eV were generated using a volumetric source in TOPAS. This energy was chosen since on the one hand it is the mean energy produced by primary ions of clinically relevant energies (Pimblott and LaVerne 2007) and on the other hand simulation times are acceptable, due to less chemical species produced by only a few inelastic interactions. The last point is particularly crucial, since with increasing N , simulation times grow due to a larger amount of chemical species that interact via diffusion controlled reactions with each other. In figure 1(a), a schematic illustration of the geometry set-up using electrons is depicted. The electrons are emitted in a spherical shell with a thickness of 0.1 nm (reason explained below) and an outer radius r_e . In a distance of 0.1 nm from this spherical shell, the phase space file is scored on the outer curved surface of a sphere with radius $r_{\text{phsp}} = r_e + 0.1 \text{ nm}$.

In order to investigate the influence of inter-track interactions on both the time component, here realized by different N , and the spatial component, we set r_{phsp} to the following different values: $r_{\text{phsp}} = 1, 10, 20, 30, 40, 50, 75, 100 \text{ nm}$. Since the electron density and hence the density of chemical species gets influenced by the source geometry, we expected a change of the G-value due to different r_{phsp} . To ensure inter-track interactions, we started with the densest arrangement of electrons and then systematically decreased it. When scoring electrons at r_{phsp} , we applied filters to the scorer so that only primary electrons with a kinetic energy of 60 eV at the scorer surface were included in the phase space file. This way, it can be avoided that the electron has already undergone interactions like ionization or excitation resulting in chemical species in the following radiolysis. These molecules would not be included in the subsequent simulation calculating the G-value. Thus, the thickness of

the spherical shell was set to 0.1 nm, which is the smallest geometrical dimension that can be set in TOPAS-nBio. This way it can be avoided in advance that the particles scoring on the phase space surface already undergone inelastic interactions in this geometry component.

After the first simulation, the phase space file was modified in order to enable inter-track interaction of $N = 2, 4, 5, 6, 10, 12, 15, 20, 30, 60$ primary particles. These factors were chosen so that the same total number of 60 primary particles could be simulated in each simulation regardless of N . For example, choosing $N = 2$, chemicals produced by two different primary electrons can interact with each other. For a consistency of presentation, the reference simulations are specified as $N = 1$.

In the second simulation scoring the G -value, this modified phase space file was set as the particle source. The G -value was scored in a sphere with the radius of $r_G = 1 \mu\text{m}$ for all simulation set-ups of r_{phsp} and N . The chosen radius ensures that all electrons and their chemicals are stopped inside this volume.

The simulations were repeated 100 times with different random seeds and final G -values were received by averaging the G -values of these 100 independent simulations.

In brief, with this simulation set-up, we studied the effect of inter-track interactions on the G -value by controlling the density of chemicals the following two ways:

- By varying r_{phsp} , i.e. the geometrical setup, we varied the average distance between the initial electrons.
- By varying N , i.e. varying the setup on the time scale, we varied the number of tracks between which inter-track interactions can occur.

2.3.2. Particle source B + C: proton sources

In first simulations for scoring the phase space file, a proton beam with two different energies was used in separated simulations as a source: 10 MeV (source B) and 100 MeV (source C). In figure 1(b), the geometry setup is shown schematically for both proton beams. For both energies, the particle source was placed at one end of the sphere in which the G -value is scored emitting 100 primary protons inside the sphere towards the opposite end. Around each proton beam, a cylinder with an length of $1 \mu\text{m}$ and a radius of $r_{\text{phsp}} = 1 \text{ nm}$ was positioned at the center of the sphere in order to score all secondary electrons traversing the surface of the cylinder in a phase space file. We chose this setup to reduce simulation times and still be able to investigate the difference between the high (10 MeV) and low LET (100 MeV) sources. Since the number of secondary electrons scored in one event on the cylinder surface varies with the LET, the LET-dependence can be investigated without unfeasible simulation times.

After the first simulation runs, the phase space files were modified in order to calculate inter-track interaction of the secondary electrons of $N = 2, 4, 5, 10, 20, 25, 50, 100$ primary protons.⁵

In the following second simulations, the G -value was calculated in a sphere with radius $r_G = 5 \mu\text{m}$ using the modified phase space files as a particle source. This sphere size was chosen since it corresponds approximately to the size of a cell nucleus.

For statistical reasons, the simulations were performed 10 times with different random seeds⁶ and final G -values were received by averaging the results of the simulations using different random seeds.

2.4. Physics and chemistry modules

In the physical stage, interactions of all primary and secondary particles with the surrounding water molecules were simulated step-by-step using the GEANT4 physics constructor *G4EmDNAPhysics_option2*, which is currently the default setup in TOPAS-nBio. This constructor is in detail described by Incerti et al (2018) with regard to the included physics models and was further investigated in TOPAS-nBio in our previous work (Derksen et al 2021). The following pre-chemical stage, in which the chemical species are generated, was characterized by the branching ratios and dissociation schemes, which are specified by Ramos-Méndez et al (2018) and shown in table 1. Thereby, the placement of all dissociation products is specified for each product and dissociation channel in relation to its inelastic process generating the chemicals (Bernal et al 2015). In the chemical stage, diffusion of the produced chemical species were simulated step-by-step using the Brownian motion. All chemical reactions between the molecules including their reaction rate, which were implemented in GEANT4 by Karamitros et al (2011, 2014) and extended by Ramos-Méndez et al (2018), are shown in table 2. To access these chemistry models, we used the *TsEmDNAChemistryExtended* module in TOPAS-nBio. In table 2, the included reactions of all eleven chemical species considered in the extended chemical list are

⁵ Similar to the electron source, these factors were chosen so that in each simulation the same number of secondary electrons of 100 primary protons was simulated.

⁶ In contrast to the simulations using source A, 10 simulation runs showed sufficient accuracy relative to the significant increased simulation time due to the high amount of secondary electrons and the consequent increase of chemical species.

Table 1. Dissociation schemes implemented in TOPAS-nBio. Adapted from Ramos-Méndez et al 2018. © 2018 Institute of Physics and Engineering in Medicine. All rights reserved.

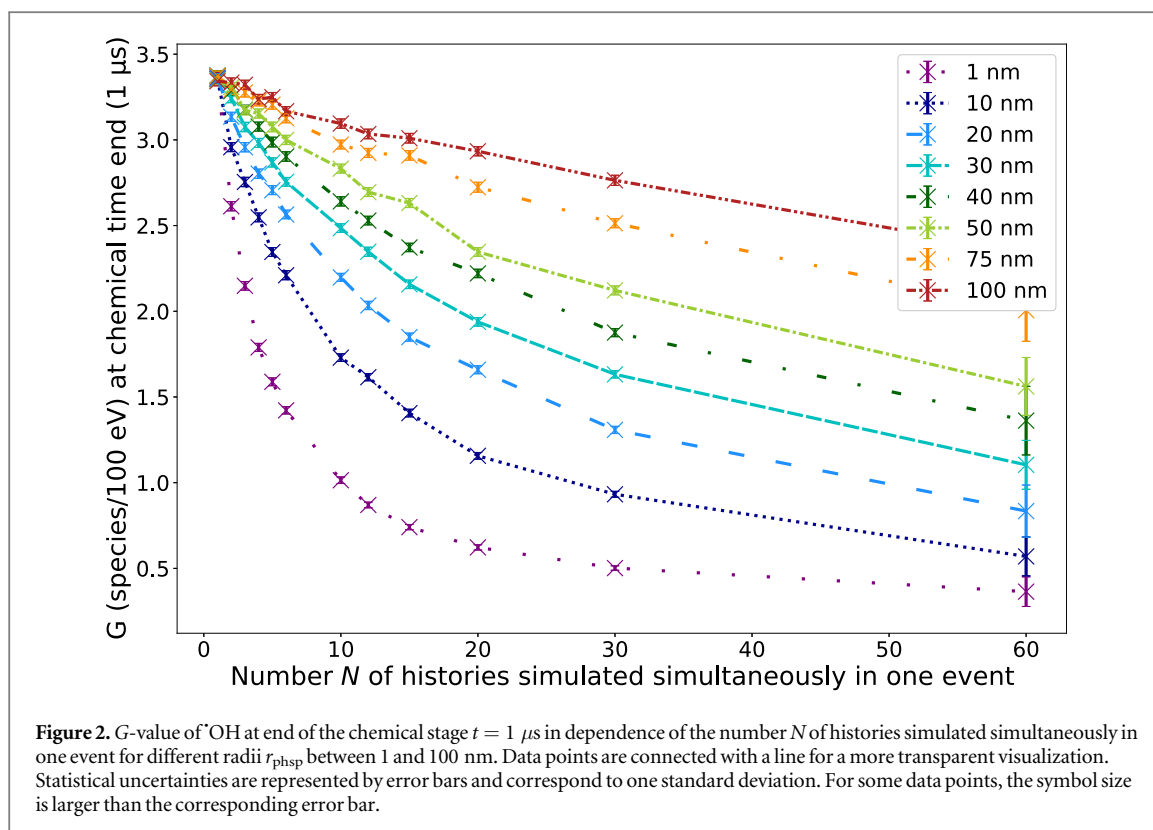
Process		Probability (%)	
Ionization state	Dissociative decay	$H_3O^+ + OH^\cdot$	100
A^1B_1	Dissociative decay	$OH^\cdot + H^\cdot$	65
	Relaxation	$H_2O + \Delta E$	35
B^1A_1	Auto-ionization	$H_3O^+ + \cdot OH + e_{aq}^-$	55
	Auto-ionization	$\cdot OH + \cdot OH + H_2$	15
	Relaxation	$H_2O + \Delta E$	30
Rydberg, diffuse bands	Auto-ionization	$H_3O^+ + \cdot OH + e_{aq}^-$	50
	Relaxation	$H_2O + \Delta E$	50
Dissociative attachment	Dissociative decay	$OH^- + \cdot OH + H_2$	100

Table 2. Chemical reactions and reaction rates k considered in the chemical stage used in the module *TsEmDNACchemistryExtended*. H_2O molecules are not listed in the reaction formulas and no product means that the reaction product is H_2O . In this context, e_{aq}^- describes an electron solvated in water. Moreover, an electron generated in the physical stage with an energy lower than the threshold of physical interactions (here 7.4 eV) is also considered as solvated. This way, its diffusion and reaction is then simulated in the chemical stage.

No.	Reaction	$k (10^{10}/M/s)^b$
1 ^a	$e_{aq}^- + e_{aq}^- \rightarrow 2OH^- + H_2$	0.647
2 ^a	$e_{aq}^- + \cdot OH \rightarrow OH^-$	2.953
3 ^a	$e_{aq}^- + H^\cdot \rightarrow OH^- + H_2$	2.652
4 ^a	$e_{aq}^- + H_3O \rightarrow H^\cdot$	2.109
5	$e_{aq}^- + H_2O_2 \rightarrow OH^- + \cdot OH$	1.405
6 ^a	$\cdot OH + \cdot OH \rightarrow H_2O_2$	0.475
7 ^a	$\cdot OH + H^\cdot \rightarrow$ No product	1.438
8 ^a	$H^\cdot + H^\cdot \rightarrow H_2$	0.503
9 ^a	$H_3O + OH^- \rightarrow$ No product	11.031
10 ^a	$H_2 + \cdot OH \rightarrow H^\cdot$	0.0045
11	$\cdot OH + H_2O_2 \rightarrow HO_2$	0.0023
12	$\cdot OH + HO_2 \rightarrow O_2$	1.0
13	$\cdot OH + O_2 \rightarrow O_2 + OH^-$	0.9
14	$\cdot OH + HO_{-2} \rightarrow HO_2 + OH^-$	0.9
15	$e_{aq}^- + HO_2 \rightarrow HO_{-2}$	2.0
16	$e_{aq}^- + O_2 \rightarrow O_2^-$	1.9
17	$e_{aq}^- + O_2^- \rightarrow OH^- + HO_{-2}$	1.3
18	$H^\cdot + H_2O_2 \rightarrow \cdot OH$	0.01
19	$H^\cdot + HO_2 \rightarrow H_2O_2$	2.0
20	$H^\cdot + O_2 \rightarrow HO_2$	2.0
21 ^a	$H^\cdot + OH^- \rightarrow e_{aq}^-$	0.002
22	$H^\cdot + O_2^- \rightarrow HO_{-2}$	2.0
23	$H_3O + O_2^- \rightarrow HO_2$	3.0
24	$H_3O + HO_{-2} \rightarrow H_2O_2$	2.0
25	$HO_2 + HO_2 \rightarrow H_2O_2 + O_2$	
26	$HO_2 + O_2^- \rightarrow O_2 + HO_{-2}$	0.0085

Notes.^a These reactions can occur directly after the pre-chemical stage.^b $M = 1 \text{ mol dm}^{-3}$.

shown. Even though oxygen is specified as a molecule in table 2, dissolved oxygen is not simulated in our simulations. The time end for chemical interactions was set to 1 μs which is the maximum value in TOPAS-nBio.

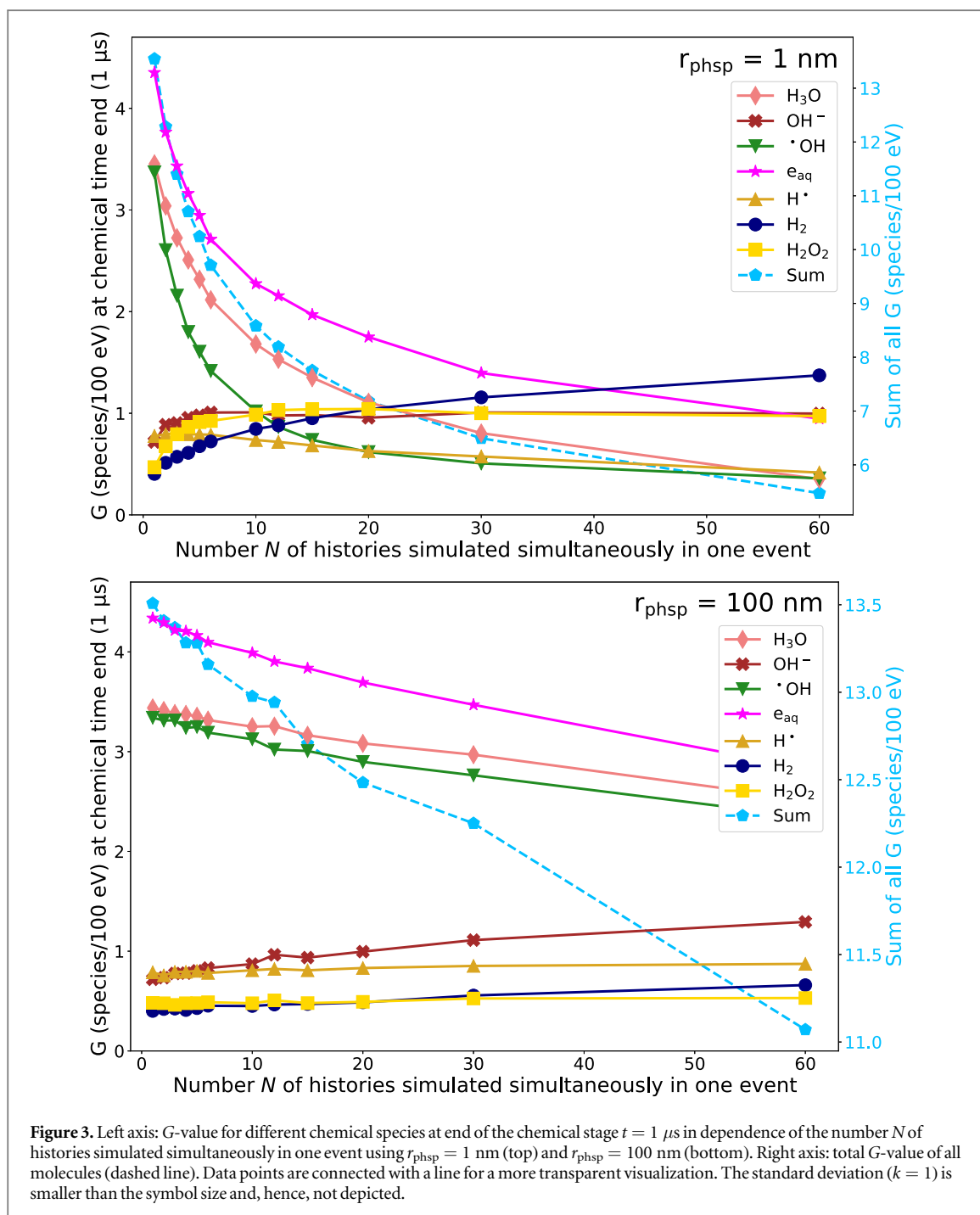


3. Results

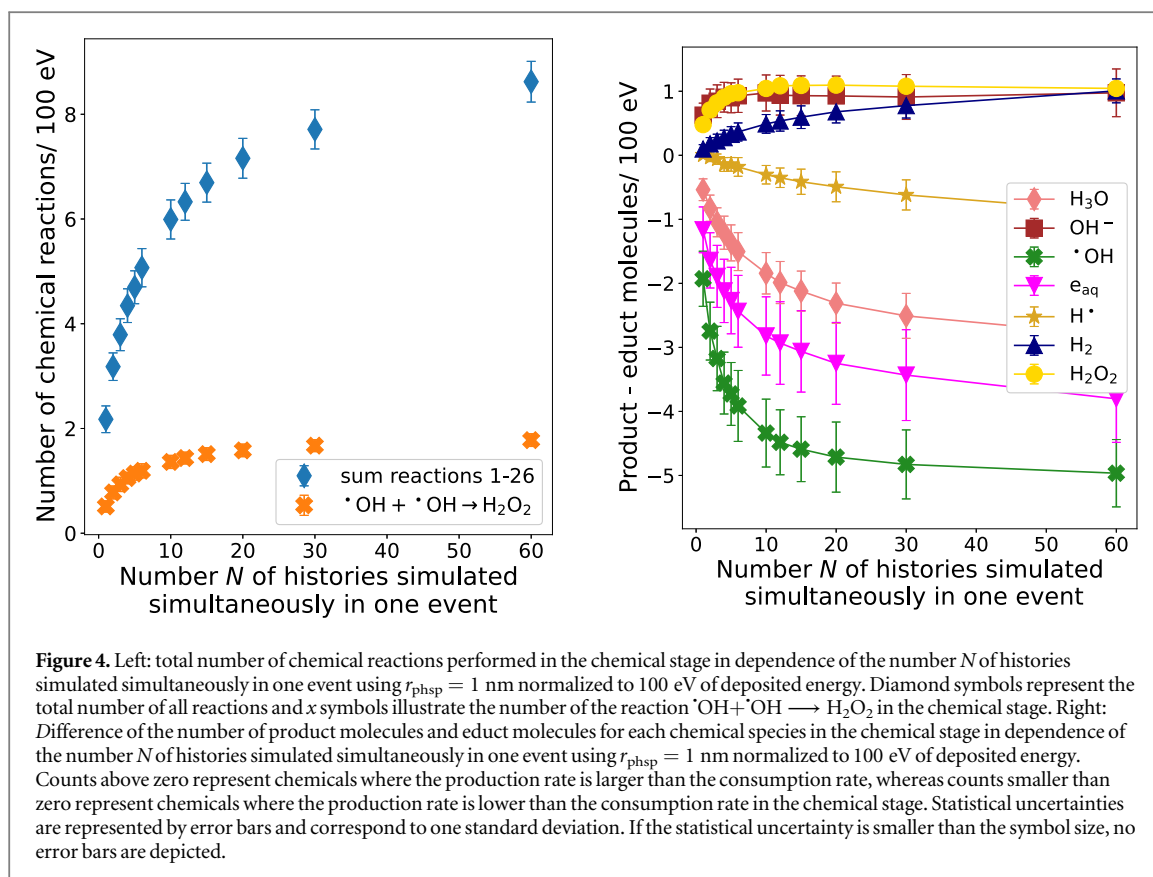
3.1. Particle source A: electron source

3.1.1. Radical yield at the end of the chemical phase in dependence of inter-track interactions

In figure 2, the G -value of $\cdot\text{OH}$ at the end of the chemical stage ($t = 1 \mu\text{s}$) is shown for all different r_{phsp} in dependence of the number N of histories simulated simultaneously in one event using electrons with an energy of 60 eV. We chose $\cdot\text{OH}$ as the molecule of interest for this comparison because it is assumed that indirect DNA damages resulting from interactions of chemical species with the DNA sugar phosphate backbone are mainly caused by $\cdot\text{OH}$ radicals (Chapman *et al* 1973, Achey and Duryea 1974, Roots and Okada 1975). For all r_{phsp} , the G -value of $\cdot\text{OH}$ reduces with increasing N (see figure 2). However, the magnitude of the decrease depends on r_{phsp} . While the decrease of the G -value is approximately exponential for small r_{phsp} , for larger r_{phsp} (approx. $r_{\text{phsp}} \geq 40$) it is rather linear. The reason is, the smaller r_{phsp} , the higher the density of electrons and the larger the probability of chemical reactions between molecules of different primary particles. For large r_{phsp} , the spatial distance between primary particles is on average larger. Correspondingly, chemical species have to diffuse farther to undergo inter-track interactions. Hence, the effect of increasing N is less pronounced. Indeed, along with N , the geometry considerably effects the density of primary electrons and, consequently, the concentration of chemical radicals. This way, N and the initial, spatial distribution of the electrons affect the dynamics and complexity of the whole chemical stage significantly. Thus, we also analyzed the G -value of all six most observed molecules (H_3O , H_2O_2 , OH^- , $\cdot\text{OH}$, e_{aq} , H^+ , H_2) in dependence on N in addition to $\cdot\text{OH}$. Therefore, in figure 3, the G -value of these chemicals is presented as a function of N for the smallest r_{phsp} ($r_{\text{phsp}} = 1 \text{ nm}$) and largest r_{phsp} ($r_{\text{phsp}} = 100 \text{ nm}$) at the end of the chemical stage. For both radii, a reduction of the chemical species e_{aq} , H_3O and $\cdot\text{OH}$ with increasing N can be observed. In turn, the number of the species OH^- , H_2 and H_2O_2 increases with increasing N . For example, comparing the reference simulation ($N = 1$) and $N = 60$ using $r_{\text{phsp}} = 1 \text{ nm}$, the G -value of H_2O_2 is twice as high. Using $r_{\text{phsp}} = 100 \text{ nm}$, the amount of H_2O_2 increases only by around 10 % in comparison to the reference. However, for H^+ , no significant difference can be observed independent on the geometry and N . Furthermore, the G -value of the molecules H_2O_2 , $\cdot\text{OH}$ and OH^- goes into saturation for high N , which means that further increasing N has no effect on these G -values (see figure 3). Transferring this to FLASH-RT would mean that a maximum dose rate could exist, above which an increase of the dose rate does not have an influence on the creation of chemical species in case of the inter-track interactions anymore.



However, the total G -value of all molecules decreases with increasing N . This can be explained by a significant increase of chemical reactions with an increase of N which is illustrated in figure 4 (left panel). For example, a reaction that occurs very frequently is reaction no. 6 in which H_2O_2 is formed from two $\cdot\text{OH}$ molecules (see table 2). This explains why the G -value of $\cdot\text{OH}$ decreases rapidly with N (see figure 3). Even though the total number of chemical species decreases with increasing N , figure 3 shows that the G -value of some molecules increase and the changes in the G -values depend on the molecule type. The reason for the different modifications of the G -value of different molecules is that some reactions occur more frequently than others with increasing N . This leads to a greater ratio of chemical reactions, that are consuming each molecule type, and reactions, that are producing each molecule type. This variable ratio in turn is responsible that the G -values of some molecules vary stronger with N than the others. The difference of the number of product and educt reactions of each chemical species is illustrated in figure 4 (right panel). Regarding the reactions of $\cdot\text{OH}$ exemplary, there is a negative and decreasing difference of reactions producing and consuming $\cdot\text{OH}$ molecules with increasing N . This means that the number of $\cdot\text{OH}$ molecules that are consumed in chemical reactions



increases stronger with N than the number of $\cdot\text{OH}$ molecules that are produced in chemical reactions⁷. Hence, this results in a decrease of the G -value of $\cdot\text{OH}$ with N at the end of the chemical stage (see figure 3).

All in all, the ratio of the chemical reactions consuming or producing the same chemical species is the reason why the G -value of some chemicals increases with N and for other molecules it decreases or even remains rather unchanged.

3.1.2. Time resolved radical yields

In order to validate that the diffusion ranges are responsible for the influence of the spatial separation of the primary particles, we investigated the time-dependent G -values of different r_{phsp} , which are shown in figure 5 for $\cdot\text{OH}$ and H_2O_2 using $r_{\text{phsp}} = 1$ nm and $r_{\text{phsp}} = 100$ nm. In general, the amount of $\cdot\text{OH}$ reduces with time for all different set-ups and more H_2O_2 is produced towards the end of the chemical stage. For the reference simulations, this is generally in agreement with the time-evolution of the G -value calculated by Ramos-Méndez *et al* (2018),⁸ who validated the chemistry included in TOPAS-nBio against other simulation studies and experimental data.

In figure 5, using $r_{\text{phsp}} = 1$ nm, the G -value of $\cdot\text{OH}$ decreases for all N with time. Already at the beginning of the chemical stage, the decrease of the G -value is more pronounced for higher N than for smaller N . The reason for this is, that for high N , the initial density of chemicals is very high and the chemicals do not need to diffuse large distances to meet a reactant. Thus, chemical reactions can already occur at the very beginning of the chemical stage ($t \leq 1$ ps) explaining the differences of the G -value for different N . To quantify this, we calculated the number of reactions that occur at $t \leq 1$ ps in dependence of N , which is in detail described in appendix C. All in all, the number of reactions at $t \leq 1$ ps increase with N (see figure C2) explaining the differences of the G -value for different N at $t = 1$ ps. At the end of the chemical stage, using $r_{\text{phsp}} = 1$ nm, the G -value of $\cdot\text{OH}$ saturates for all N . Thus, this indicates that using this setup, the G -value of $\cdot\text{OH}$ does not change much with time after 1 μs . For $r_{\text{phsp}} = 100$ nm, the profile of the G -value of $\cdot\text{OH}$ is unchanged for $N = 1$ (see figure 5). This is because no inter-track interactions are possible and thus the density of the electrons does not matter. While for $r_{\text{phsp}} = 1$ nm and $N \geq 1$ variations of the G -value are already present at the beginning of the chemical stage, for $r_{\text{phsp}} = 100$ nm

⁷ This can also be explained by the reaction rates: In sum, the reactions rates of all chemical reactions consuming $\cdot\text{OH}$ (reaction no. 2, 6, 7, 10–14) is $7.6728 \cdot 10^{10}$ /M/s whereas in sum, the reaction rates producing $\cdot\text{OH}$ (reaction no. 5, 18) is $1.415 \cdot 10^{10}$ /M/s. In general, this means that it is more likely that $\cdot\text{OH}$ is consumed than produced in the chemical stage.

⁸ The amount of molecules differs slightly in this study. This is due to the fact that different LETs were used and the G -value is dependent on the LET, which was shown by Ramos-Méndez *et al* (2018).

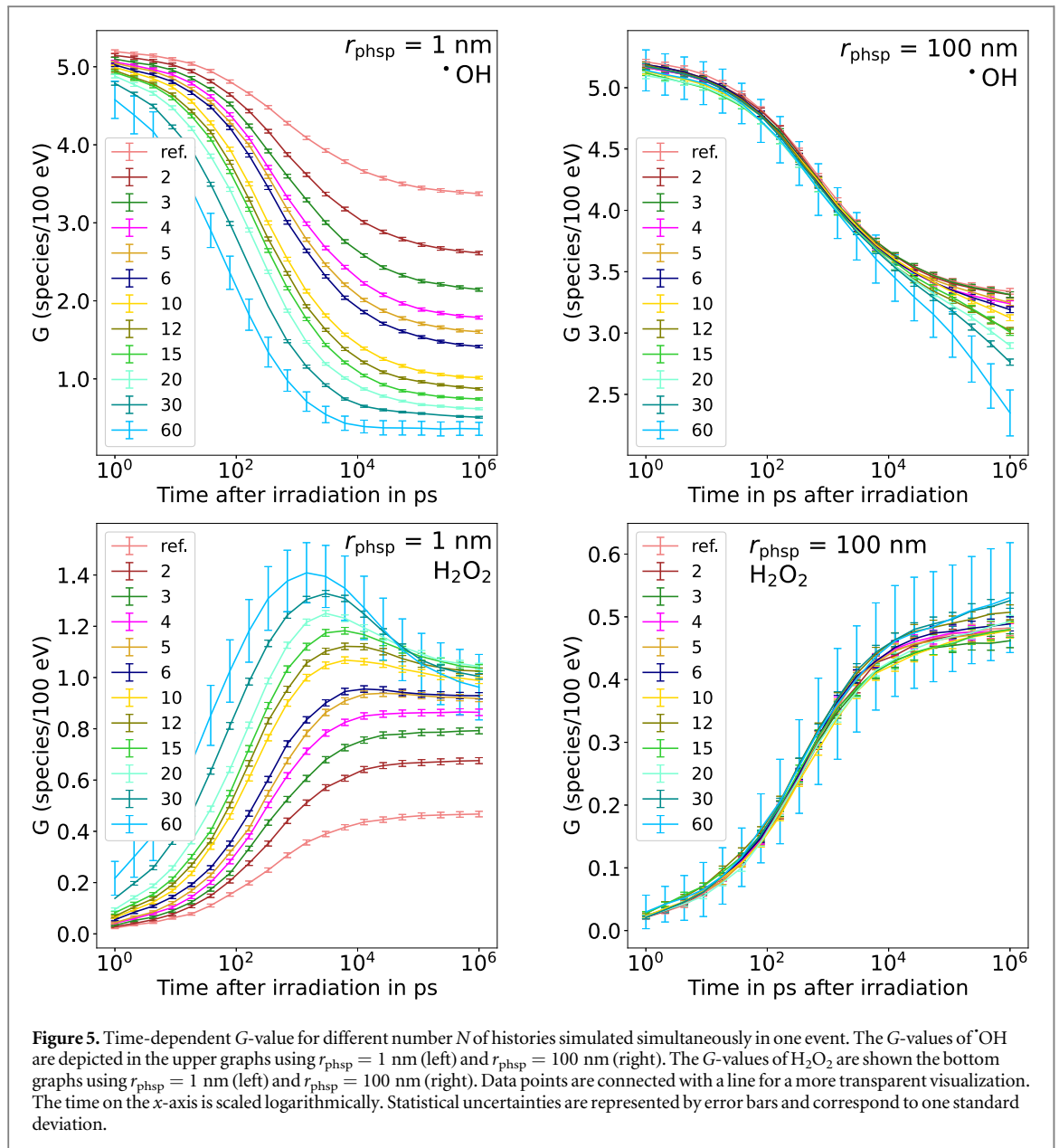


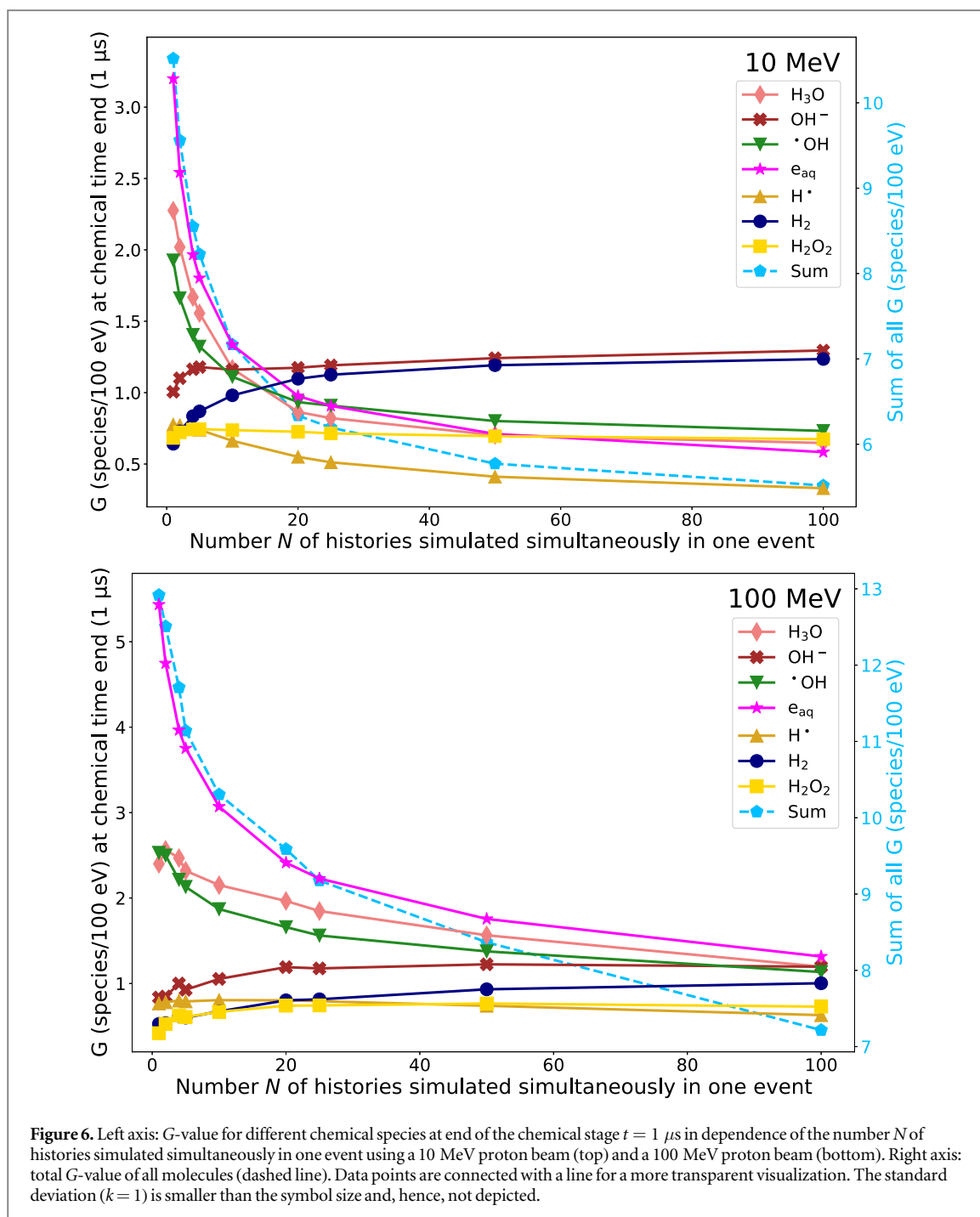
Figure 5. Time-dependent G -value for different number N of histories simulated simultaneously in one event. The G -values of $\cdot\text{OH}$ are depicted in the upper graphs using $r_{\text{phsp}} = 1 \text{ nm}$ (left) and $r_{\text{phsp}} = 100 \text{ nm}$ (right). The G -values of H_2O_2 are shown the bottom graphs using $r_{\text{phsp}} = 1 \text{ nm}$ (left) and $r_{\text{phsp}} = 100 \text{ nm}$ (right). Data points are connected with a line for a more transparent visualization. The time on the x -axis is scaled logarithmically. Statistical uncertainties are represented by error bars and correspond to one standard deviation.

changes due to inter-track interactions only become apparent from about 10^4 ps onwards. After this time period, the G -value changes for different N , which indicates that the chemicals of different primary particles diffused far enough so that inter-track interactions can occur. This can be further illustrated by calculating the theoretical mean distance between two primary particles which is approximately 1.3 nm for $r_{\text{phsp}} = 1 \text{ nm}$ and approximately 132.3 nm , 100 times larger, for $r_{\text{phsp}} = 100 \text{ nm}$.

Since H_2O_2 is created by a reaction of two $\cdot\text{OH}$ molecules, the relation of the time-dependent G -values relative to N and to the different electron distributions can be explained similar to the time-dependent G -value of $\cdot\text{OH}$. For $r_{\text{phsp}} = 1 \text{ nm}$, the G -value of H_2O_2 increases more strongly for higher N than for smaller N (see figure 5). For small N , the G -value is saturated at the chemical time end, whereas for $N \geq 10$ the G -value decreases after about 10^3 ps to 10^4 ps . We analyzed this characteristic profile in more detail by comparing the number of reactions in which H_2O_2 is consumed and produced. We could show that the varying ratio between consuming and producing H_2O_2 reactions is responsible for the changes in the profile with increasing N . For more details, see appendix C.

For the less dense electron distribution ($r_{\text{phsp}} = 100 \text{ nm}$), the time-dependent G -value of H_2O_2 does not vary much with N similar to the G -value of $\cdot\text{OH}$ (see figure 5). This can be explained, as mentioned previously for $\cdot\text{OH}$, by a low number of inter-track interactions due to large spatial separations of the primary tracks.

All in all, analyzing the time-dependent G -value of different r_{phsp} , we could indicate that the variations in the G -values for different source geometries is related to the density of chemical species and the complexity of chemical reactions.



3.2. Particle source B + C: proton sources

Once the fundamental influence of inter-track interactions has been analyzed and explained using a low energy electron source, we further examined the effects of inter-track interactions of high-LET radiation sources. In figure 6, the G -value at the end of the chemical stage at $t = 1 \mu s$ of different chemical species in dependence of the number N of histories simulated simultaneously in one event is shown for the 10 MeV (top) and 100 MeV (bottom) proton beam. Similar to the electron source, the total number of molecules (dashed line) decreases with increasing N for both proton sources. As before, the G -value of e_{aq} , H_3O and $\cdot OH$ decreases with an increasing N . In turn, the number of the species OH^- , H_2 and H_2O_2 increases with increasing N . For 100 MeV protons, the G -value of $H\cdot$ stays constant as it is the case for the electron source. However, for 10 MeV protons, the G -value of $H\cdot$ decreases slightly with increasing N . For the proton sources, saturation effects of the G -value can also be observed for high N for some molecules, such as $\cdot OH$ and OH^- . However, using the high LET (10 MeV) proton source, these effects occur already at lower N compared to the low LET (100 MeV) source.

When comparing the G -values of the proton sources without inter-track interactions ($N = 1$), it is obvious that the G -values of the two proton sources are already different. For example, the G -value of $\cdot OH$ for $N = 1$

using the 10 MeV source is 1.92 ± 0.01 , while it is 2.53 ± 0.04 applying the 100 MeV source. This is consistent with other studies in which an LET-dependence of the G -value was observed (Burns and Sims 1981). Additionally, for the high LET source the G -value of $\cdot\text{OH}$ decreases in a greater extent with increasing N than the G -value of $\cdot\text{OH}$ using the lower LET proton source. Since the density of secondary electrons is higher in the higher LET radiation, and thus also the density of chemical species of different primary particles, here, more inter-track interactions occur in the chemical phase with increasing N , which leads to the large variation of the G -values.

4. Discussion

4.1. Discussion of the radical yield with other simulation studies and experimental studies

The variation of the G -value of e_{aq}^- , $\cdot\text{OH}$, H_2 and H_2O_2 resulting from inter-track interactions (see figure 3) was also observed by Kreipl *et al* (2009) in a similar way simulating inter-track interactions of He^{2+} ions, C^{6+} ions and protons. Although they investigated inter-track interactions of only two primary particles in comparison to simulations without inter-track interactions, comparable to $N = 1$ and $N = 2$ in our simulations, inter-track interactions of numerous secondary particles contribute to the considerable change of the G -value. However, systematically increasing the number of inter-track interactions as done by our work group, illustrates effects of different particle and dose rates as described in section 2.2. The higher a dose rate, the more inter-track interactions can occur since an overlap of chemical tracks of different primary particles becomes more probable. Comparing this work with simulation studies that directly induced dose rates by varying the initial time of primary particles in a fixed pulse width, the same trend in the change of the G -value can be observed: Ramos-Méndez *et al* (2020) simulated different dose rates by simulating a constant number of primary particles delivered in pulses of different width. A maximum change in the G -value was found for a zero width pulse, which is comparable to our method in which all 60 primary particles were initialized at the same time. Even larger pulse widths of 1 ns, 1 μs and 10 μs showed significant changes in the G -value compared to conventional dose rates. Nevertheless, larger pulse widths, which are equivalent to lower dose rates, had less effects on the G -value which is in agreement with our results allowing less inter-track interactions. Comparable results were obtained by Lai *et al* (2021). In their simulation study, higher dose rates contributed to a smaller amount of $\cdot\text{OH}$ molecules. While the results of the simulation studies show a similar trend of the G -values with an increasing number of inter-track interaction or the dose rate, experimental results are not straightforward. On the one hand, Kusumoto *et al* (2020) observed a decrease of $\cdot\text{OH}$ with increasing dose rate, as investigated in the simulation studies, but on the other hand, a decrease of H_2O_2 with increasing dose rate was observed in some experimental trials (Montay-Gruel *et al* 2019, Blain *et al* 2022). This is in direct conflict with the results of our study and the mentioned simulation studies. Here, an increase of H_2O_2 has been observed for FLASH dose rates in comparison to conventional dose rates. Differences could, for example, be caused as the simulations mostly run only up to 1 μs after irradiation, whereas the experimental measurements are recorded at a later point in time. In addition, dissolved molecular oxygen is not included in some of the simulations. Since $\cdot\text{OH}$ often forms a compound with oxygen, less H_2O_2 can thus be generated by $\cdot\text{OH}$. However, since the amount of oxygen decreases for ultra-high dose rates, less $\cdot\text{OH}$ radicals might react with oxygen in comparison to low dose rates resulting in a higher production of H_2O_2 . For a more detailed discussion of the contrary observations of H_2O_2 with increasing dose rate of experimental and simulation studies we here refer to commentary by Wardman (2020).

4.2. Discussion of the radical yields in dependence of the spatial separation

As already observed when regarding the G -value of $\cdot\text{OH}$ for all r_{phsp} (see figure 2), the variation of the G -value of all chemical species with N shown in figure 3 is more pronounced for $r_{\text{phsp}} = 1$ nm than for $r_{\text{phsp}} = 100$ nm. The influence of the spatial separation between interacting tracks was also investigated by Kreipl *et al* (2009) using primary He^{2+} ions, C^{6+} ions and protons. In contrast to this work, whereby the spacing of the interacting tracks is not systematically controlled but influenced by the source radius r_{phsp} , the spatial separation in their research was systematically parameterized in the range of 0 nm and 1000 nm. Nevertheless, for all particle sources, the G -value was lowest for the smallest spatial separation of the interacting tracks as seen in our results (see figure 2). In addition, Kreipl *et al* observed that the number of interacting tracks had no influence on the yield of radicals for a spatial separation of 1000 nm. In comparison, in our study, the spatial separation for the largest radius ($r_{\text{phsp}} = 100$ nm) cannot be larger than 200 nm, which would only be the case for $N = 2$ if the particles are emitted directly opposite on the sphere surface⁹. To investigate whether the saturation effect regarding the spatial separation can be reproduced with our simulations, we simulated the G -value using a radius of

⁹ It should be mentioned that the spatial separation also depends on N . The larger N , the smaller the average distance of the initial tracks for the same r_{phsp} , since the particle density becomes larger.

$r_{\text{phsp}} = 750$ nm, corresponding to an approximately average spatial separation of 1000 nm of the initial electrons placed on the surface of the sphere. As shown in figure B1 in the appendix, varying N in the range of 1–100 has no influence on the G -value. Generally, the effect can be explained due to the fact that diffusion ranges of the chemical species up to 1000 nm are extremely improbable as shown by Ramos-Méndez *et al* (2018). Thus, chemical species of different primary particles are unlikely to react with each other at such large spatial separations. However, if N would be increased by a multiple more than 100, inter-track interactions could be triggered by the high density and thus smaller distances of the primary tracks. However, the systematic arrangement of the various primary tracks as in this study and in that of Kreipl *et al* (2009), do not reflect the situation of realistic extended beam fields. For particles sources with a different source geometry as well as with a different LET and hence, a corresponding different spatial arrangement of inelastic interactions, the situation of inter-track interactions might be different. However, in case of simulation time we investigated the spatial separation using electrons of low energy and not using the proton sources showing exemplary that the spatial arrangement of the source geometry has an effect on inter-track interactions. The results illustrate that the denser the primary tracks are, the more likely inter-track interactions occur reducing the amount of chemicals which is illustrated by a reduced G -value. In summary, the occurrence of inter-track interactions can be controlled by the spatial arrangement of the source geometry and by the number N of primary particles simulated simultaneously in one event, i.e. broadly the dose rate, all influencing the spatial distribution of the physical particle track.

4.3. Discussion of our approach: advantages, limitations and relevance to FLASH radiotherapy

In this study, inter-track interactions of chemicals produced by different primary particles were investigated whereas the primary particles were initialized simultaneously, that means at the same initial time. In fact, using ultra-high dose rates as in FLASH-RT, the particles are delivered at different initial times in a given pulse width as simulated for example by Ramos-Méndez *et al* (2020) and Lai *et al* (2021). However, simulating all interacting tracks simultaneously, as done in this study, actually has certain advantages: first, the impact of inter-track interactions on their own can be analyzed without other parameters affecting the results. Parameters could for example be the time structure of the pulses, the dose-per-pulse, the oxygen level and the type of the surrounding tissue cells, since these parameters obviously have an influence on the dynamics of chemical reactions. However, we first wanted to show that we are able to simulate inter-track interactions in TOPAS-nBio and investigate their influence on a first principal basis. Second, Abolfath *et al* (2022) pointed out that in TOPAS-nBio inter-track interactions are underestimated. By simulating all tracks simultaneously, the maximized effect of inter-track interactions can be studied.

Due to limitations in our study, a quantitative relation between N and a dose rate cannot be established. One the one hand, the temporal profile of the G -value (see figure 5) clearly illustrates that the time factor is one of the key factors for the G -value. Since in our study the particles are simulated simultaneously, that means without a separation in time, a conversion to a realistic dose rate is not feasible. One the other hand, and most importantly, the simulations are performed on microscopic scale which disables a conversion into dose, a macroscopic quantity, as discussed in detail by Abolfath *et al* (2020). For the purpose of calibrating the number N of particles simulated simultaneously against dose rates, the simulations will be adapted in a subsequent study. Simulations will be performed under the same conditions as experiments so that by comparing both G -values a reference to clinical dose rates can be obtained.

In this initial study regarding inter-track interactions we did not considered the role of oxygen in the simulations, which will, in turn, be taken into account in subsequent studies. Additionally, in further steps, scavengers should be included in the simulations since Ramos-Méndez *et al* (2021) showed that including scavengers in the chemistry simulations improves the agreement to experimental data. To improve simulations of the chemical stage and linking them to experimental conditions, the GEANT4 developers are constantly updating the code with new molecules and scavengers (Chappuis *et al* 2023). In addition, Wardman (2022) clarified the importance of scavenger systems since in biological tissue intracellular molecules can compete with the chemical reactions in 'pure water'. This could change the effect of inter-track interactions. But as we could show that inter-track interactions occur also in the picosecond regime, we expect that the effect of inter-track interactions is still significant in the presence of scavengers as in cellular mediums. Nevertheless, this should be investigated in further studies including the mechanisms of living cells. Until now, however, there are no established simulation codes that can cover the needs of those simulations as pointed out by Wardman (2022) and will be a quite challenging task.

Furthermore to the presented results, since we could show that inter-track interactions influence the yield of chemicals, we now apply our approach to investigate the resulting DNA damage yield in more realistic simulation set-ups e.g. including a nucleus model and optimize the spatial and temporal arrangement of initial particles.

As an outlook, TOPAS-nBio has been updated to version 2.0, which provides the simulation of inter-track interactions. Therefore, we will evaluate in a following study if comparable results can be achieved by simulations applying our approach and simulations using TOPAS-nBio 2.0.

This research showed that increasing the number of histories from which the chemical species can interact with each others, representing higher dose rates, reduces the total G -value (see figures 3 and 6) and hence more chemical reactions occur. Increasing the number N of histories simulated simultaneously in one event has a comparable effect on the G -value like increasing the dose rate as observed in an experimental study by Kusumoto *et al* (2020). With higher dose rates, and correspondingly more inter-track interactions, a reduction of $\cdot\text{OH}$ is observed. Since $\cdot\text{OH}$ is considered to be mainly responsible for indirect damages on the DNA, we hypothesize that this has an impact on the amount and distribution of DNA damages. This in turn, could play a crucial roll in the FLASH effect. To provide an explanation of the FLASH effect, these results are surely not sufficient enough since a difference between tumor and normal tissue response cannot be specified. But as the FLASH effect is 'the result of a multi-parameter situation' (Rothwell *et al* 2021), each individual variation is relevant. The exact explanation of the FLASH effect is beyond the scope of this paper but inter-track interactions may be a parameter to be considered in the mechanism.

5. Conclusion

In this work, the influence of the dose rate on the yield of chemical species was investigated by enabling inter-track interactions in radiobiological simulations using TOPAS-nBio. We developed an approach to generate inter-track interactions in the chemical stage of the simulations. It was shown that increasing the number N of histories simulated simultaneously in one event as a substitute for an increased dose rate, leads to significant changes in the yield of chemical species. In particular, the yield of $\cdot\text{OH}$ radicals decreases with increasing number of inter-track interactions. However, the magnitude of the variation of the chemical yields depends on the LET of the primary particles and the geometry of the source. The variation in chemical radicals may induce changes in the amount of indirect DNA damages, which in turn may be relevant in explaining the FLASH effect.

Acknowledgments

The project was supported by the Federal Ministry of Education and Research within the scope of the grant 'Physikalische Modellierung für die individualisierte Partikel-Strahlentherapie und Magnetresonanztomographie', (MiPS, Grant Number 13FH726IX6).

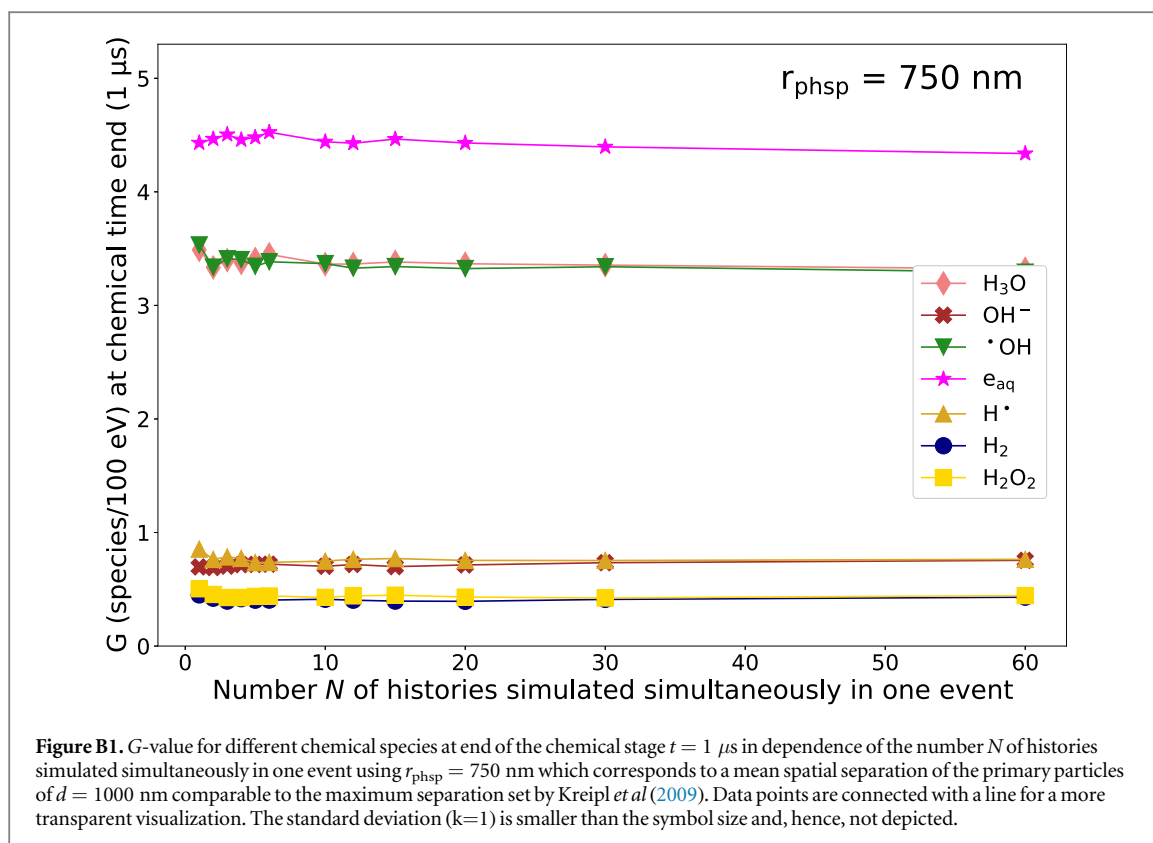
Data availability statement

The data cannot be made publicly available upon publication because no suitable repository exists for hosting data in this field of study. The data that support the findings of this study are available upon reasonable request from the authors.

Appendix A. Generation of inter-track interactions in TOPAS-nBio using a phase space file.

In order to enable inter-track interactions in TOPAS, i.e. to simulate N histories in one event, we scored a phase space file of the source and modified the column called `Flag` to tell if this is the First Scored Particle from this History (1 means true).¹⁰ Suppose one simulates M primary particles and scores a phase space file such that at least one particle from each primary particle reaches the surface on which the phase space file is scored. Then the mentioned column in the phase space file contains M times the flag 1. In order to simulate N histories simultaneously in one event in our simulations, the flag was modified in such a way that only every N th entry with the flag 1 remains and the others are replaced by the flag 0. In this way, all particles between two particles with flag 1 are assigned to one event and inter-track interactions are possible.

¹⁰ For details of the phase space file scorer see the TOPAS documentation <https://topas.readthedocs.io/en/latest/parameters/scoring/phasespace.html>.



Appendix B. G-value using $r_{\text{phsp}} = 750 \text{ nm}$

For the purpose of comparing the G-value simulating a similar maximum spatial separating of interacting tracks as by Kreipl *et al* (2009), we performed our simulations using $r_{\text{phsp}} = 750 \text{ nm}$. This way, we achieved a mean spatial separation of the tracks of around 1000 nm as set by Kreipl *et al*. The G-values in dependence of N using $r_{\text{phsp}} = 750 \text{ nm}$ are shown in figure B1. As observed in Kreipl *et al*'s results, the G-value does not change with N since the distance of chemicals produced in different tracks is too large. Hence, inter-track interactions do not occur.

Appendix C. Supplementary data for the analysis of the time-resolved G-value

Since we recognized that the time-dependent G-values of all N vary already at the beginning of the chemical stage at 1 ps using $r_{\text{phsp}} = 1 \text{ nm}$ and we hypothesized, that in case of more interacting chemicals, more chemical reactions occur, we calculated the number of reactions that occur at $t \leq 1 \text{ ps}$ in dependence of N using the electron source with $r_{\text{phsp}} = 1 \text{ nm}$. For this, we used the command `i:Ts/ChemistryVerbosity=2` in TOPAS-nBio. This way, for each history, all chemical reactions that took place at $t \geq 1 \text{ ps}$ are printed in the output file including the time of the reaction. For example, an extract of the output can look as illustrated in figure C1. The exemplary output in figure C1 demonstrates that chemical reactions can already take place at 1 ps which are then considered in the calculation of the G-value at 1 ps. Figure C2 shows that the number of reactions per 100 eV of deposited energy at $t \leq 1 \text{ ps}$ increases significantly with N . Comparing $N = 1$ and $N = 60$, the number of reactions per 100 eV of deposited energy at $t \geq 1 \text{ ps}$ increases by a factor of approximately 2. One of the reactions that occur quite frequently in this time interval is reaction no. 6 (see table 2) in which H_2O_2 is produced while $\cdot\text{OH}$ is consumed. The occurrence of this reaction increases strongly with N which explains the decreasing G-value of $\cdot\text{OH}$ at 1 ps with increasing N in figure 5.

However, to be sure, that the difference of the G-value of $\cdot\text{OH}$ at 1 ps for different N (see figure 5) is a result of chemical reactions at $t \leq 1 \text{ ps}$ (see figure C2) we re-calculated the G-value for $t < 1 \text{ ps}$ by considering the chemical reactions at $t \leq 1 \text{ ps}$. Therefore, the number of molecules that are produced through chemical reactions in this time interval are subtracted from the amount of molecules counted at 1 ps and molecules that are consumed are added to the amount of molecules counted at 1 ps. In principal, the number N of histories simulated simultaneously in one event should not have an influence on the initial yield of chemicals (here at $t < 1 \text{ ps}$), since these are generated in the pre-chemical stage based on the physical interactions (ionization,


```

Begin processing for Run: 0, History: 0
*** G4Scheduler starts processing
At time : 9.0993 ps Reaction : OH^0 (-12) + OH^0 (-13) -> H2O2^0 (-14)
*** G4Scheduler ends at time : 1 us

-----
Begin processing for Run: 0, History: 1
*** G4Scheduler starts processing
At time : 1 ps Reaction : H^0 (-14) + OH^0 (-13) -> No product
At time : 1 ps Reaction : e_aq^-1 (-4) + H3O^1 (-11) -> H^0 (-15)
At time : 3 ps Reaction : OH^0 (-10) + e_aq^-1 (-12) -> OH^-1 (-16)
At time : 61.971 ps Reaction : e_aq^-1 (-6) + OH^0 (-9) -> OH^-1 (-17)
At time : 666.22 ps Reaction : H3O^1 (-8) + OH^-1 (-16) -> No product
*** G4Scheduler ends at time : 1 us

```

Figure C1. Exemplary extract of an output file using `i:Ts/ChemistryVerbosity = 2` in TOPAS-nBio regarding all chemical reactions per history and time. The numbers in brackets behind each molecule name, correspond to the TrackIDs of the respective molecules. In this simulation, no inter-track interactions were allowed.

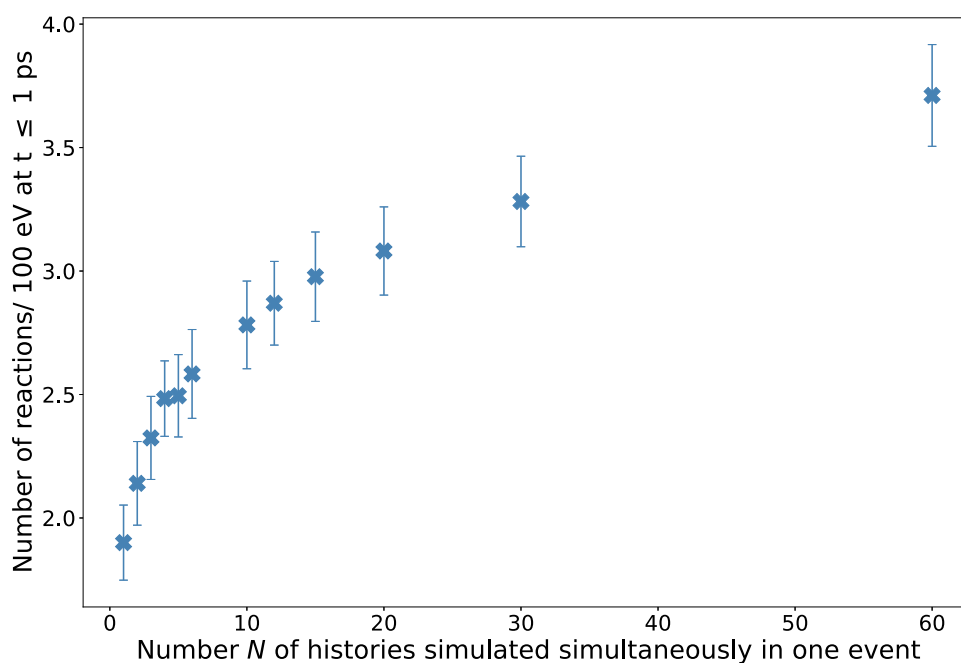
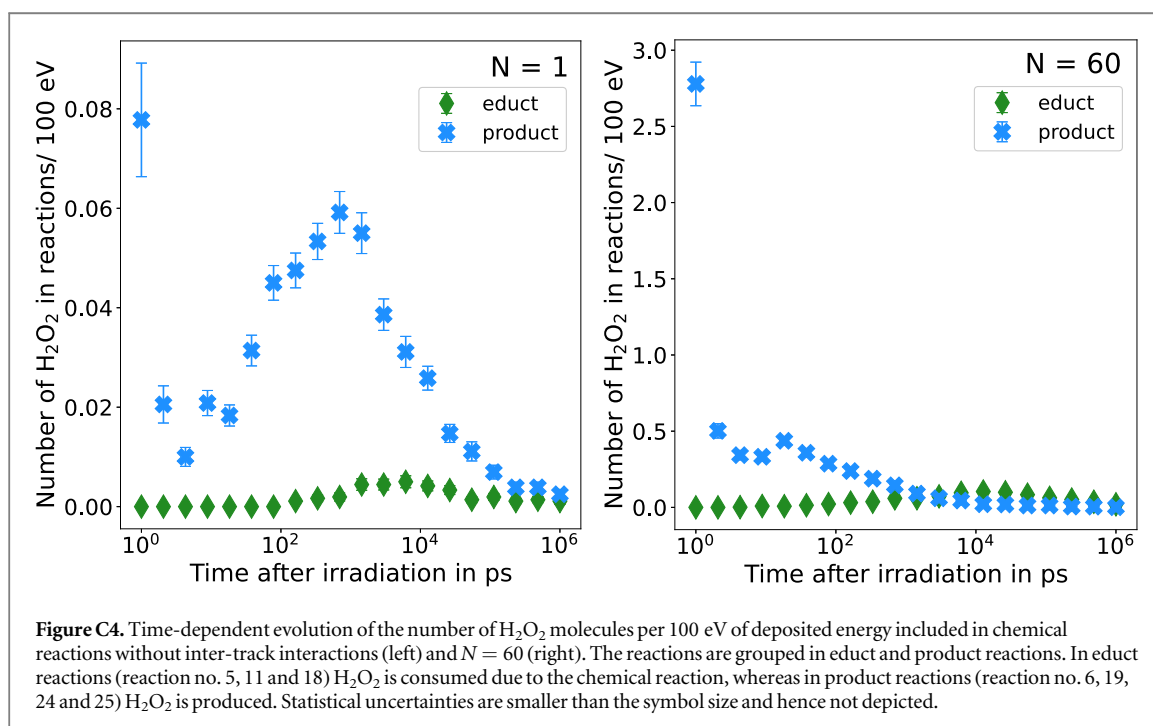
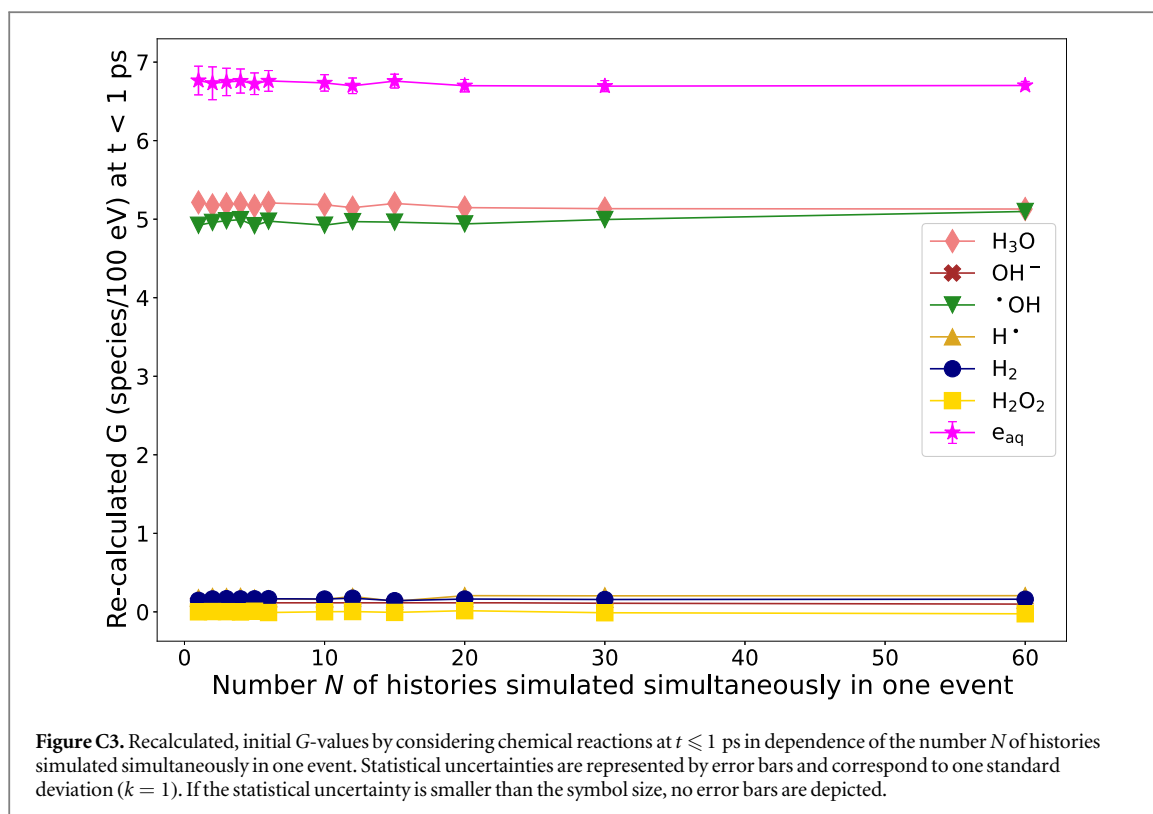


Figure C2. Mean number of chemical reactions that occurred at $t \leq 1$ ps normalized to 100 eV of deposited energy. Statistical uncertainties are represented by error bars and correspond to one standard deviation.

excitation, attachment, see table 1) which do not depend on N . Hence, in principle, the initial G -value should be the same for all N , which is the case as shown in figure C3. This proves that the difference of the G -values at $t = 1$ ps in figure 5 is a result of chemical reactions and our approach does not affect the initial distribution of chemical radicals.

Regarding the characteristic profile of the G -value of H_2O_2 using $r_{\text{phsp}} = 1$ nm observed in figure 5, we examined the number of reactions in which H_2O_2 is involved at fixed time intervals. In figure C4, the number of H_2O_2 molecules included in the reactions per 100 eV of deposited energy are shown for the reference simulation without inter-track interaction (left) and for $N = 60$ (right). We grouped the reactions in so called educt- and product-reactions. Concretely, educt-reactions concern the reactions 5, 11 and 18 from table 2 in which H_2O_2 is consumed, and product-reactions include the reactions 6, 19, 24 and 25 in which H_2O_2 is produced. Regarding the reference simulation, the production rate of H_2O_2 is highest at the beginning of the chemical stage and reaches a second maximum around 1 ns. Towards the end of the chemical stage the production rate decreases. At the beginning of the chemical stage up to 10^3 ps, H_2O_2 is not consumed via educt-reactions. After this time period, educt-reactions occur in small amounts. Nevertheless, for $N = 1$, more H_2O_2 is produced than consumed during the whole chemical stage. Thus, the diminished gradient of the increasing G -value of H_2O_2 using $r_{\text{phsp}} = 1$ nm of the reference simulation ($N = 1$) shown in figure 5 can be attributed to a decreased number



of product-reactions and an increase of educt-reactions. In comparison, regarding the results of $N = 60$, the amount of H_2O_2 produced by chemical reactions is around 30 times larger at the beginning of the chemical stage than for the reference simulation but decreases to a greater extent with time. The number of consumed H_2O_2 is very low at the beginning of the chemical stage, but contrary to the reference simulation, after 10^3 ps, more H_2O_2 is consumed than produced by chemical reactions. This results in a reduced G-value of H_2O_2 after 10^3 ps for $N = 60$ using $r_{\text{phsp}} = 1$ nm in figure 5. In conclusion, the difference between the characteristic profiles of the time-dependent G-value of the reference simulation ($N = 1$) and $N = 60$ using $r_{\text{phsp}} = 1$ nm can be explained

due to the fact that for the reference simulation, the production rate of H_2O_2 is always larger than the consumption rate, i.e. number of educt-reactions, whereas for $N = 60$, at the end of the chemical stage, the consumption is higher than the production of H_2O_2 .

ORCID iDs

Veronika Flatten  <https://orcid.org/0000-0003-4963-6838>

Klemens Zink  <https://orcid.org/0000-0001-5785-4101>

Kilian-Simon Baumann  <https://orcid.org/0000-0003-1223-523X>

References

- Abolfath R, Baikalov A, Bartzsch S, Afshordi N and Mohan R 2022 The effect of non-ionizing excitations on the diffusion of ion species and inter-track correlations in flash ultra-high dose rate radiotherapy *Phys. Med. Biol.* **10** 105005
- Abolfath R, Grosshans D and Mohan R 2020 Oxygen depletion in FLASH ultra-high-dose-rate radiotherapy: a molecular dynamics simulation *Med. Phys.* **47** 6551–61
- Achey P and Duryea H 1974 Production of DNA strand breaks by the hydroxyl radical *Int. J. Radiat. Biol. Related Stud. Phys. Chem. Med.* **25** 595–601
- Agostinelli S et al 2003 GEANT4—a simulation toolkit *Nucl. Instrum. Methods Phys. Res. A* **506** 250–303
- Alanazi A, Meesungnoen J and Jay-Gerin J-P 2021 A computer modeling study of water radiolysis at high dose rates. Relevance to FLASH radiotherapy *Radiat. Res.* **195** 149–62
- Allison J et al 2006 GEANT4 developments and applications *IEEE Trans. Nucl. Sci.* **53** 270–8
- Baikalov A, Abolfath R, Mohan R, Schüler E, Wilkens J J and Bartzsch S 2022 Modeling interspur interactions as a potential mechanism of the FLASH effect arXiv:2207.12287
- Bernal M A et al 2015 Track structure modeling in liquid water: a review of the Geant4-DNA very low energy extension of the Geant4 Monte Carlo simulation toolkit *Phys. Med.* **31** 861–74
- Blain G et al 2022 Proton irradiations at ultra-high dose rate vs. conventional dose rate: strong impact on hydrogen peroxide yield *Radiat. Res.* **198** 318–24
- Boscolo D, Scifoni E, Durante M, Krämer M and Fuss M C 2021 oxygen depletion explain the FLASH effect? A chemical track structure analysis *Radiother. Oncol.* **162** 68–75
- Bourhis J et al 2019 Treatment of a first patient with FLASH-radiotherapy *Radiother. Oncol.* **139** 18–22
- Buonanno M, Grilj V and Brenner D J 2019 Biological effects in normal cells exposed to FLASH dose rate protons *Radiother. Oncol.* **139** 51–5
- Burns W G and Sims H E 1981 Effect of radiation type in water radiolysis, Journal of the Chemical Society *Faraday Trans. 1: Phys. Chem. Conden. Phases* **77** 2803–13
- Chapman J, Reuvers A, Borsa J and Greenstock C 1973 Chemical radioprotection and radiosensitization of mammalian cells growing *in vitro* *Radiat. Res.* **56** 291–306
- Chappuis F, Grilj V, Tran H N, Zein S A, Bochud F, Bailat C, Incerti S and Desorgher L 2023 Modeling of scavenging systems in water radiolysis with Geant4-DNA *Phys. Med.* **108** 102549
- Derksen L, Pfuhl T, Engenhardt-Cabillic R, Zink K and Baumann K-S 2021 Investigating the feasibility of TOPAS-nBio for Monte Carlo track structure simulations by adapting GEANT4-DNA examples application *Phys. Med. Biol.* **66** 175023
- Faddegon B, Ramos-Mendez J, Schuemann J, McNamara A, Shin J, Perl J and Paganetti H 2020 The TOPAS tool for particle simulation, a Monte Carlo simulation tool for physics, biology and clinical research *Phys. Med.* **72** 114–21
- Favaudon V et al 2014 Ultrahigh dose-rate FLASH irradiation increases the differential response between normal and tumor tissue in mice *Sci. Transl. Med.* **6** 245ra93–245ra93
- Fouillade C et al 2020 FLASH irradiation spares lung progenitor cells and limits the incidence of radio-induced senescence *Clin. Cancer Res.* **26** 1497–506
- Gao Y, Liu R, Chang C-W, Charyyev S, Zhou J, Bradley J D, Liu T and Yang X 2022 A potential revolution in cancer treatment: a topical review of FLASH radiotherapy *J. Appl. Clin. Med. Phys.* **23** e13790
- Hahn M B and Villate J M Z 2021 Combined cell and nanoparticle models for TOPAS to study radiation dose enhancement in cell organelles *Sci. Rep.* **11** 6721
- Intensity Modulated Radiation Therapy Collaborative Working Group and others 2001 Intensity-modulated radiotherapy: current status and issues of interest *Int. J. Radiat. Oncol. Biol. Phys.* **51** 880–914
- Incerti S et al 2010a The Geant4-DNA project The Geant4-DNA collaboration *Int. J. Model. Simul. Sci. Comput.* **1** 157–78
- Incerti S et al 2018 GEANT4-DNA example applications for track structure simulations in liquid water: a report from the GEANT4-DNA Project *Med. Phys.* **45** e722–39
- Jansen J, Knoll J, Beyreuther E, Pawelke J, Skuza R, Hanley R, Brons S, Pagliari F and Seco J 2021 Does FLASH deplete oxygen? Experimental evaluation for photons, protons, and carbon ions *Med. Phys.* **48** 3982–90
- Kacem H, Almeida A, Cherbuin N and Vozenin M-C 2021 Understanding the FLASH effect to unravel the potential of ultra-high dose rate irradiation *Int. J. Radiat. Biol.* **98** 506–16
- Karamitros M et al 2011 Modeling radiation chemistry in the GEANT4 toolkit *Prog. Nucl. Sci. Technol.* **2** 503–8
- Karamitros M et al 2014 Diffusion-controlled reactions modeling in GEANT4-DNA *J. Comput. Phys.* **274** 841–82
- Kim M M, Darafsheh A, Schuemann J, Dokic I, Lundh O, Zhao T, Ramos-Méndez J, Dong L and Petersson K 2021 Development of ultra-high dose rate (FLASH) particle therapy *IEEE Trans. Radiat. Plasma Med. Sci.* **6** 252–62
- Klapproth A P, Schuemann J, Stangl S, Xie T, Li W B and Multhoff G 2021 Multi-scale Monte Carlo simulations of gold nanoparticle-induced DNA damages for kilovoltage X-ray irradiation in a xenograft mouse model using TOPAS-nBio *Cancer Nanotechnol.* **12** 1–18
- Kreipl M S, Friedland W and Paretzke H G 2009 Interaction of ion tracks in spatial and temporal proximity *Radiat. Environ. Biophys.* **48** 349–59
- Kusumoto T, Kitamura H, Hojo S, Konishi T and Kodaira S 2020 Significant changes in yields of 7-hydroxy-coumarin-3-carboxylic acid produced under FLASH radiotherapy conditions *RSC Adv.* **10** 38709–14

- Lai Y, Jia X and Chi Y 2021 Modeling the effect of oxygen on the chemical stage of water radiolysis using GPU-based microscopic Monte Carlo simulations, with an application in FLASH radiotherapy *Phys. Med. Biol.* **66** 025004
- Mascia A E et al 2023 Proton FLASH radiotherapy for the treatment of symptomatic bone metastases: the FAST-01 nonrandomized trial *JAMA Oncol.* **9** 62–9
- McMahon SJ, Schuemann J, Paganetti H and Prise K M 2016 Mechanistic modelling of DNA repair and cellular survival following radiation-induced DNA damage *Sci. Rep.* **6** 1–14
- McNamara A, Geng C, Turner R, Mendez J R, Perl J, Held K, Faddegon B, Paganetti H and Schuemann J 2017 Validation of the radiobiology toolkit TOPAS-nBio in simple DNA geometries *Phys. Med.* **33** 207–15
- McNamara A L et al 2018 Geometrical structures for radiation biology research as implemented in the TOPAS-nBio toolkit *Phys. Med. Biol.* **63** 175018
- Mohan R and Grosshans D 2017 Proton therapy-present and future *Adv. Drug Deliv. Rev.* **109** 26–44
- Montay-Gruel P et al 2019 Long-term neurocognitive benefits of FLASH radiotherapy driven by reduced reactive oxygen species *Proc. Natl Acad. Sci.* **116** 10943–51
- Otto K 2008 Volumetric modulated arc therapy: IMRT in a single gantry arc *Med. Phys.* **35** 310–7
- Perl J, Shin J, Schümann J, Faddegon B and Paganetti H 2012 TOPAS: an innovative proton Monte Carlo platform for research and clinical applications *Med. Phys.* **39** 6818–37
- Pimblott S M and LaVerne J A 2007 Production of low-energy electrons by ionizing radiation *Radiat. Phys. Chem.* **76** 1244–7
- Ramos-Méndez J, Domínguez-Kondo N, Schuemann J, McNamara A, Moreno-Barbosa E and Faddegon B 2020 LET-dependent intertrack yields in proton irradiation at ultra-high dose rates relevant for FLASH therapy *Radiat. Res.* **194** 351–62
- Ramos-Méndez J, Perl J, Schuemann J, McNamara A, Paganetti H and Faddegon B 2018 Monte Carlo simulation of chemistry following radiolysis with TOPAS-nBio *Phys. Med. Biol.* **63** 105014
- Ramos-Méndez J et al 2021 TOPAS-nBio validation for simulating water radiolysis and DNA damage under low-LET irradiation *Phys. Med. Biol.* **66** 175026
- Roots R and Okada S 1975 Estimation of life times and diffusion distances of radicals involved in x-ray-induced DNA strand breaks or killing of mammalian cells *Radiat. Res.* **64** 306–20
- Rothwell B C, Kirkby N, Merchant M J, Chadwick A, Lowe M, Mackay R I, Hendry J H and Kirkby K J 2021 Determining the parameter space for effective oxygen depletion for FLASH radiation therapy *Phys. Med. Biol.* **66** 055020
- Ruan J-L et al 2021 Irradiation at ultra-high (FLASH) dose rates reduces acute normal tissue toxicity in the mouse gastrointestinal system *Int. J. Radiat. Oncol. * Biol. * Phys.* **111** 1250–61
- Rudek B, McNamara A, Ramos-Méndez J, Byrne H, Kuncic Z and Schuemann J 2019 Radio-enhancement by gold nanoparticles and their impact on water radiolysis for x-ray, proton and carbon-ion beams *Phys. Med. Biol.* **64** 175005
- Schuemann J, McNamara A L, Ramos-Méndez J, Perl J, Held K D, Paganetti H, Incerti S and Faddegon B 2019 TOPAS-nBio: an extension to the TOPAS simulation toolkit for cellular and sub-cellular radiobiology *Radiat. Res.* **191** 125–38
- Small K et al 2021 Evaluating very high energy electron RBE from nanodosimetric pBR322 plasmid DNA damage *Sci. Rep.* **11** 1–12
- Stephan F et al 2022 Flashlab@ Pitz: New R&D platform with unique capabilities for electron FLASH and VHEE radiation therapy and radiation biology under preparation at Pitz *Phys. Med.* **104** 174–87
- Testa M, Schuemann J, Lu H-M, Shin J, Faddegon B, Perl J and Paganetti H 2013 Experimental validation of the TOPAS Monte Carlo system for passive scattering proton therapy *Med. Phys.* **40** 1–16
- Thompson S J, Prise K M and McMahon S J 2023 Investigating the potential contribution of inter-track interactions within ultra-high dose-rate proton therapy *Phys. Med. Biol.* **68** 055006
- Van Delinder K W, Khan R and Gräfe J L 2021 Radiobiological impact of gadolinium neutron capture from proton therapy and alternative neutron sources using TOPAS-nBio *Med. Phys.* **48** 4004–16
- Venkatesulu B P, Sharma A, Pollard-Larkin J M, Sadagopan R, Symons J, Neri S, Singh P K, Tailor R, Lin S H and Krishnan S 2019 Ultra high dose rate (35 Gy s^{-1}) radiation does not spare the normal tissue in cardiac and splenic models of lymphopenia and gastrointestinal syndrome *Sci. Rep.* **9** 1–9
- Wardman P 2020 Radiotherapy using high-intensity pulsed radiation beams (FLASH): a radiation-chemical perspective *Radiat. Res.* **194** 607–17
- Wardman P 2022 Approaches to modeling chemical reaction pathways in radiobiology *Int. J. Radiat. Biol.* **98** 1399–413
- Warmenhoven J W, Henthorn N T, Ingram S P, Chadwick A L, Sotiropoulos M, Korabel N, Fedotov S, Mackay R I, Kirkby K J and Merchant M J 2020 Insights into the non-homologous end joining pathway and double strand break end mobility provided by mechanistic in silico modelling *DNA Repair* **85** 102743
- Wilson J D, Hammond E M, Higgins G S and Petersson K 2020 Ultra-high dose rate (FLASH) radiotherapy: silver bullet or fool's gold? *Front. Oncol.* **9** 1563
- Wilson R R 1946 Radiological use of fast protons *Radiology* **47** 487–91
- Zhou G 2020 Mechanisms underlying FLASH radiotherapy, a novel way to enlarge the differential responses to ionizing radiation between normal and tumor tissues *Radiat. Med. Protection* **1** 35–40
- Zhu H et al 2020a Cellular response to proton irradiation: a simulation study with TOPAS-nBio *Radiat. Res.* **194** 9–21
- Zhu H et al 2020b A parameter sensitivity study for simulating DNA damage after proton irradiation using TOPAS-nBio *Phys. Med. Biol.* **65** 085015

ACCEPTED MANUSCRIPT • OPEN ACCESS

Comparison of two methods simulating inter-track interactions using the radiobiological Monte Carlo toolkit TOPAS-nBio

To cite this article before publication: Larissa Derksen *et al* 2024 *Phys. Med. Biol.* in press <https://doi.org/10.1088/1361-6560/ad1cf4>

Manuscript version: Accepted Manuscript

Accepted Manuscript is “the version of the article accepted for publication including all changes made as a result of the peer review process, and which may also include the addition to the article by IOP Publishing of a header, an article ID, a cover sheet and/or an ‘Accepted Manuscript’ watermark, but excluding any other editing, typesetting or other changes made by IOP Publishing and/or its licensors”

This Accepted Manuscript is © 2024 The Author(s). Published on behalf of Institute of Physics and Engineering in Medicine by IOP Publishing Ltd.



As the Version of Record of this article is going to be / has been published on a gold open access basis under a CC BY 4.0 licence, this Accepted Manuscript is available for reuse under a CC BY 4.0 licence immediately.

Everyone is permitted to use all or part of the original content in this article, provided that they adhere to all the terms of the licence <https://creativecommons.org/licenses/by/4.0>

Although reasonable endeavours have been taken to obtain all necessary permissions from third parties to include their copyrighted content within this article, their full citation and copyright line may not be present in this Accepted Manuscript version. Before using any content from this article, please refer to the Version of Record on IOPscience once published for full citation and copyright details, as permissions may be required. All third party content is fully copyright protected and is not published on a gold open access basis under a CC BY licence, unless that is specifically stated in the figure caption in the Version of Record.

View the [article online](#) for updates and enhancements.

Comparison of two methods simulating inter-track interactions using the radiobiological Monte Carlo toolkit TOPAS-nBio

Larissa Derksen¹, Sebastian Adeberg^{2,3,4}, Klemens Zink^{1,2,3},
Kilian-Simon Baumann^{1,2,3}

¹University of Applied Sciences, Institute of Medical Physics and Radiation Protection, Giessen, Germany

²Marburg University Hospital, Department of Radiotherapy and Radiation Oncology, Marburg, Germany

³Marburg Ion-Beam Therapy Center (MIT), Department of Radiotherapy and Radiation Oncology, Marburg University Hospital, Marburg, Germany

⁴University Cancer Center, Frankfurt-Marburg, Germany

E-mail: larissa.derksen@biotecmed.thm.de

Abstract.

Objective: To compare two independently developed methods that enable modelling inter-track interactions in TOPAS-nBio by examining the yield of radiolytic species in radiobiological Monte Carlo track structure simulations. One method uses a phase space file to assign more than one primary to one event, allowing for inter-track interaction between these primary particles. This method has previously been developed by this working group and published earlier. Using the other method, chemical reactions are simulated based on a new version of the independent reaction time approach to allow inter-track interactions.

Approach: G-values were calculated and compared using both methods for different numbers of tracks able to undergo inter-track interactions.

Main results: Differences in the G-values simulated with the two methods strongly depend on the molecule type, and deviations can range up to 3.9% (H₂O₂), although, on average, the deviations are smaller than 1.5%.

Significance: Both methods seem to be suitable for simulating inter-track interactions, as they provide comparable G-values even though both techniques were developed independently of each other.

1
2 *Comparing two methods simulating inter-track interactions in TOPAS-nBio* 2
3

4
5 18 *Keywords:* Monte Carlo simulation, GEANT4-DNA, TOPAS-nBio, inter-track interac-
6
7 19 tion, radiolysis, radiation chemistry
8

9
10 20

11
12
13 21 Submitted to: *Phys. Med. Biol.*
14
15
16
17
18
19
20
21
22
23
24
25
26
27
28
29
30
31
32
33
34
35
36
37
38
39
40
41
42
43
44
45
46
47
48
49
50
51
52
53
54
55
56
57
58
59
60

Accepted Manuscript

1
2
3 *Comparing two methods simulating inter-track interactions in TOPAS-nBio* 3

4
5 **1. Introduction**

6
7
8 23 The radiobiological Monte Carlo toolkit TOPAS-nBio (Schuemann et al. 2019), an
9
10 24 extension of TOPAS (Perl et al. 2012, Faddegon et al. 2020), has recently been updated
11
12 25 to version 2.0, introducing new features. One feature is the simulation of inter-track
13
14 26 interactions between chemical radicals from different primary tracks and their effects on
15
16 27 the yield of chemicals during the chemical stage (Ramos-Méndez et al. 2020).

17
18 28 Inter-track interactions occur when the chemical stage ($t \geq 1$ ps) of two or more primary
19
20 29 particles overlaps in time, which may happen at ultra-high dose rates emitting a large
21
22 30 number of particles in very short time intervals. This way, molecules generated through
23
24 31 the radiolysis of water cannot only interact within their track (intra-track interactions),
25
26 32 but can also perform chemical reactions with molecules from another track (inter-track
27
28 33 interactions). In TOPAS-nBio version 1.0, inter-track interactions are not taken into
29
30 34 account by default since under conventional conditions and dose rates of under 0.03 Gy/s
31
32 35 in radiotherapy inter-track interactions are highly improbable (Lai et al. 2021). Thus, all
33
34 36 physical and chemical interactions of one track are supposed to be independent of other
35
36 37 tracks and are simulated sequentially, meaning that chemicals from different primaries
37
38 38 cannot interact with each other. However, applying new techniques in radiotherapy like
39
40 39 the use of ultra-high dose rate, it cannot be assured that the events occur independently
41
42 40 of each other. Even though the time scale of physical interactions is quite small (1 fs)
43
44 41 (Ramos-Méndez et al. 2018), the chemical stage of different primary particles could
45
46 42 overlap, making inter-track interactions possible (Lai et al. 2021, Baikalov et al. 2022).
47
48 43 However, in TOPAS-nBio 1.0, there is no feature included allowing for the modelling
49
50 44 of inter-track interactions. Thus, in a preliminary work (Derksen et al. 2023), we
51
52 45 developed a method enabling inter-track interactions and investigated their effect on the
53
54 46 dynamics of the chemical stage following radiation using TOPAS-nBio 1.0. Recently,
55
56
57
58
59
60

Comparing two methods simulating inter-track interactions in TOPAS-nBio ⁴

an updated version of TOPAS-nBio 2.0 was released, in which inter-track interactions can be modeled by default using a specific scorer.

The aim of this study is to compare these two independently developed methods for simulating inter-track interactions in TOPAS-nBio. Therefore, we examined the yield of chemicals following the irradiation of a water-filled sphere using an isotropic electron source of 4.5 keV, modelling different amounts of inter-track interactions.

2. Materials and methods

2.1. The Monte Carlo toolkit TOPAS-nBio

Performing track structure simulations, we used TOPAS-nBio version 2.0 with TOPAS version 3.9 to simulate physical and chemical interactions following the irradiation. Based on the open-source Monte Carlo Code GEANT4/ GEANT4-DNA (version 10.07.p03) (Agostinelli et al. 2003, Allison et al. 2006, Incerti et al. 2010a), the toolkit TOPAS and its extensions are freely accessible[‡]. With the TOPAS extension library TOPAS-nBio, in addition to simulations on the macroscopic scale, simulations can also be performed on nanoscopic scales, like cells and DNA. Here, not just every physical interaction of a particle track is simulated step-by-step until the primary particle has a residual kinetic energy of a few eV[§], but also the production and reactions of chemical species following the radiolysis can be simulated. Following the update of TOPAS-nBio, the code offers two methods of simulating the chemical stage: the step-by-step method (SBS) (Karamitros et al. 2011) and the independent reaction time method (IRT) (Schuemann et al. 2019, Green et al. 1990, Ramos-Méndez et al. 2020). While using the SBS method, the reaction kinetics are simulated step-by-step based on their simulated

[‡] <https://www.topasmc.org/> and <https://github.com/topas-nbio>

[§] The exact limit depends on the selected physics list and is between 7.4 eV and 11 eV (Incerti et al. 2018)

1
2
3 *Comparing two methods simulating inter-track interactions in TOPAS-nBio* 5

4
5 69 diffusion steps. Using the IRT method, the diffusion of chemicals is not calculated
6
7 70 step-by-step, but chemical reactions are simulated by calculating reaction times based
8
9 71 on the initial positions of pairs of radiolytic species and probability functions. Even
10
11 72 though the spatial information of the chemicals is not provided in contrast to the step-
12
13 73 by-step method, this approach features much higher computing efficiency. A detailed
14
15 74 description of this approach and a comparison to the SBS chemistry is given by Ramos-
16
17 75 Méndez et al. (2020). In previous studies, both TOPAS and TOPAS-nBio have been
18
19 76 well-validated against experimental data and other simulation studies (Perl et al. 2012,
20
21 77 Testa et al. 2013, McNamara et al. 2017, Ramos-Méndez et al. 2018).

22
23
24
25
26 78 *2.2. Simulation of inter-track interactions*

27
28 Investigating the effect of inter-track interactions was performed by calculating the G-
29
30 value in dependence on the number of tracks with inter-track interactions. Here, the
31
32 G-value is defined as the total number $M(t)$ of radiolytic species that are generated or
33
34 consumed in the case of chemical reactions at a given time t normalized to 100 eV of
35
36 deposited energy E , formalized by Karamitros et al. (2011) as:
37
38

$$39 \quad G(t) = \frac{M(t) \cdot 100}{E(\text{eV})}. \quad (1)$$

40
41
42
43
44

45 79 In the following, both methods to enable the modelling of inter-track interactions will
46
47 80 be described.

48
49
50
51 81 *2.2.1. Method 1: Phase Space Approach* This method was developed in a preliminary
52
53 82 work (Derksen et al. 2023) to investigate inter-track interactions with TOPAS-nBio 1.0
54
55 83 using the SBS approach. However, it is also possible to apply this method using the
56
57 84 IRT model available in TOPAS-nBio 2.0. To maintain consistent simulation conditions
58
59
60

1
2
3 *Comparing two methods simulating inter-track interactions in TOPAS-nBio* 6

4
5 85 for both methods, we utilized TOPAS-nBio version 2.0 in both cases.

6
7 86 This approach is based on a manipulation of the particle source using a phase space
8
9 87 file. Here, secondary particles produced by different primary particles are appointed
10
11 88 to one primary particle. This is achieved by modifying the label "Flag to tell if this
12
13 89 is the First Scored Particle from this History" in the phase space file. This label can
14
15 90 be 1 or 0. A label of 1 identifies the first particle scored of a given history, which
16
17 91 is not necessarily a primary particle depending on the settings of the scorer. A label
18
19 92 of 0 signifies particles belonging to the same history as the previously scored particle.
20
21 93 In our case, only primary particles are scored, meaning that all particles are initially
22
23 94 labeled with 1. By changing the label of a specific number of sequential particles to
24
25 95 0, those particles are considered as secondary particles from the previous particle with
26
27 96 label 1. Thus, all these particles are simulated simultaneously including the subsequent
28
29 97 created chemical species enabling inter-track interactions of different originally primary
30
31 98 particles. This approach allows to directly set the number N of primary particles whose
32
33 99 secondary particles can interact with each other. For details of this method, we refer to
34
35 100 Derksen et al. (2023). In the following, this method is referred to as the phsp method.
36
37
38
39
40

41 101 *2.2.2. Method 2: New Inter-track scorer in TOPAS-nBio 2.0* To simulate the yield
42
43 102 of radicals following radiolysis with inter-track interactions, TOPAS-nBio version 2.0
44
45 103 includes a scorer called *TsIRTInterTrack*. Applying this scorer, the user can set the
46
47 104 number of tracks with inter-track interactions, but also the relative position and time
48
49 105 delay of the primary tracks. However, this method only works with the IRT method.
50
51 106 An application of this scorer can be found in Ramos-Méndez et al. (2020). This method
52
53 107 will further be referred to as the TsIRTInterTrack method.
54
55
56
57
58
59
60

1
2 *Comparing two methods simulating inter-track interactions in TOPAS-nBio* 7

3
4
5 108 *2.3. Simulation setup*

6
7
8 109 An isotropic electron source of 4.5 keV positioned in the center of the coordinate system
9
10 110 was used as the source in the simulations. This energy was chosen since electrons with
11
12 111 this kinetic energy are important considering the formation of chemical spurs and DNA
13
14 112 damage segments (Ward 1988).

15
16 113 Since for the phsp method a phase space file needs to be scored, which will be post-
17
18 114 processed and used in the following simulations with inter-track interactions as explained
19
20 115 in section 2.2.1, the same phase space file was used as a basis for the source in the
21
22 116 simulations applying both methods to ensure consistent simulation setups. While using
23
24 117 the TsIRTInterTrack method, the phase space file was not modified in its fundamental
25
26 118 way, but using the phsp method, the phase space file had to be modified before
27
28 119 simulating G-values with inter-track interactions. This phase space file is scored on
29
30 120 the surface of a water-filled|| sphere with a radius of 0.5 nm placed around the source.

31
32
33 121 Using both methods, the G-value was scored in a sphere with 5 μm radius filled with
34
35 122 water. For the phsp method, the scorer *TsIRTGvalue* was applied to score the G-
36
37 123 value of each molecule type making use of the IRT chemistry method. Here, the
38
39 124 IRT chemistry model is employed for simulating the chemical stage of the simulation
40
41 125 since the subsequent TsIRTInterTrack method solely works with the IRT chemistry
42
43 126 approach, and consistent simulation setups were required for comparison of the two
44
45 127 methods enabling inter-track interactions. For the TsIRTInterTrack method, the scorer
46
47 128 *TsIRTInterTrack* was applied, which enables the simulation of inter-track interactions
48
49 129 by specifying the number N of tracks with inter-track interactions as well using the IRT
50
51 130 method. Using this scorer, no additional offset and no time delay was applied and all N
52
53
54
55
56 131 primary particles were simulated at the same time. When applying the TsIRTInterTrack
57
58 || Using *G4.WATER*, the density is 1 g/cm³, and the ionization potential is 78 eV.
59
60

Comparing two methods simulating inter-track interactions in TOPAS-nBio 8

method, the deposited energy was also scored, since the `TsIRTInterTrack` scorer does not normalize the number of chemicals to 100 eV of deposited energy, which is necessary when calculating G-values. In general, the objective of both scoring methods is to provide a G-value. However, one scorer, the `TsIRTInterTrack` scorer, incorporates the generation of inter-track interactions, and the other, the `TsIRTGvalue` scorer, does not, as inter-track interactions are achieved through a different mechanism.

To vary the number of inter-track interactions, the number N of primary particles, from which the chemical species can react in inter-track interactions with each other, was set to $N = 2, 3, 4, 5, 6, 10, 12, 15, 20, 30, 60$. When using the `phsp` method, 60 primary particles were simulated in total in one simulation run for all N . For the `phsp` method, this is valid since all N are divisors of 60, and the phase space file is modified so that N original primary particles are assigned to one primary particle in the phase space file. Contrary, applying the `TsIRTInterTrack` method, exactly N primary particles need to be simulated in one simulation run. For statistical reasons, the simulations were repeated 300 times with different random seeds.

Physical interactions were simulated by using the GEANT4 physics constructor `G4EmDNAPhysics_option2`, which is described in detail by Incerti et al. (2018) and has previously been investigated using TOPAS-nBio by Derksen et al. (2021). For simulating chemical kinetics and radiolytic species, we used the `TsEmDNAChemistry` module with the corresponding list of chemical specifications given in `TOPASDefaultReaction.txt`.

The end of the chemical stage was set to 1 μ s.

¶ <https://github.com/topas-nbio/TOPAS-nBio/blob/master/examples/scorers/IRTInterTrack/TOPASDefaultReactions.txt>

3. Results

In figure 1 and 2, the G-values for various chemical species and the sum of all species (G_{all}) are shown in dependence of the number N of tracks with inter-track interactions for both the phsp and TsIRTInterTrack methods. In addition, the yield of recombined water molecules, formed through a reaction of $\bullet\text{OH}$ and $\text{H}\bullet$ or H_3O and OH^- , is shown as it contributes to G_{all} . The general development of the G-value with increasing N agrees for both methods. With increasing N , the overall G-value decreases when using the phsp method as well as using the TsIRTInterTrack method. While the G-value decreases for most molecule types ($\bullet\text{OH}$, H_3O , OH^- , H_2O_2 and e_{aq}^+) with N , for some molecules (recombined H_2O , H_2) it increases. In comparison to our previous work (Derksen et al. 2023) the trends of individual molecules with N in this study differ slightly because on the one hand, a different source with a different LET was used and on the other hand, a different list of chemical reactions was included and the SBS approach was used instead of the IRT approach in this study. For a detailed analysis of G-values in dependence of N , we refer to Derksen et al. (2023). Regarding the summarized G-value of all molecule types, G_{all} , the G-values agree very well with a maximum difference of 0.2%. Nonetheless, examining solely G_{all} is insufficient, as the compensation of consumed and generated radicals may not expose differences between the methods. Consequently, a comparison of the G-values of individual molecules is essential. Regarding the individual radical species, the maximum difference of the G-value between both methods is observed for H_2O_2 (3.9%) and the minimum difference is seen for OH^- , for which the mean difference is less than 0.5%. Except for $\bullet\text{OH}$ and recombined water, the majority of G-values using the phsp method are smaller than those obtained using the TsIRTInterTrack method. This, and in combination with the

[†] In this manner, e_{aq} represents a free electron surrounded by a few (5-7) water molecules.

Comparing two methods simulating inter-track interactions in TOPAS-nBio 10

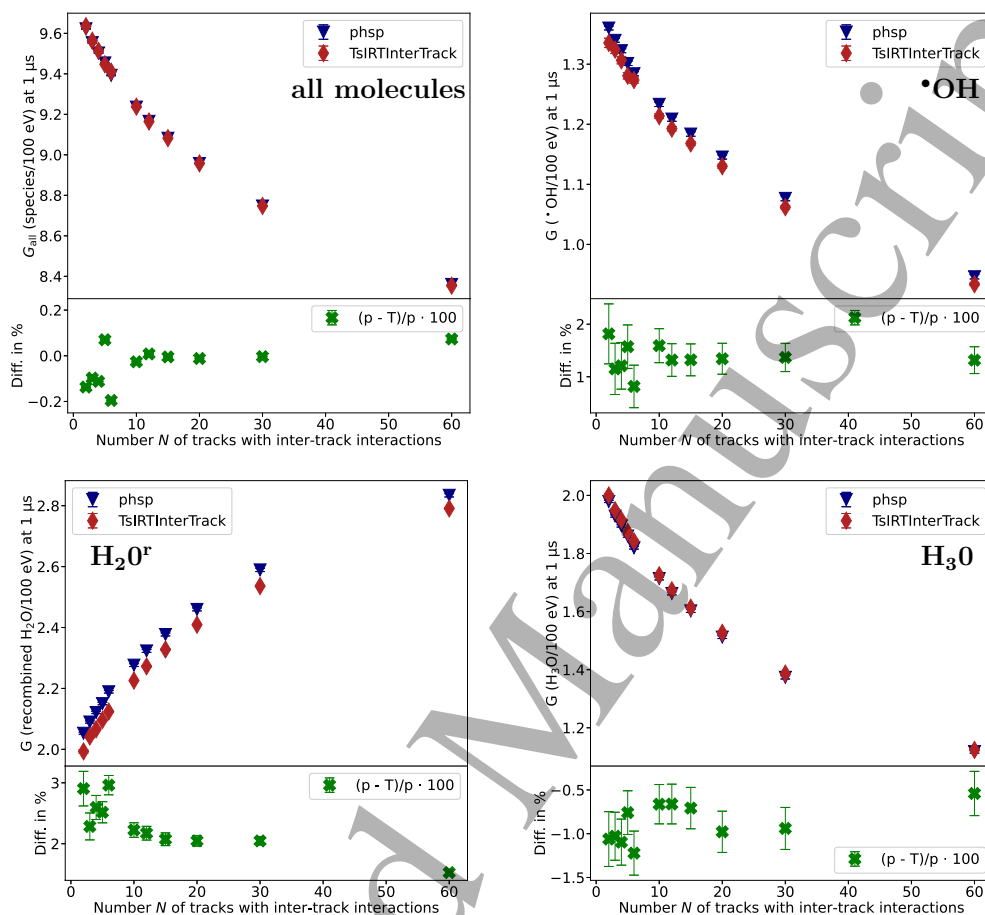


Figure 1: Comparison of the G-value G_{all} considering all molecules (upper left), $\bullet\text{OH}$ (upper right), recombined H_2O (bottom left) and H_3O (bottom right) using the phsp and TsIRTInterTrack method in dependence of the number N of tracks with inter-track interactions. In each upper panel, the G-value using both methods is depicted (phsp: blue triangles, TsIRTInterTrack: red diamonds) and in each bottom panel, the relative deviation of the TsIRTInterTrack results to phsp results are shown. Statistical uncertainties are represented by vertical error bars and correspond to one standard deviation.

Comparing two methods simulating inter-track interactions in TOPAS-nBio 11

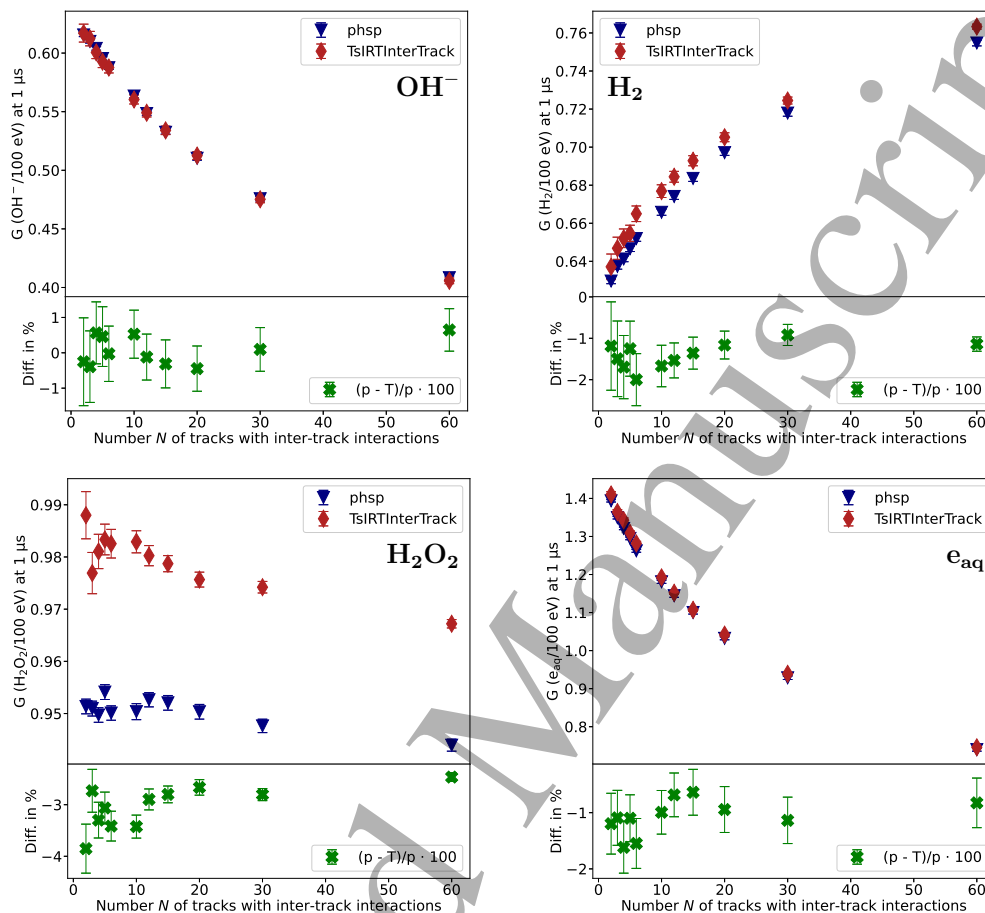


Figure 2: Comparison of the G-value considering OH⁻ (upper left), H₂ (upper right), H₂O₂ (bottom left) and e_{aq} (bottom right) using the phsp and TsIRTInterTrack method in dependence of the number *N* of tracks with inter-track interactions. In each upper panel, the G-value using both methods is depicted (phsp: blue triangles, TsIRTInterTrack: red diamonds) and in each bottom panel the relative deviation of the TsIRTInterTrack results to phsp results are shown. Statistical uncertainties are represented by vertical error bars and correspond to one standard deviation.

177 fact that the amount of recombined water constitutes approximately 20 - 35% of G_{all} ,
 178 proves our initial hypothesis that the positive difference of the G-value of $\bullet\text{OH}$ and
 179 recombined water using the TsIRTInterTrack method compared to the phsp method,
 180 can compensate the negative difference of the other chemical species. This way, the
 181 differences between phsp and TsIRTInterTrack for G_{all} are very low and present an

Comparing two methods simulating inter-track interactions in TOPAS-nBio 12

182 overstated positive agreement. Since the deviations between the methods are always
183 either negative or positive for each molecule type, we suspect that these are systematic
184 deviations.

185 In fact, it may initially seem confusing why these variations arise at all, considering that
186 the simulations employ the same toolkit version, identical physics and chemistry lists,
187 as well as the same dissociation tables, reactions, and diffusion constants — essentially
188 under identical conditions. The sole distinction lies in the generation of inter-track
189 interactions, implying that there are divergent operations in the code attributed to the
190 generation of inter-track interaction affecting the chemical stage of the simulation. We
191 investigated two potential factors that could be contributing to the deviations in the
192 number of molecules: First, we examined the number of inelastic processes from which
193 the chemical species are generated. Since inter-track interactions should not impact the
194 physical stage, there should be no difference between the two methods for generating
195 inter-track interactions. Nevertheless, we conducted this examination excluding any
196 issues in the physical stage that might affect the yield of chemicals. Additionally,
197 we investigated the number of chemical species processed directly at the beginning
198 of the chemical stage. This analysis was carried out because in the pre-chemical stage,
199 which connects the physical and chemical stages, not only the production of chemicals
200 occurs, but also chemical reactions, albeit relatively infrequently. This could be handled
201 differently between the two methods generating inter-track interactions resulting in a
202 variation of the G-value between the methods.

203 In figure 3 (left), the number of inelastic processes normalized to 100 eV of deposited
204 energy is shown for both methods generating inter-track interactions. Here, only
205 ionizations, electronic excitation and electron attachment are considered for the inelastic
206 processes, since these processes generate the chemical species that are processed during

Comparing two methods simulating inter-track interactions in TOPAS-nBio 13

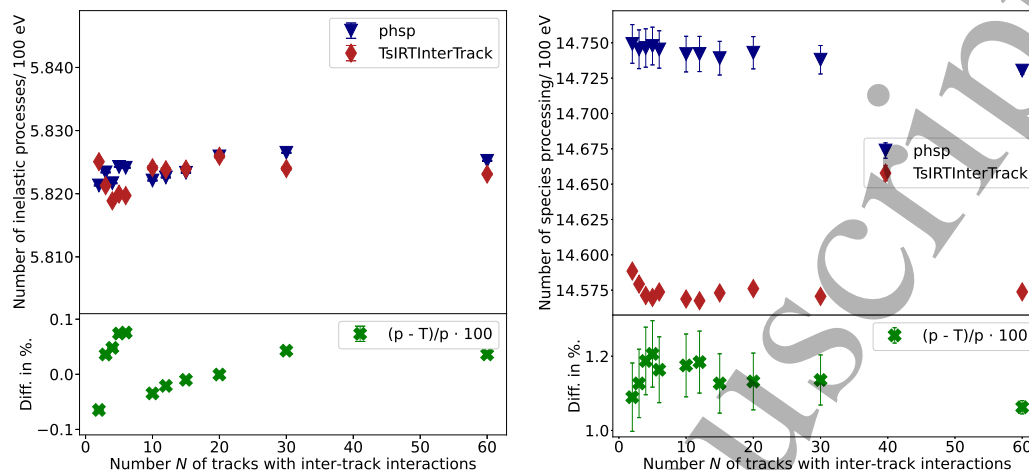


Figure 3: Left: Number of inelastic processes creating chemical species normalized to 100 eV of deposited energy in dependence of N shown for both methods (phsp: blue triangles, TsIRTInterTrack: red diamonds). Right: Number of chemical species processing normalized to 100 eV of deposited energy in dependence of the number N of tracks with inter-track interactions using the phsp (blue triangles) and TsIRTInterTrack (red diamonds) method. Each bottom panel shows the relative difference of TsIRTInterTrack to phsp results. Statistical uncertainties are represented by vertical error bars and correspond to one standard deviation.

the chemical stage. For all N , differences between the number of inelastic processes of both methods are smaller than 0.1% and with an average difference of 0.01(4)%, there is no significant difference between both methods noticeable.

In figure 3 (right), the number of chemical species that are initially processed within the chemical IRT method normalized to 100 eV of deposited energy is shown for both methods, as well as the relative difference of the TsIRTInterTrack method to the phsp method. Using the IRT chemistry method, this number is given by default in the output of each simulation for every history and considers only the chemical species processing at the beginning of the chemical stage, not the pre-chemical stage. Interestingly, the number of chemical species processing is on average 1.13(4)% higher with the phsp method compared to the TsIRTInterTrack method. As this investigated number of chemical species is the same as the G-value scored at 1 ps, we further studied time-

Comparing two methods simulating inter-track interactions in TOPAS-nBio 14

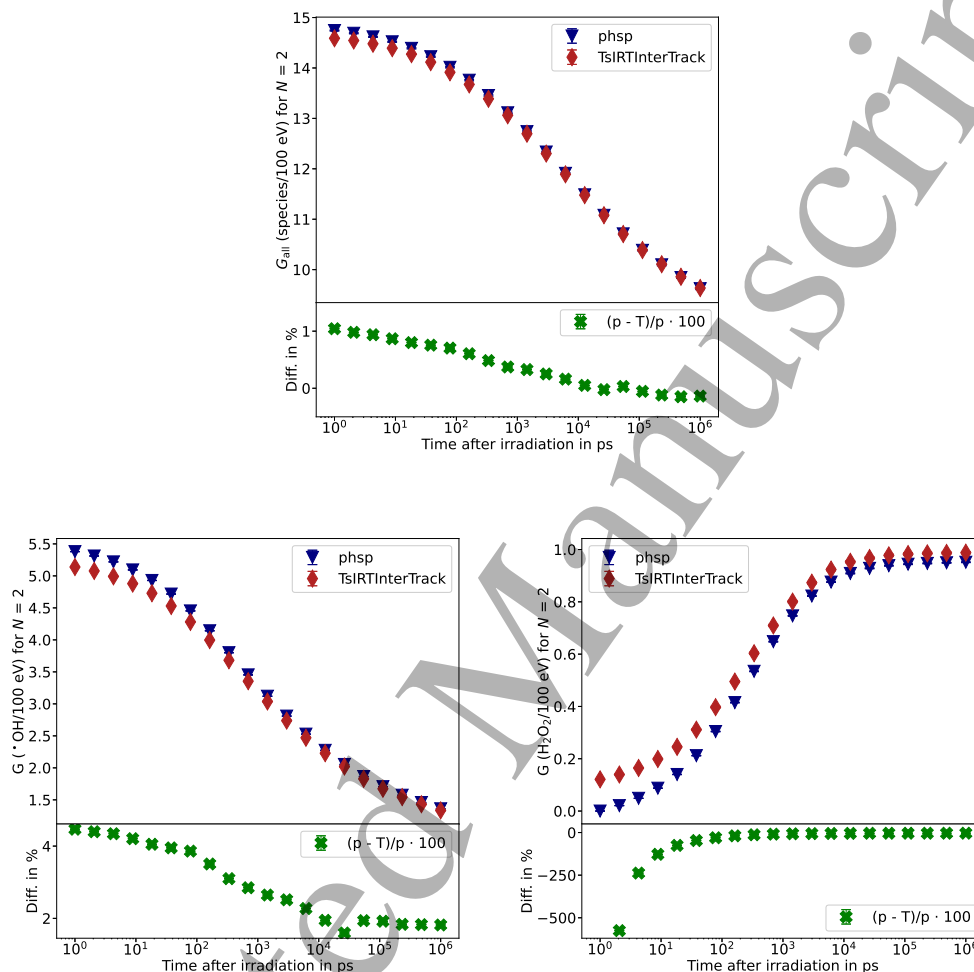


Figure 4: Comparison of time-dependent G-values for $N = 2$ using the phsp and TsIRTInterTrack method (Top: G_{all} , bottom left: G-values of $\bullet\text{OH}$, bottom right: G-values of H_2O_2). In each upper panel, the G-values are depicted for both methods and in each bottom panel, the difference of TsIRTInterTrack results relative to phsp results are shown. Statistical uncertainties represented by vertical error bars correspond to one standard deviation.

219 dependent G-values comparing both methods for generating inter-track interactions. In
 220 figure 4, time-dependent G-values are shown for $N = 2$ for G_{all} (top), for $\bullet\text{OH}$ (bottom
 221 left) and for H_2O_2 (bottom right) exemplary. As it can be seen in the bottom panel of
 222 each graph, relative differences of the TsIRTInterTrack method to the phsp method are

Comparing two methods simulating inter-track interactions in TOPAS-nBio 15

223 always the highest at the beginning of the chemical stage and become smaller towards
224 the end of the chemical simulation at 1 μ s. Different G-values at the beginning of the
225 chemical stage could be explained by the pre-chemical stage being treated differently in
226 terms of chemical reactions between the two methods.

227 In combination with the results of the number of inelastic processes, we conclude that
228 the differences in the G-value of some molecule types are caused by processing the
229 pre-chemical stage differently between the phsp and TsIRTInterTrack method, as the
230 G-values at 1 ps differ the most. Since detailed processes in the pre-chemical stage
231 cannot be studied with TOPAS-nBio, and there is no reference for these data, it is not
232 possible to decide which method provides the most accurate results. Nevertheless, since
233 the differences are acceptable with regard to deviations of experimental and simulated
234 data of radiolytic species (Ramos-Méndez et al. 2018), both methods seem to be suitable
235 for the simulation of inter-track interactions.

236 However, we noticed some differences in the handling of the two methods. Using
237 the TsIRTInterTrack method, the number of primary particles set in one simulation
238 run is defined by N , which means that exactly the number of tracks with inter-track
239 interactions needs to be simulated as primary particles to obtain accurate G-values.
240 Otherwise, invalid results will be obtained, which is further described in the appendix
241 Appendix A. Thus, a higher number of simulation runs is required to receive precise
242 statistical results. In contrast, using the phsp method, multiple of N primary particles
243 can be simulated in one simulation run, reducing the total number of runs required
244 to obtain comparable statistical results. However, applying the phsp method, two
245 separate simulations are necessary to create inter-track interaction because a phase
246 space file, which is further modified, needs to be scored in a first simulation. The
247 TsIRTInterTrack method has the advantage that, in principle, only one simulation is

Comparing two methods simulating inter-track interactions in TOPAS-nBio 16

248 sufficient to model inter-track interactions since a predefined scorer can be used. For
249 the phsp method, some programming effort is needed when modifying the phase space
250 file. Nevertheless, the user knows exactly how inter-track interactions are generated
251 since the simulations are manipulated accordingly. Another benefit of this method
252 is that the G-value is scored via the TsIRTGvalue scorer, so no post-processing is
253 necessary. In contrast, with the TsIRTInterTrack scorer, only the number of molecules,
254 not normalized to the deposited energy, is scored, and therefore the deposited energy
255 must also be scored in order to normalize the number of molecules to 100 eV of deposited
256 energy to obtain the G-value. Furthermore, it is crucial to acknowledge that the phsp
257 method is compatible with both the IRT and the SBS chemistry approach, while the
258 TsIRTInterTrack method is exclusively compatible with the IRT method. However,
259 it is worth noting that transitioning from the SBS to the IRT approach can result in
260 differences of approximately 5% (Ramos-Méndez et al. 2020).

4. Conclusion

262 G-values for different numbers of tracks with inter-track interactions were calculated in
263 TOPAS-nBio and compared using two different and independently developed methods
264 for generating inter-track interactions of N primary tracks. It was shown that the
265 G-values of both methods agree well, and differences regarding individual molecule
266 types are, on average, 1.5%. A reason for this could be a different consideration
267 of the pre-chemical stage influencing the dynamics of the following chemical stage.
268 Nevertheless, within the limits of uncertainties of experimental data of radiolysis
269 products and deviations to simulated data at conventional dose rates, both methods
270 seem suitable for simulating inter-track interactions, as they provide comparable G-
271 values, even though both techniques were developed independently of each other.

1
2
3 *Comparing two methods simulating inter-track interactions in TOPAS-nBio* 17

4
5 272 Furthermore, this comparison proved particularly informative by identifying a limitation
6
7 273 in the TsIRTInterTrack method, as this method can only accommodate a maximum of
8
9 274 N primary particles in one simulation.

10 11 12 13 275 **Acknowledgments**

14
15
16 276 The project was supported by the Federal Ministry of Education and Research
17
18 277 within the scope of the grant "Physikalische Modellierung für die individualisierte
19
20 278 Partikel-Strahlentherapie und Magnetresonanztomographie", (MiPS, grant number
21
22 279 13FH726IX6).

23 24 25 26 27 28 281 **Appendix A. Additional information simulating inter-track interactions** 29 30 282 **applying the TsIRTInterTrack scorer**

31
32
33
34 283 Figure A1 shows that simulating more primary particles than the defined number N of
35
36 284 tracks with inter-track interactions leads to invalid G-values using the *TsIRTInterTrack*
37
38 285 scorer. In figure A1(left), G_{all} is shown for enabling inter-track interactions of $N = 2$
39
40 286 primary tracks in dependence of the total number of simulated primary particles in one
41
42 287 simulation run. In comparison to simulations with two primary particles, which equals
43
44 288 N , in simulations using a higher number of primary particles than N , G_{all} decreases
45
46 289 significantly. In figure A1(right), G_{all} in dependence of time is illustrated simulating
47
48 290 2, 10 and 50 primary particles in one simulation run with inter-track interactions of
49
50 291 $N = 2$ tracks. As it can be seen, differences in the G-value between the number of
51
52 292 simulating primary particles become mainly visible at the end of the chemical stage.

53
54
55
56 293 Figure A2 shows an extract of the TOPAS simulation output using 10 primary particles
57
58 294 for inter-track interactions of $N = 2$ tracks. Here, the number of simulating chemicals

Comparing two methods simulating inter-track interactions in TOPAS-nBio 18

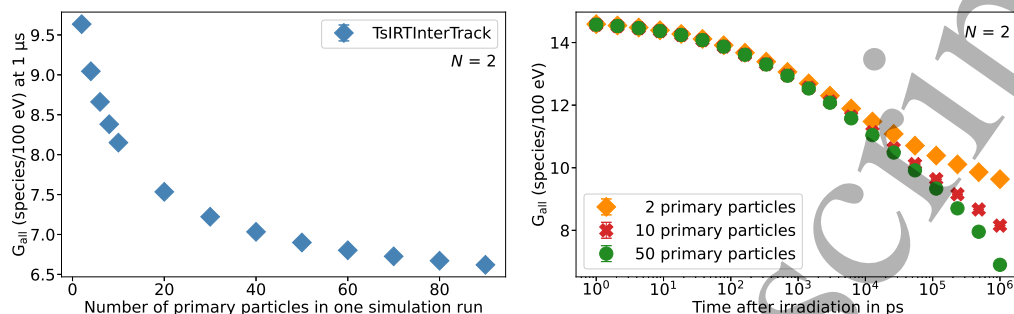


Figure A1: Left: G-value G_{all} using the TsIRTInterTrack method simulating inter-track interactions of two tracks ($N = 2$) in dependence of the total number of primary particles simulated in one run. Right: Time-dependent G_{all} for $N = 2$ simulating 2, 10 and 50 primary particles in one simulation run. For both graphs, statistical uncertainties are smaller than the symbol size and hence not depicted.

```

G4WT0 > Begin processing for Run: 0, History: 0
G4WT0 > Begin processing for Run: 0, History: 1
G4WT0 > - For event 1:
G4WT0 > --- IRT start for event 1
Processing 1318 species
G4WT0 > --- IRT ends for event 1
G4WT0 > Begin processing for Run: 0, History: 2
G4WT0 > Begin processing for Run: 0, History: 3
G4WT0 > - For event 3:
G4WT0 > --- IRT start for event 3
Processing 3114 species
G4WT0 > --- IRT ends for event 3
G4WT0 > Begin processing for Run: 0, History: 4
G4WT0 > Begin processing for Run: 0, History: 5
G4WT0 > - For event 5:
G4WT0 > --- IRT start for event 5
Processing 5119 species
G4WT0 > --- IRT ends for event 5

G4WT0 > Begin processing for Run: 0, History: 6
G4WT0 > Begin processing for Run: 0, History: 7
G4WT0 > - For event 7:
G4WT0 > --- IRT start for event 7
Processing 7226 species
G4WT0 > --- IRT ends for event 7
G4WT0 > Begin processing for Run: 0, History: 8
G4WT0 > Begin processing for Run: 0, History: 9
G4WT0 > - For event 9:
G4WT0 > --- IRT start for event 9
Processing 9315 species
G4WT0 > --- IRT ends for event 9
TOPAS run sequence complete.
Particle source Demo: Total number of histories: 0
Particle source Example: Total number of histories: 10

```

Figure A2: Extract of the output simulating 10 primary particles with inter-track interactions of $N = 2$ primary tracks. Here, a history refers to a new primary particle.

at the beginning of the chemical stage are shown after each pair of primary tracks (indicated by a new history) with inter-track interactions. Interestingly, the number of processing species does not remain roughly the same for each pair of simulated histories as expected, but increases significantly with further simulated histories. It seems like a pair of simulated histories considers also every chemical species created from all previous

REFERENCES

19

1
2
3
4
5 300 simulated histories, which would explain the increase of chemical species with increasing
6
7 301 number of successive histories. This in turn explains the decreasing G-value for an
8
9 302 increasing number of primary particles simulated for the same number of tracks with
10
11 303 inter-track interactions shown in figure A1. This is due to the fact that the averaged
12
13 304 G-value is actually calculated from G-values considering inter-track interactions of an
14
15 305 increasing number of primary particle tracks (multiple of N , see figure A2) even though
16
17 306 the number of tracks with inter-track interactions is defined in the scorer. Therefore,
18
19 307 when using the TsIRTINterTrack scorer, care should be taken to ensure that the number
20
21 308 of primary particles is equal to the number of tracks with inter-track interactions.
22
23
24
25

References

- 26 309 **References**
27
28
29 310 Agostinelli, S. et al. (2003), 'GEANT4 - a simulation toolkit', *Nucl. Instrum. Methods*
30
31 311 *Phys. Res. A* **506**, 250–303.
32
33
34 312 Allison, J., Amako, K., Apostolakis, J., Araujo, H., Arce Dubois, P., Asai, M., Barrand,
35
36 313 G., Capra, R., Chauvie, S., Chytráček, R., Cirrone, G., Cooperman, G., Cosmo, G.,
37
38 314 Cuttone, G., Daquino, G., Donszelmann, M., Dressel, M., Folger, G., Foppiano, F.,
39
40 315 Generowicz, J., Grichine, V., Guatelli, S., Gumplinger, P., Heikkinen, A., Hrivnacova,
41
42 316 I., Howard, A., Incerti, S., Ivanchenko, V., Johnson, T., Jones, F., Koi, T., Kokoulin,
43
44 317 R., Kossov, M., Kurashige, H., Lara, V., Larsson, S., Lei, F., Link, O., Longo,
45
46 318 F., Maire, M., Mantero, A., Mascialino, B., McLaren, I., Mendez Lorenzo, P.,
47
48 319 Minamimoto, K., Murakami, K., Nieminen, P., Pandola, L., Parlati, S., Peralta,
49
50 320 L., Perl, J., Pfeiffer, A., Pia, M., Ribon, A., Rodrigues, P., Russo, G., Sadilov, S.,
51
52 321 Santin, G., Sasaki, T., Smith, D., Starkov, N., Tanaka, S., Tcherniaev, E., Tome,
53
54 322 B., Trindade, A., Truscott, P., Urban, L., Verderi, M., Walkden, A., Wellisch,
55
56 323 J., Williams, D., Wright, D. & Yoshida, H. (2006), 'GEANT4 developments and
57
58
59
60

REFERENCES

20

- 324 applications', *IEEE Transactions on Nuclear Science* **53**(1), 270–278.
- 325 Baikalov, A., Abolfath, R., Mohan, R., Schüler, E., Wilkens, J. J. & Bartzsch, S. (2022),
326 'Modeling interspur interactions as a potential mechanism of the FLASH effect', *arXiv*
327 *preprint arXiv:2207.12287*.
- 328 Derksen, L., Flatten, V., Engenhardt-Cabillic, R., Zink, K. & Baumann, K.-S.
329 (2023), 'A method to implement inter-track interactions in Monte Carlo simulations
330 with TOPAS-nBio and their influence on simulated radical yields following water
331 radiolysis', *Physics in Medicine and Biology* **68**(13).
- 332 Derksen, L., Pfuhl, T., Engenhardt-Cabillic, R., Zink, K. & Baumann, K.-S. (2021),
333 'Investigating the feasibility of TOPAS-nBio for Monte Carlo track structure
334 simulations by adapting GEANT4-DNA examples application', *Physics in Medicine*
335 *& Biology* **66**(17), 175023.
- 336 Faddegon, B., Ramos-Mendez, J., Schuemann, J., McNamara, A., Shin, J., Perl, J. &
337 H., P. (2020), 'The TOPAS Tool for Particle Simulation, a Monte Carlo Simulation
338 Tool for Physics, Biology and Clinical Research', *Physica Medica* **72**, 114–121.
- 339 Green, N., Pilling, M., Pimblott, S. & Clifford, P. (1990), 'Stochastic modeling of fast
340 kinetics in a radiation track', *Journal of Physical Chemistry* **94**(1), 251–258.
- 341 Incerti, S., Baldacchino, G., Bernal, M., Capra, R., Champion, C., Francis, Z., Guatelli,
342 S., Guèye, P., Mantero, A., Mascialino, B., Moretto, P., Nieminen, P., Rosenfeld,
343 A., Villagrasa, C. & Zacharatou, C. (2010a), 'The Geant4-DNA project The Geant4-
344 DNA collaboration', *International Journal of Modeling, Simulation, and Scientific*
345 *Computing* **1**(2), 157.
- 346 Incerti, S., Kyriakou, I., Bernal, M., Bordage, M., Francis, Z., Guatelli, S., Ivanchenko,
347 V., karamitros, M., Lampe, N., Lee, S., Meylan, S., Min, C., Shin, W., Nieminen, P.,
348 Sakata, D., Tang, N., Villagrasa, C., Tran, H. & Brown, J. (2018), 'GEANT4-DNA

REFERENCES

21

- example applications for track structure simulations in liquid water: A report from the GEANT4-DNA Project', *Medical Physics* **45**(8), e722–e739.
- Karamitros, M., Mantero, A., Incerti, S., Friedland, W., Baldacchino, G., Barberet, P., Bernal, M., Capra, R., Champion, C., El Bitar, Z. et al. (2011), 'Modeling radiation chemistry in the GEANT4 toolkit', *Prog. Nucl. Sci. Technol* **2**, 503–508.
- Lai, Y., Jia, X. & Chi, Y. (2021), 'Modeling the effect of oxygen on the chemical stage of water radiolysis using GPU-based microscopic Monte Carlo simulations, with an application in FLASH radiotherapy', *Physics in Medicine & Biology* **66**(2), 025004.
- McNamara, A., Geng, C., Turner, R., Mendez, J. R., Perl, J., Held, K., Faddegon, B., Paganetti, H. & Schuemann, J. (2017), 'Validation of the radiobiology toolkit TOPAS-nBio in simple DNA geometries', *Physica Medica* **33**, 207 – 215.
- Perl, J., Shin, J., Schümann, J., Faddegon, B. & Paganetti, H. (2012), 'TOPAS: An innovative proton Monte Carlo platform for research and clinical applications', *Medical Physics* **39**(11), 6818–6837.
- Ramos-Méndez, J., Domínguez-Kondo, N., Schuemann, J., McNamara, A., Moreno-Barbosa, E. & Faddegon, B. (2020), 'LET-dependent intertrack yields in proton irradiation at ultra-high dose rates relevant for FLASH therapy', *Radiation research* **194**(4), 351–362.
- Ramos-Méndez, J., Perl, J., Schuemann, J., McNamara, A., Paganetti, H. & Faddegon, B. (2018), 'Monte Carlo simulation of chemistry following radiolysis with TOPAS-nBio', *Physics in Medicine & Biology* **63**(10), 105014.
- Ramos-Méndez, J., Shin, W.-G., Karamitros, M., Domínguez-Kondo, J., Tran, N. H., Incerti, S., Villagrasa, C., Perrot, Y., Štěpán, V., Okada, S., Moreno-Barbosa, E. & Faddegon, B. (2020), 'Independent reaction times method in Geant4-DNA: Implementation and performance', *Medical physics* **47**(11), 5919–5930.

REFERENCES

22

- 374 Schuemann, J., McNamara, A. L., Ramos-Méndez, J., Perl, J., Held, K. D., Paganetti,
375 H., Incerti, S. & Faddegon, B. (2019), 'TOPAS-nBio: An Extension to the TOPAS
376 Simulation Toolkit for Cellular and Sub-cellular Radiobiology', *Radiation Research*
377 **191**, 125–138.
- 378 Testa, M., Schuemann, J., Lu, H.-M., Shin, J., Faddegon, B., Perl, J. & Paganetti,
379 H. (2013), 'Experimental validation of the TOPAS Monte Carlo system for passive
380 scattering proton therapy', *Medical Physics* **40**(12), 1–16.
- 381 Ward, J. F. (1988), 'DNA damage produced by ionizing radiation in mammalian
382 cells: identities, mechanisms of formation, and reparability', *Progress in nucleic acid*
383 *research and molecular biology* **35**, 95–125.

1
2
3
4
5
6
7
8
9
10
11
12
13
14
15
16
17
18
19
20
21
22
23
24
25
26
27
28
29
30
31
32
33
34
35
36
37
38
39
40
41
42
43
44
45
46
47
48
49
50
51
52
53
54
55
56
57
58
59
60

Appendix

Verzeichnis der akademischen Lehrenden

Meine akademischen Lehrenden waren in Dortmund:

- Prof. Dr. Karl-Heinz Bauer
- Prof. Dr. Andreas Block
- Prof. Dr. Roland Böhmer
- Prof. Dr. Winfried Kaballo
- Prof. Dr. Shaukat Khan
- Prof. Dr. Jan Kierfeld
- Prof. Dr. Gudrun Hiller
- Prof. Dr. Jörg Horst
- Prof. Dr. Heinrich Päs
- Prof. Dr. Jörg Rahnenführer
- Prof. Dr. Matthias Schneider
- Prof. Dr. Bernhard Spaan
- Prof. Dr. Metin Tolan
- Prof. Dr. Carsten Westphal

Meine akademischen Lehrenden waren in Bochum:

- Prof. Dr. Klaus Gerwert
- Prof. Dr. Eckhard Hofmann

Meine akademischen Lehrenden waren in Gießen:

- Prof. Dr. Klemens Zink

Meine akademischen Lehrenden waren in Marburg:

- Prof. Dr. Rita Engenhardt-Cabillic

Danksagung

Im Zuge meiner Promotion möchte ich mich von Herzen bei all jenen bedanken, die mich auf meinem Weg begleitet und unterstützt haben.

Ein besonderer Dank gebührt Frau Prof. Dr. Engenhardt-Cabillic und Herrn Prof. Dr. Klemens Zink. Ich schätze Ihre großzügige Bereitschaft, meine Doktorarbeit unter Ihrer fachkundigen Betreuung verfassen zu dürfen. Ich bedanke mich für die zahlreichen anregenden Diskussionen zu meinem Forschungsthema, die fortwährende Unterstützung und das Vertrauen in meine Arbeit. Auch möchte ich mich für die Gelegenheit, an nationalen und internationalen Konferenzen teilzunehmen, bedanken. Diese Erfahrung eröffnete mir nicht nur einen vertieften Einblick in die Themengebiete der medizinischen Physik, sondern erwies sich auch als hilfreich für das Knüpfen von Kontakten und den Austausch mit anderen Wissenschaftlern.

Ein herzliches Dankeschön gilt auch Dr. Kilian-Simon Baumann für seine engagierte Unterstützung während meiner Promotion. Seine vielfältigen und hilfreichen Tipps, insbesondere im Bereich der Monte-Carlo-Simulationen, und die zahlreichen anregenden Diskussionen haben meine Arbeit in bedeutender Weise geprägt. Er nahm sich stets die Zeit, mir zuzuhören, und hat mich in meinem Vorhaben bestärkt.

Außerdem möchte ich meinen Kolleginnen und Kollegen am IMPS danken, die mich herzlich in der Arbeitsgruppe aufgenommen haben. Ihre Erklärungen, Unterstützung und kollegiale Atmosphäre haben meine Promotionszeit sehr bereichert.

Nicht zuletzt möchte ich mich auch bei meiner Familie und meinen Freunden außerhalb der Wissenschaft für jegliche Unterstützung und den starken emotionalen Rückhalt über die Dauer meiner Promotion bedanken.